

Evaluation of Stratospheric Iodine Oxide Concentrations from Balloon Borne Remote Sensing Measurements

Student: 01709003

Supervisor: Prof. Dr Andre Butz

Supervisor: Karolin Voss

Word Count: 12,406

**Imperial College
London**

Preface

This project was conducted within the Atmosphere group at the Environmental Physics Institute of Heidelberg University. The TotalBro instrument used to gather the data analysed in this dissertation was developed by this research group, and was deployed once previously in 2021. I was not involved in the development of the instrument or the data acquisition campaign, as this took place in August 2022.

I travelled to Karlsruhe Institute of Technology in November 2022 with my supervisor Karolin Voss to retrieve the instrument after it was returned from Canada. I spent several days assisting in the retrieval of instrument calibration spectra, the process of which is described in Chapter 4 of this report. I analysed these spectra and developed a calibration and resolution scheme for the instrument, both of which I then use in my subsequent data analysis.

Data analysis relied on the use of the QDOAS program, developed by the Royal Belgian Institute for Astrophysics. I obtained access to this program by requesting it from the aforementioned organisation, and did not make any alterations/contributions to it. I also used the DAMF program, which I obtained from my supervisor.

Besides this, I modified scripts provided in my lecture courses and provided as part of past Bachelors and Masters Theses to perform profile retrievals. I carried out a week-long lab based practical to better understand the full process of retrieving and correcting DOAS spectra. I also performed the analysis for various retrieval scenarios discussed in Chapter 5 of my thesis, and developed my own code for the profile retrieval described in Chapter 6.

My supervisor provided me with the pseudoabsorber cross-sections used for the correction of wave-like structures in the retrieval, as described in Chapter 5. She also performed the spectral coaddition described in Chapter 4.

Abstract

Reactive species containing chlorine and bromine are known to participate in catalytic reaction cycles that effectively destroy stratospheric ozone [1]. Recent aircraft measurements in the lower stratosphere have indicated that iodine is also efficient in ozone destruction, and that Iodine Oxide (IO) radicals remain detectable in the stratosphere at concentrations of (0.06 ± 0.03) pptv [2]. However, there is a high uncertainty about the role of atmospheric iodine chemistry in catalytic ozone destruction due to a lack of widespread ground or satellite-based observations [3]. This study aims to apply balloon-borne Differential Optical Absorption Spectroscopy (DOAS) remote sensing methods to quantify total stratospheric IO content, and to retrieve a vertical concentration profile for IO in the lower and middle stratosphere via solar occultation and ascent measurements.

Spectra were obtained by the TotalBrO [4] [5] instrument during the HEMERA 3 balloon launch from Timmins, Canada in August 2022 [6]. The instrument consists of an active solar tracker which couples ultraviolet (UV) and visible (VIS) light into two grating spectrometers via glass fibres. This study analyses VIS measurements using the QDOAS program [7]. A suitable retrieval scenario was obtained by conducting a sensitivity study, which simultaneously examines if *IO* is reliably detected.

Retrieved differential Slant Column Density (dSCD) values are analysed using Langley's Method to obtain an overhead Volume Mixing Ratio (VMR) for O_3 , NO_2 and *IO*. The Tikhonov inversion technique is then used to retrieve mid-stratosphere vertical concentration profiles for these species. The retrieved O_3 results compare well with data gathered by an Ozone sonde released closely after the HEMERA 3 launch, as well as data taken by a Microwave Limb Sounder (MLS) satellite, which surveyed the area close to the same time.

IO is found to be on the limit of the detection sensitivity of the DOAS method, with concentrations peaking at 0.4 ppt in the retrieved vertical profile. An overhead VMR of 3.5 ppt was found, presenting an unphysical contrast and an abnormally high value. Residual structures obtained in DOAS fits were larger than *IO* absorption peaks, and errors in the retrieved vertical profile extended to zero for most data points.

Contents

| | | |
|----------|--|-----------|
| 1 | Introduction | 4 |
| 2 | Theoretical Background | 6 |
| 2.1 | Atmospheric Structure | 6 |
| 2.2 | Ozone Layer | 7 |
| 2.3 | Iodine Oxide | 11 |
| 3 | Differential Optical Absorption Spectroscopy | 14 |
| 3.1 | Atmospheric Absorption of Light | 14 |
| 3.1.1 | Rayleigh Scattering | 15 |
| 3.1.2 | Mie Scattering | 16 |
| 3.1.3 | Atmospheric Absorption | 16 |
| 3.2 | Atmospheric Spectroscopy | 16 |
| 3.2.1 | Real Measurements | 17 |
| 3.3 | Langley's Method | 18 |
| 3.4 | Profile Retrieval | 19 |
| 3.5 | Shortcomings and Corrections for DOAS Method | 19 |
| 3.5.1 | Centre to Limb Darkening | 19 |
| 3.5.2 | Ring Effect, Solar I_0 effect | 20 |
| 4 | Experimental Techniques | 22 |
| 4.1 | TotalBro Instrument | 22 |
| 4.2 | Instrument Calibration | 25 |
| 5 | QDOAS: Analysing Spectra | 30 |
| 5.1 | Fit Scenario | 30 |
| 5.1.1 | Wavelength Range | 31 |
| 5.1.2 | Polynomial Order | 34 |
| 5.1.3 | Reference Cross Sections | 34 |
| 5.2 | Results | 40 |
| 5.3 | Sensitivity Study | 44 |
| 6 | Results | 46 |
| 6.1 | Langley Plots | 46 |
| 6.2 | Profile Retrieval | 49 |
| 6.2.1 | Ozone | 51 |
| 6.2.2 | NO_2 | 51 |
| 6.2.3 | IO | 54 |

| | |
|---|-----------|
| 7 Validation | 56 |
| 7.1 Sonde Ozone Data | 56 |
| 7.2 MLS Data | 56 |
| 8 Conclusion | 59 |
| 8.1 Acknowledgements | 59 |
| Bibliography | 60 |
| A Coadded Spectra per Data Point | 67 |
| B Full QDOAS Output SZA 93.46° | 68 |
| C Zeroth Order Tikhonov Regularization Routine | 70 |

Chapter 1

Introduction

Ozone (O_3) is an atmospheric gas formed by photochemical reactions from Oxygen (O_2) [8]. The 'Ozone Layer' refers to a layer in the stratosphere of the Earth at an altitude between 15 km and 30 km containing a high concentration of ozone. Life on Earth as we know it would be impossible without the ozone layer; it protects biological organisms against most of the damaging ultraviolet (UV) radiation from the Sun, as Ozone molecules exhibit strong absorption bands over an extensive UV wavelength range [9]. This significant absorption results in a positive temperature gradient within the stratosphere, maintaining its stably stratified vertical structure. In addition to this, it makes Ozone a strong greenhouse gas, as absorbed UV radiation is mostly re-emitted as long-wave radiation, thereby contributing to the greenhouse effect.

Increases in UV radiation reaching the Earth's surface due to decreasing ozone amounts were observed during the 1980s and 1990s, particularly at high latitudes where ozone depletion was more pronounced [10]. It was determined that this ozone depletion was caused by human emission of Ozone Depleting Substances (ODS); these include CFCs, HCFCs, halons, methyl bromide, carbon tetrachloride, and methyl chloroform. ODS are generally very stable in the troposphere and only degrade under intense ultraviolet light in the stratosphere. When they break down, they release halogen atoms (mainly chlorine or bromine), which then deplete ozone [11].

Iodine is the heaviest of the stable Halogen elements, commonly found in natural brines and seaweed [12] and widely used as a disinfectant and antiseptic [13]. The natural ecology of iodine is shown in Fig. 1.1. As the right-hand side of the figure illustrates, a small fraction of natural iodine enters the atmosphere through evaporation from seawater.

Reactive species containing chlorine and bromine, particularly chlorine monoxide (ClO) and bromine monoxide (BrO), are known to participate in catalytic reaction cycles that effectively destroy stratospheric ozone [1]. Recent aircraft measurements in the lower stratosphere have indicated that iodine is also efficient in the destruction of ozone, and that IO radicals remain detectable in the stratosphere at concentrations of (0.06 ± 0.03) pptv [2]. However, there is a high uncertainty in the role of atmospheric iodine chemistry in catalytic ozone destruction compared to bromine chemistry due to a lack of widespread ground or satellite-based observations [3].

One of the techniques used in detecting reactive iodine atomic species in the atmosphere was Differential Optical Absorption Spectroscopy (DOAS) [14]. DOAS allows for the derivation of column abundances of trace species from measurements of electromagnetic radiation, mainly in the UV and visible spectral range [15]. This project centres on the application of the DOAS technique to balloon-borne spectral measurements in the visible spectral range to evaluate the

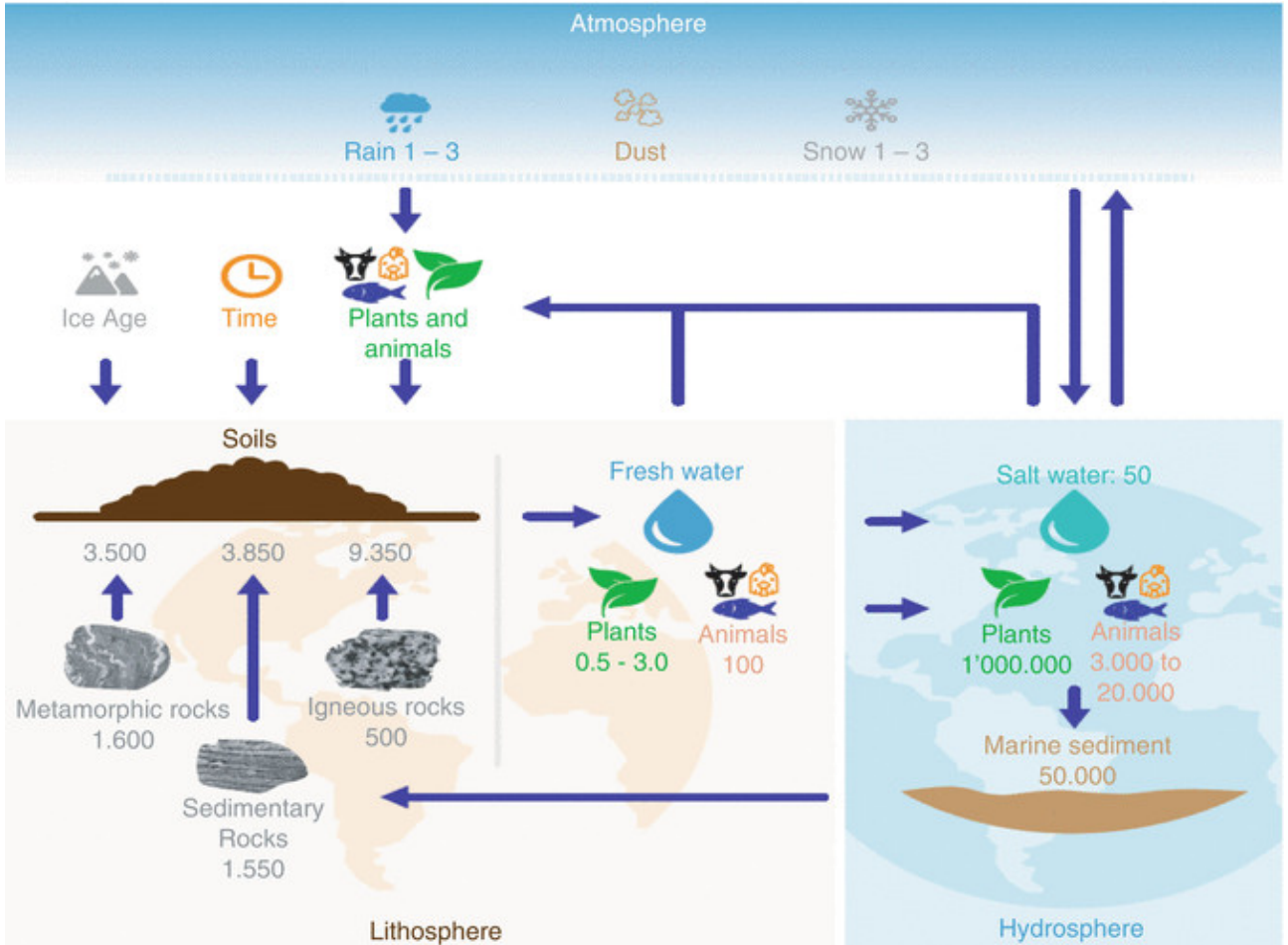


Figure 1.1: Iodine ecology in nature: Certain marine plants and animals have developed mechanisms that enable them to concentrate large amounts of iodine in their tissues and when they die and fall to the bottom of the sea, iodine becomes part of the sediment and the sedimentary rocks that may form later on. Part of the iodine contained in seawater evaporates and rises to the atmosphere, probably attached to dust particles. From [12].

presence of iodine oxide in the atmosphere.

The balloon-borne spectral measurements evaluated in this project were obtained during the HEMERA-3 balloon launch from the Timmins Stratospheric Balloon Base in Ontario, Canada [6]. Data were gathered by a direct-sun DOAS instrument referred to as TotalBrO, which was developed at Heidelberg University [4] [5].

Chapter 2

Theoretical Background

2.1 Atmospheric Structure

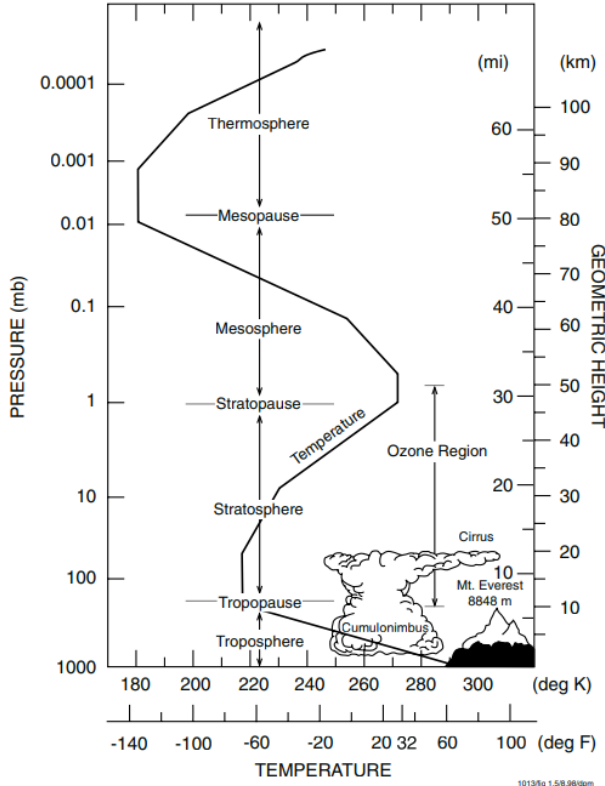


Figure 2.1: Schematic representation of the thermal structure of the atmosphere with its different layers, from [16]. The relevant layers for this project are the Troposphere and Stratosphere.

of vertical and interhemispheric convection and mixing; these processes occur on timescales of four to six years, in stark contrast to the timescales of a few months observed in the troposphere

The atmosphere can be divided into several layers according to temperature, mixing mechanisms, and degree of ionization, as illustrated by Fig. 2.1. This vertical structure of atmospheric temperature is qualitatively similar everywhere, despite significant horizontal temperature variation [17].

Closest to the Earth's surface lies the troposphere, which extends from between 7 km (at the poles) to 18 km (at the equator) and contains around 75% of the total mass of the atmosphere [18]. Since this layer is in direct contact with the Earth's surface, it experiences a steady drop in temperature with height due to adiabatic cooling of about 7 K per kilometre (for dry air), referred to as the adiabatic lapse rate [19]. This well-mixed layer contains almost all atmospheric water vapor and is responsible for most weather phenomena [20].

The second-lowest atmospheric layer is the Stratosphere, which lies between 18 km and 50 km above the surface of the earth [21]. Within this region, temperature increases with altitude as a result of the absorption of Ultra-Violet (UV) radiation by the ozone layer [22], an inversion of the decreasing temperature gradient observed in the layer below. It gains its name from being composed of stably stratified temperature layers.

This stability leads to extremely low levels

[4]. Horizontally, the stratosphere is generally very well mixed by zonal winds.

A few kilometres beyond the tropopause, stratospheric flow is completely dominated by the zonal mean circulation and planetary waves; weather disturbances cease to play a role [23]. As a result, aerosols that reach the stratosphere can persist there for significant time periods.

Only the troposphere and stratosphere are relevant to the work carried out in this project, as atmospheric gas concentrations above the stratopause are not measured.

Above the stratopause lie the Mesosphere and then the Thermosphere, which are briefly described for the sake of completion.

The Mesosphere extends from 50 km to 85 km and contains about 0.1% of the total atmospheric air mass [24]. Within this region temperatures drop with increasing altitude, reaching a minimum of around 185 K at the Mesopause, making this the coldest place in the Earth's atmosphere [25]

The Thermosphere is the highest atmospheric layer and extends from altitudes of 85 km to about 500 km. This region contains the ionosphere, and is characterized by high temperature and large variability, in response to changes in solar ultraviolet radiation and solar-driven geomagnetic activity. The lower thermosphere is primarily composed of N_2 and O_2 , while the upper thermosphere is dominated by atomic oxygen (O) due to the importance of photodissociation and molecular diffusion at high altitudes. Dynamical motion at these altitudes results from complex interactions between solar heating, auroral processes, the resulting pressure gradients, and dissipative processes [25].

2.2 Ozone Layer

The ozone (O_3) layer refers to a thin O_3 containing region within the stratosphere. About 90% of atmospheric total ozone resides in the stratosphere, with concentrations peaking at 10 ppm [26]. The other 10% mainly resides in the troposphere, where it presents a hazard to the health of biological organisms through direct contact [27], and is considered 'bad' ozone.

The ozone layer is considered 'good' ozone, as it absorbs most of the Sun's medium-frequency UV-B light (wavelengths between 290 - 320 nm). Excess amounts of this radiation are associated with sunburn, skin cancer and cataracts, although the small amounts that pass through are necessary for vitamin D production. It also absorbs all UV-C light (wavelengths between 240 - 290 nm), which is essential to the existence of life as we know it since this radiation destroys nucleic acids (RNA and DNA) and protein [29]. Fig. 2.2 illustrates the vertical structure of the Ozone layer and its absorbing properties.

Due to the significance of the presence of Ozone in maintaining the health of biological organisms, observations of the total integrated column ozone began in the early 20th century, dating back to 1913 [30]. Beginning in the 1980s, measurements of this type revealed a marked decrease in total ozone column density over many regions of the Earth [31].

The cycle governing the formation and decomposition of ozone was first posited by Chapman in 1930 [32]. It consists of the following 5 reactions [33]:



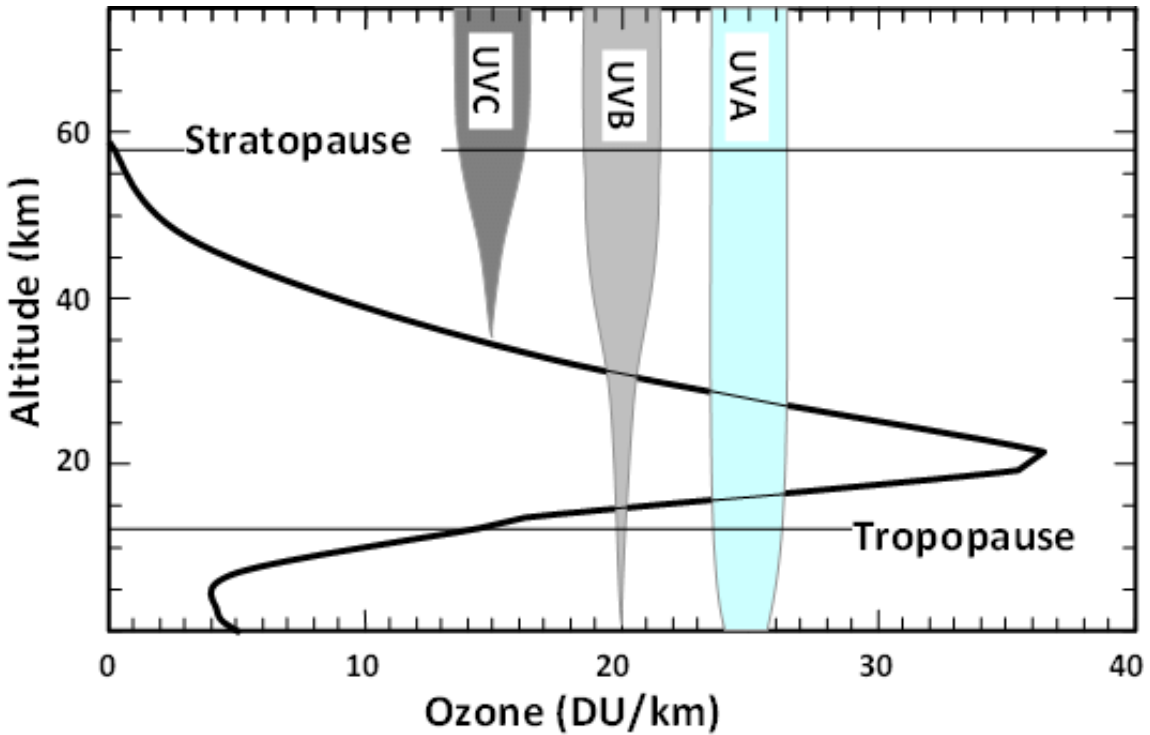


Figure 2.2: Typical vertical profile of ozone concentration and its UV screening properties. From [28].



In these equations, M represents any third molecule that absorbs the heat from the reaction [34] and is necessary to conserve momentum.

This cycle alone strongly overestimates the total ozone column in the tropics [35]. This is because Ozone can also be lost through a reaction with several chemical families that catalyse its destruction [36]. This catalytic cycle can be represented as:



Where the catalyst, denoted by X, is most commonly a nitrogen, hydrogen, chlorine, or bromine species, such as NO, OH, BrO, or ClO (in order of significance) [37]. The catalyst is reformed at the end of the reaction and can destroy thousands of ozone molecules before it is removed from the atmosphere.

The observed ozone depletion was determined to be caused by the human-related emission of ozone depleting substances (ODS) [38]. ODS release molecules from the Halogen group into the stratosphere, where these molecules act as catalysts in the decomposition of ozone [39]. Following this discovery, the Montreal Protocol was introduced in 1987 to control the

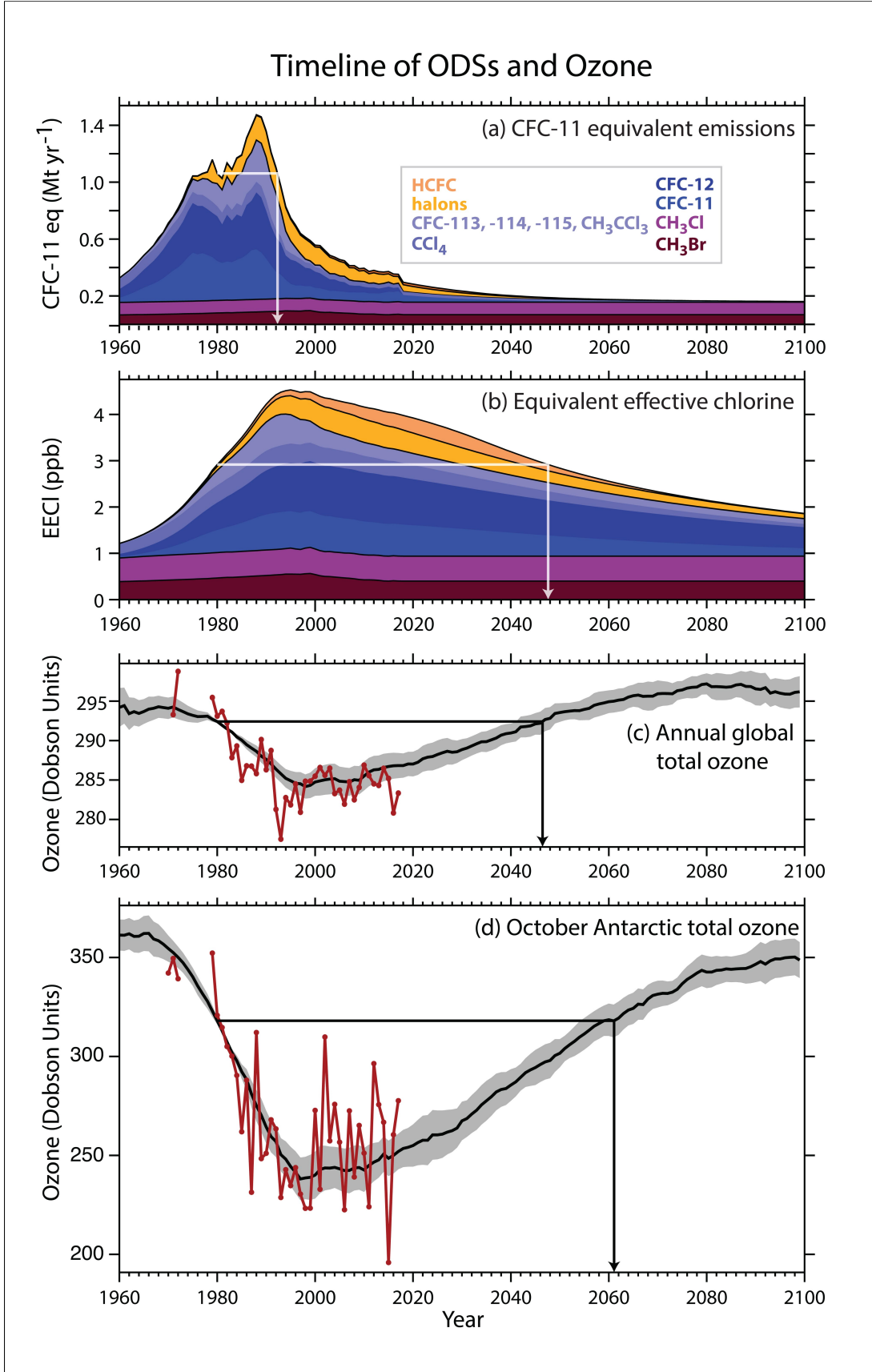


Figure 2.3: Timeline of: a) CFC-11-equivalent emissions, b) equivalent effective chlorine, c) global total ozone, and d) October Antarctic total ozone. Annual CFC-11-equivalent emissions are computed for the ODSs shown in the legend by multiplying mass emissions of a substance by its ODP. From [38].

emission of the major ODS: Chlorofluorocarbons (CFCs) and halons [40]. This achieved results in reducing ODS concentrations and reversing ozone depletion, as illustrated by Fig. 2.3.

Fig. 2.3 is taken from the 2018 Scientific Assessment of Ozone Depletion, produced by the National Oceanic and Atmospheric Administration of the US Department of Commerce, in coordination with the World Meteorological Organization (WMO) the United Nations Environment Programme (UN Environment). It depicts timelines for:

- a) CFC-11-equivalent emissions. Annual CFC-11 equivalent emissions are computed for the ODSs shown in the legend by multiplying the mass emissions of a substance by its Ozone Depleting Potential (ODP). The ODP is a metric for the relative strength of a chemical to destroy ozone, and is defined as the ratio of the change in global ozone for a given mass emission of the substance to the change in global ozone for the same mass emission of CFC-11. Therefore, CFC-11 equivalent emissions illustrate total emissions scaled by the threat they pose to the ozone layer.
- b) Equivalent effective chlorine. Annual EECl abundances are based on surface abundances (measured or derived from projected emissions and lifetimes) of the chlorine- and bromine-containing substances covered under the Montreal Protocol. Similarly to CFC-11 equivalent emissions, these values are scaled so that the amount shown is representative of the threat posed to the ozone layer. To this end, the bromine abundances are weighted by a factor of 65 to account for the greater efficiency of bromine in ozone destruction reactions in the atmosphere.
- c) Global total ozone. This represents an annual average over the latitudes 60°N to 60°S.
- d) October Antarctic total ozone. This represents an average over the latitudes 60°S to 80°S for the month of October. This is typically the time and region for which the Ozone hole is most pronounced.

The parties to the protocol meet annually to review it and have made six amendments since the Protocol's inception. These amendments included the introduction of restrictions on further ODS. The most recent amendment was the Kigali Amendment, which was registered on January 1, 2019 [41].

The Kigali amendment seeks to reduce the consumption and production of hydrofluorocarbons (HFCs). These substances were first introduced to replace CFCs in industrial products such as refrigerants following the creation of the original Montreal Protocol. Since HFCs do not contain chlorine, they do not contribute to the destruction of the ozone layer. However, it has been determined that they are powerful greenhouse gases and are making a significant contribution to climate change [42]. Although not ODS, they were added to the Montreal Protocol in an effort to reduce global warming by phasing them out. This is an unfortunate example of the Law of Unintended Consequences.

The ODS currently restricted by the Montreal Protocol are [43]:

- Chlorofluorocarbons (*CFCs*)
- Halon
- Carbon tetrachloride (CCl_4)
- Methyl chloroform (CH_3CCl_3)

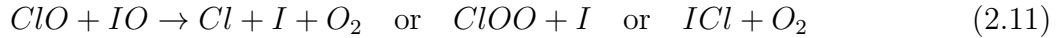
- Hydrobromofluorocarbons (*HBFCs*)
- Hydrochlorofluorocarbons (*HCFCS*)
- Methyl bromide (CH_3Br)
- Bromochloromethane (CH_2BrCl)

Although iodine is a member of the halogen family and a suitable catalyst for the catalytic decomposition of ozone, it is not included in the Montreal Protocol. This is because it is almost exclusively emitted naturally as opposed to anthropogenically, and we cannot control natural emissions.

2.3 Iodine Oxide

In the 1990s, Solomon et al. suggested that Iodine chemistry should be considered in studies of Ozone destruction mechanisms, particularly for the cases of rapid interhalogen reactions and/or total Iodine abundances of 1pptv [44]. Fig. 2.4 shows the rate of odd oxygen destruction calculated in this paper for 50°N in December 1990 based on a total atmospheric iodine concentration of 1 pptv.

The rapid ozone-depleting interhalogen reactions considered in this paper refer to catalytic cycles such as



where the possible products $ClOO$ and ICl rapidly thermally or photolytically decompose to reform halogen atoms and close the cycle [45]. Solomon estimated that such reactions would lead to ozone destruction pathways with rate constants of about $1 \times 10^{-10} cm^3 molecule^{-1} s^{-1}$ at stratospheric temperatures. For comparison, the catalytic ozone destruction cycle shown in equations 2.6, 2.7 and 2.8 with Cl as the catalyst X has an overall rate constant of approximately $1 \times 10^{-14} cm^3 molecule^{-1} s^{-1}$ at 298 K. This chemistry would imply that ozone destroying efficiency of iodine released in the stratosphere would be more than 1000 times greater than that of chlorine released there.

Subsequent work in the early 2000s estimated the amount of total iodine entering the stratosphere as below 0.15pptv [46] or 0.2 pptv [47]. DOAS measurements made in 2009 estimated the upper limits for the total gaseous inorganic iodine burden (Iy) as 0.09 to 0.16 ppt in the tropical lower stratosphere and 0.17 to 0.35ppt in the tropical upper troposphere [48]. As such, its contribution to stratospheric Ozone chemistry was considered negligible and therefore not assessed in much detail [49].

However, recent research indicates that significant levels of total reactive iodine (0.25–0.7 parts per trillion by volume) can be injected into the stratosphere via tropical convective outflow. At these iodine levels, modelled iodine catalytic cycles account for up to 30% of the contemporary ozone loss in the tropical lower stratosphere [50]. Additional modelling supported that the influence of iodine on ozone loss is strongest in the lower stratosphere, causing

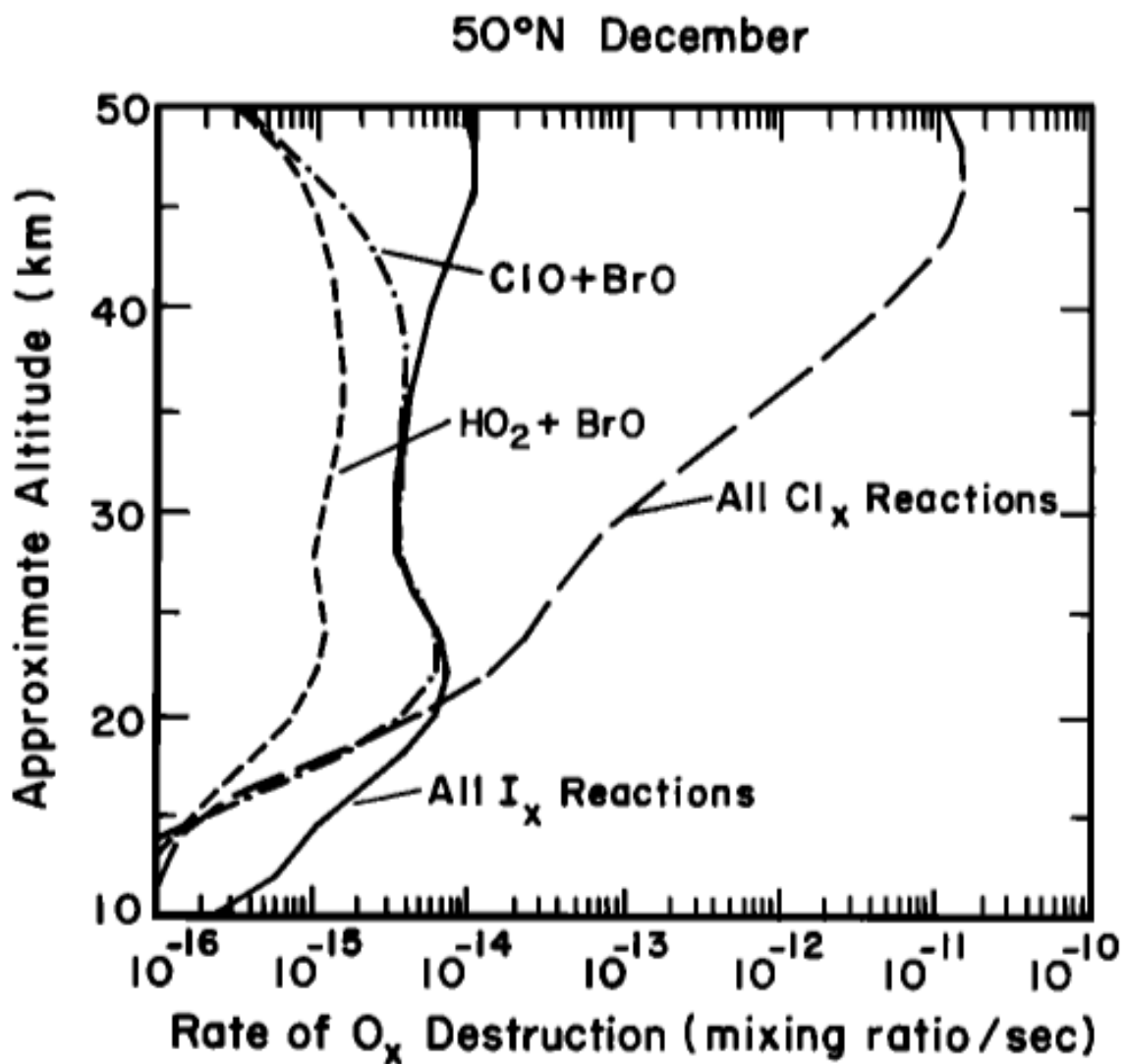


Figure 2.4: Calculated rate of odd oxygen destruction for 50°N in December 1990 for different chemical processes assuming 1pptv of total iodine. From [44]

30 ppbv less ozone at low latitudes and up to 100 ppbv less at high latitudes within this region [51].

Direct measurements of IO and particulate iodine in the upper troposphere and lower stratosphere, in combination with models, support that 0.77 ± 0.10 parts per trillion by volume (pptv) of total inorganic iodine (both gas and particulate phase) enters the stratosphere via tropical convective outflow. At these levels, iodine is responsible for 32% of the halogen-induced ozone loss (bromine for 40%, chlorine for 28%), mainly due to previously unconsidered heterogeneous chemistry [2]. The relative contribution of iodine to future stratospheric ozone loss is also likely to increase as anthropogenic chlorine and bromine emissions decline following the Montreal Protocol.

However, there is still high uncertainty in the role of atmospheric iodine chemistry as compared with bromine chemistry due to a lack of widespread ground or satellite-based observations [3]. The results quoted above are each based on only one measurement point, so more measurements are needed to verify the findings and draw robust conclusions.

Chapter 3

Differential Optical Absorption Spectroscopy

Differential Optical Absorption Spectroscopy (DOAS) is the method by which column abundances of trace species are derived from measurements of electromagnetic radiation in a specified spectral interval [15]. The method is an inversion technique, which retrieves the Slant Column Density (SCD), aka the total number density of absorbers along the light path L, from the measured spectra [4].

The continuous wavelength sampling of DOAS instruments in typically hundreds of spectral channels allows the detection of much weaker absorption features, and thus a higher sensitivity, than previous methods of analysing atmospheric composition by scattered sunlight absorption spectroscopy. This is because the differential absorption pattern of the trace gas cross-section is unique for each absorber and its amplitude can be readily determined by a fitting procedure to separate the contributions of the individual absorbers; enabling the simultaneous measurement of several absorbers while cross-interferences and the influence of Mie scattering are virtually eliminated [52].

These results can then be used together with some forward model of the photons' path from the Sun through the atmosphere to the instrument to retrieve trace gas profiles. The basic principle behind DOAS is the separation of narrowband and broadband spectral structures in differential spectra, allowing for the detection of changes in narrowband absorption caused by the target gases.

3.1 Atmospheric Absorption of Light

The guiding principle behind air monitoring spectroscopic techniques is to make use of the absorption or emission of electromagnetic radiation by matter. Emission spectra are measured in the far-infrared, and another instrument called GLORIA attached to the same measurement balloon used in the Kiruna campaign was used to measure the emission spectra of trace gases in the atmosphere. However, this project focuses on absorption spectra, which are typically measured for the UV/VIS spectral regions.

Absorption of electromagnetic radiation by matter can be expressed quantitatively by the Beer-Lambert Law:

$$I(\lambda) = I_0(\lambda) \exp(-L\sigma(\lambda)c) \quad (3.1)$$

where $I_0(\lambda)$ represents the intensity of the initial radiation emitted, and $I(\lambda)$ the intensity

of the radiation after passing through a layer of thickness L, with the absorbing species to be measured of absorption cross-section $\sigma(\lambda)$ at wavelength λ present at concentration c [53].

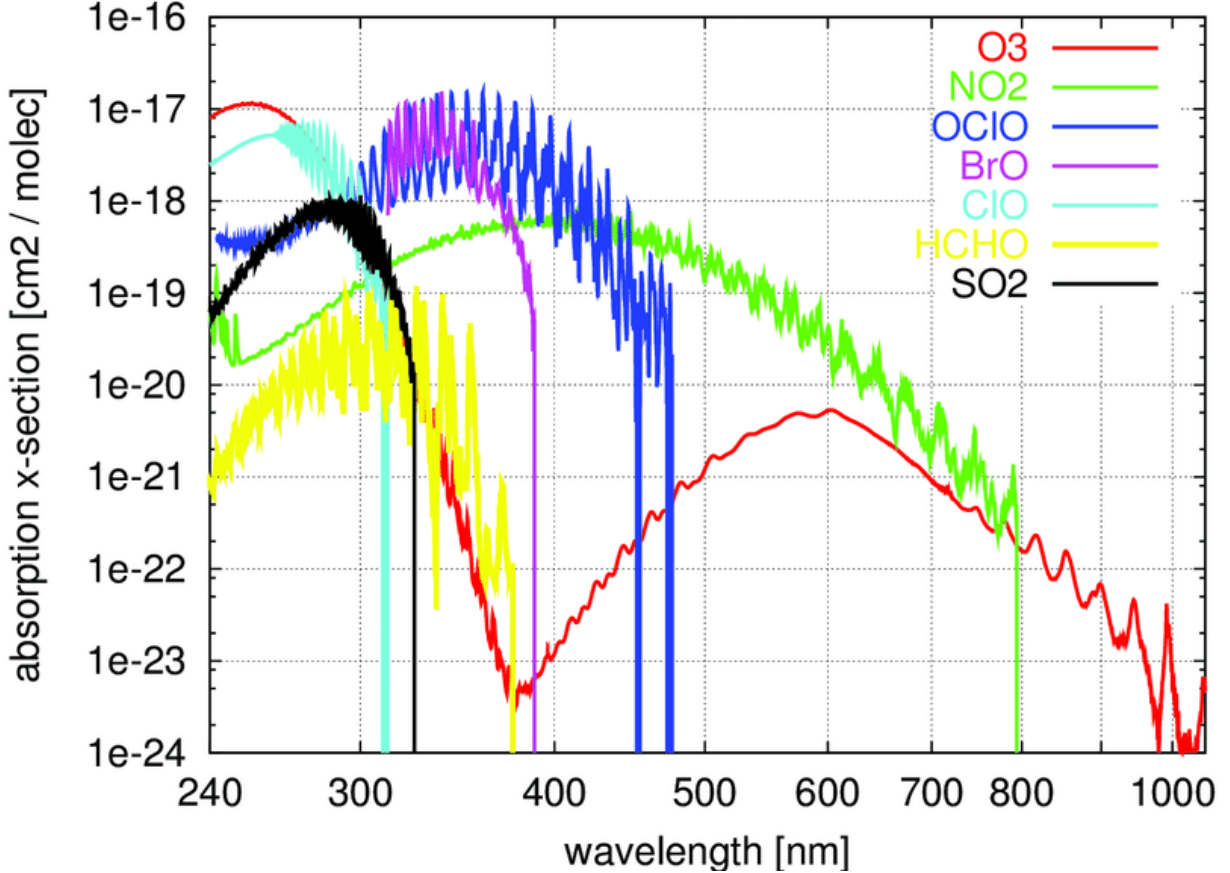


Figure 3.1: Absorption cross-section of trace gases in the UV-vis spectral region. From [54]

The absorption cross-section is a characteristic property of any species and can be determined experimentally. Some reference absorption cross-sections for atmospheric trace gases are shown in Fig. 3.1. This information can be used alongside the determination of the light path length L to determine the trace gas concentration according to

$$c = D/(\sigma(\lambda)L) \quad (3.2)$$

where D represents the optical density $\log(I_0(\lambda)/I(\lambda))$ of a layer of a given species. This equation neglects other causes of light extinction in the atmosphere, such as Rayleigh and Mie scattering.

3.1.1 Rayleigh Scattering

Rayleigh scattering in this context refers to the scattering of light by air molecules. Although it is not an absorption process, the light scattered out of the probing light beam will generally not reach the detector, so for spectroscopic purposes, it can be treated as such. This simplified Rayleigh absorption cross-section can be written as

$$\sigma_R(\lambda) = \sigma_{R0} \cdot \lambda^{-4} \quad (3.3)$$

where σ_{R0} is approximately $4.4 \times 10^{-16} \text{ cm}^2 \cdot \text{nm}^4$ for air. The exact value of σ_{R0} is irrelevant in our case, as our measurements are broadband.

Therefore, the Rayleigh extinction coefficient is given by

$$\epsilon_R(\lambda) = \sigma_R(\lambda) \cdot c_{AIR} \quad (3.4)$$

where c_{AIR} represents the concentration of air molecules [55].

3.1.2 Mie Scattering

Mie scattering refers to "The elastic scattering of light from atomic and molecular particles whose diameter is larger than about the wavelength of the incident light" [56]. For atmospheric absorption purposes, this is scattering from aerosol particles. Following similar arguments as for Rayleigh scattering, it can be treated as an absorption process with an extinction coefficient given by

$$\epsilon_M(\lambda) = \epsilon_{MO} \cdot \lambda^{-n} \quad (3.5)$$

with n in the range 1 - 4 [57].

3.1.3 Atmospheric Absorption

Including absorption cross-sections to represent scattering effects, atmospheric absorption in the presence of a single trace gas species can be expressed as

$$I(\lambda) = I_0(\lambda) \exp[-L(\sigma(\lambda)c) + \epsilon_R(\lambda) + \epsilon_M(\lambda)] \quad (3.6)$$

As the natural atmosphere contains a variety of trace gas species, the equation 3.6 must be extended to:

$$I(\lambda) = I_0(\lambda) \exp[-L(\sum_i (\sigma_i(\lambda)c_i) + \epsilon_R(\lambda) + \epsilon_M(\lambda))] \quad (3.7)$$

where $\sigma_i(\lambda)$ and c_i represent the absorption cross section and the concentration of the i^{th} species. Theoretically, all gases present in the atmosphere could be included in this formula. However, generally only a few will show significant absorption cross-sections in a given wavelength range, making the remainder unimportant for that range. Therefore, the equation can be simplified by only including those gases with significant absorption cross-sections for the considered range.

3.2 Atmospheric Spectroscopy

When performing spectroscopic measurements using light emitted by the Sun as the source, it is difficult to determine the true intensity $I_0(\lambda)$ which would be received in the absence of any absorption. To circumvent the issue of not having a top-of-the-atmosphere spectrum (recorded with our instrument, because in the era of satellites there certainly are spectra of other instruments recorded at the top of the atmosphere, eg. Kurucz [58]) we use one spectrum with a shorter light path as a reference spectrum.

The absorption cross-section of a given molecule can be split into two segments:

$$\sigma_i(\lambda) = \sigma_{io}(\lambda) + \sigma'_i(\lambda) \quad (3.8)$$

where $\sigma_{io}(\lambda)$ and $\sigma'_i(\lambda)$ represent slow and fast variations with λ respectively. Extinction due to Rayleigh and Mie scattering can be assumed to fall into the $\sigma_o(\lambda)$ category. Rapid variation is generally caused by features such as absorption lines.

The splitting of the cross section into differential cross section and broadband features is used to simplify the fit, as broadband structures can be described by a polynomial. Introducing this segmented definition of the absorption cross-section into equation 3.7 gives

$$I(\lambda) = I_0(\lambda) \cdot \exp[-L \sum (\sigma'_i(\lambda)c_i)] \cdot \exp[-L \sum (\sigma_{io}(\lambda)c_i + \epsilon_R(\lambda) + \epsilon_M(\lambda))] \cdot A(\lambda) \quad (3.9)$$

Where $A(\lambda)$ represents the attenuation factor, i.e. the wavelength-dependent transmission of the optical system used. The first exponential term of equation 3.9 summarised the effect of the structured 'differential' absorption of trace species, and the second their slowly varying absorption, as well as the influence of Mie and Rayleigh scattering.

From this we define I'_0 as the intensity in the absence of differential absorption:

$$I'_0 = I_0(\lambda) \cdot \exp[-L \sum (\sigma_{io}(\lambda)c_i + \epsilon_R(\lambda) + \epsilon_M(\lambda))] \cdot A(\lambda) \quad (3.10)$$

This quantity can be interpolated from the light intensity at either side of a sufficiently narrow absorption line of the species. A differential optical density can also be defined as

$$D' = \log(I'_0(\lambda)/I(\lambda)) = L \sum (\sigma'_i(\lambda)c_i) \quad (3.11)$$

The species concentration can then be determined from these measurable quantities according to

$$c = D' / (\sigma'(\lambda)L) \quad (3.12)$$

using the reasoning behind equation 3.2. This technique can only be applied to species whose spectra contain reasonably narrow absorption features, and in regions where Rayleigh scattering does not dominate.

3.2.1 Real Measurements

Measured spectra are recorded by a discrete detector with a finite resolution, which can be represented as the convolution of the high-resolution spectrum $I(\lambda)$ with the instrument line shape $g(\lambda)$:

$$I^{obs}(\lambda) = \int_{-\infty}^{\infty} I(\lambda')g(\lambda - \lambda')d\lambda' = (I \circledast g)(\lambda) \quad (3.13)$$

When using the Sun as a light source, the measured spectra exhibit significant wavelength dependence as well as absorption features such as Fraunhofer lines. To account for instrumental effects and Fraunhofer lines, a spectrum recorded at a low SZA ($I_{0,b}^{obs}$) is used as the reference I_0 . Ultimately, DOAS aims to model a function which replicates the measured spectra. This model function is constructed as

$$F(\lambda) = \ln I_0^{obs}(\lambda) - \sum a_i(\sigma_{i,n} \circledast g) + P_k(\lambda) \quad (3.14)$$

where P_k represents a polynomial of order k that accounts for all broadband extinction effects. To produce results, the absorption cross-sections of all relevant absorbers and the instrument line shape g must be known.

As mentioned previously, the reference spectrum used in this application of DOAS already includes some extinction due to absorption by the target species for each examined atmospheric component, which is referred to as the Fraunhofer Offset. The retrieved SCD values only give the SCD above the level measured by the reference spectrum and are subsequently labelled differential Slant Column Density ΔSCD , where

$$\Delta SCD = SCD - SCD^{frh} \quad (3.15)$$

3.3 Langley's Method

The method above retrieves differential Slant Column Densities ($\Delta SCDs$). The Slant Column Density (SCD) can be calculated from these values according to

$$SCD_i = \sum_j^m AMF_{ij} VCDair, j \quad (3.16)$$

where $VCDair, j$ represents the vertical air column density of each height layer, which is calculated from the air density profile using the program DAMF. This method assumes a constant Volume Mixing Ratio (VMR) of the trace gas within each j of m layers.

The Air Mass Factor (AMF) provides a scaling of the light path within each layer. Only the few layers above the balloon are important, as the number of molecules decreases exponentially with height, and thus also the contribution of higher layers to the VCD. Equation 3.16 is valid for both the total air mass and the trace gas SCDs.

Combining this with the expression for $\Delta SCDs$ given in 3.15 gives

$$\Delta SCD_i = \sum_j^m AMF_{ij} VCDj - SCD^{frh} \quad (3.17)$$

The same reference is used in the retrieval for each species i . However, the Fraunhofer offset is different for each species, as there might be more ozone in the reference spectrum than nitrogen dioxide or iodine.

If we then assume that the AMF is constant for all layers considered, equation 3.17 can be further simplified to

$$\Delta SCD_i = AMF_i \sum_j^m VCDj - SCD^{frh} \quad (3.18)$$

Applying the same simplification to the retrieved slant column density of air (via equation 3.16) gives the AMF for each layer via:

$$AMF_i = \frac{SCD_i^{air}}{\sum_j VCD_j^{air}} \quad (3.19)$$

By combining equations 3.18 and 3.19 and replacing $\sum_j VCD_j^{air}$ with the total vertical column density of the air overhead VCD^{air} , the retrieved dSCDs can be represented in a linear form:

$$\Delta SCD_i = \frac{\sum_j VCD_j}{VCD^{air}} \cdot SCD_i^{air} - SCD^{frh} \quad (3.20)$$

As discussed previously, the slope and offset are independent of each measurement i . As a result, a linear regression fit using all n measurements provides the overhead VMR and the Fraunhofer offset of the considered species [59]. The total Slant Column Densities for air required for these 'Langley Plots' are calculated from atmospheric properties and the SZA for each data point.

The method relies on the assumption of a constant AMF, which becomes worse for higher SZAs. Accordingly, a Langley evaluation should only consider spectra acquired for low SZAs [60].

3.4 Profile Retrieval

The observed slant column densities are linked to vertical column densities according to

$$\overrightarrow{SCD} = \mathbf{AMF} \times \overrightarrow{VCD} \quad (3.21)$$

where the measurement vector \overrightarrow{SCD} contains all n measurements.

The AMF matrix is calculated via a radiative transfer model which accounts for the complex viewing geometry during solar occultation. Regularised Singular Value Decomposition (SVD) is then applied to minimize the cost function and calculate the vertical column density within each layer according to

$$\overrightarrow{VCD_r} = (\mathbf{AMF}^T \mathbf{S}_e^{-1} \mathbf{AMF} + \alpha^2 \mathbf{1})^{-1} \mathbf{AMF}^T \mathbf{S}_e \times \overrightarrow{SCD} = \mathbf{G} \times \overrightarrow{SCD} \quad (3.22)$$

Where \mathbf{S}_e is the error covariance matrix and \mathbf{G} the gain matrix. The optimal regularization parameter α is obtained via the L-curve method.

The averaging kernel matrix A is given by

$$\mathbf{A} = \mathbf{G} \times \mathbf{AMF} \quad (3.23)$$

It describes the retrieval's information content and provides analytics of the inversion. Using \mathbf{A} and the true profile, the inversion error \overrightarrow{e} can be calculated according to

$$\overrightarrow{e} = \overrightarrow{VCD_r} - \mathbf{A} \times \overrightarrow{VCD_{true}} \quad (3.24)$$

3.5 Shortcomings and Corrections for DOAS Method

3.5.1 Centre to Limb Darkening

Photons originating from the upper edge of the solar disk have a longer path through the sun's atmosphere, than photons originating from the centre. this causes differences in the depths of some Fraunhofer lines for photons originating from different areas of the solar disk. Usually a constant fraction of photons from all these areas arrive at the spectrometer, but during sunset, the light path through the Earth's atmosphere has a significant difference for photons from the lower solar disk compared to the upper solar disk, leading to different fractions of photons arriving from the different areas. This causes changes in the spectrum of the Fraunhofer lines. An empirical correction for this center-to-limb darkening (CLD) effect is applied by calculating a pseudoabsorber cross-section for inclusion in the fit scenario via

$$\sigma_{CLD} = \frac{I_{disk} \circledast g - I_{centre} \circledast g}{I_{centre} \circledast g} \quad (3.25)$$

where I_{centre} is a high-resolution spectrum of the Sun's center, I_{disk} a spectrum averaged over the whole disk, and g the instrument line shape (ILS). This effect becomes more prominent for higher SZAs.

3.5.2 Ring Effect, Solar I_0 effect

Besides Centre to Limb Darkening, the quality of DOAS measurements is affected by two principal effects:

- 1 The contribution of inelastically scattered light (Raman scattering) to the total intensity leads to a modification that can be approximated as the filling in of the Fraunhofer lines. This effect complicates the complete removal of the Fraunhofer structures: it is usually called Ring effect [61].
- 2 The limited spectral resolution of a typical DOAS instrument leads to an interference of the Fraunhofer structures of the solar spectrum and the absorption cross-sections of the atmospheric trace gases. This is called the solar I_0 effect.

Ring Effect Correction

The measured spectrum (and in many cases also the Fraunhofer spectrum) is the sum of elastic scattering processes ('Rayleigh' and 'Mie scattering') and inelastic scattering processes (Raman scattering) [62]:

$$I = I_{\text{elastic}} + I_{\text{inelastic}} \quad (3.26)$$

Thus, by taking the ratio of these spectra (as required to calculate concentration in the DOAS method), the Fraunhofer structures of the measured spectrum are not fully removed. Especially in the UV spectral range, the remaining spectral structures (up to 10%) can by far exceed the absorption structures of weak atmospheric absorbers.

In most cases, the Ring effect can be approximately corrected for by considering an additional spectrum in the DOAS fitting process: the so-called Ring spectrum [63]. The logarithm of the measured spectrum can be approximated as

$$-\ln(I_{\text{measured}}) = -\ln(I_{\text{elastic}} + I_{\text{inelastic}}) \approx -\ln(I_{\text{elastic}}) + \frac{I_{\text{elastic}}}{I_{\text{inelastic}}} \quad (3.27)$$

where $\frac{I_{\text{elastic}}}{I_{\text{inelastic}}}$ gives the Ring Spectrum I_{ring} .

Solar I_0 Effect Correction

The spectral resolution of DOAS instruments in the UV/VIS region is typically in the range of about a few tenths to several nanometers. Thus, the natural line widths of solar and atmospheric absorptions tend not to be spectrally resolved [64].

The actually observed intensity $I * (\lambda)$ can be written as

$$I * (\lambda) = F * I(\lambda) = \int I(\lambda') \cdot f(\lambda - \lambda') \cdot \delta\lambda' \quad (3.28)$$

where $*$ indicates the convolution with the slit function of the instrument $f(\lambda)$. For the spectral retrieval, the cross-sections of the atmospheric absorbers are also convolved with this slit function.

Since the convolution and the logarithm can not be exchanged, a non-linearity between the observed optical depth τ and the column density $S = \sigma \cdot \rho l$ of the measured trace gas results. This effect, referred to as the saturation effect, is more prominent for stronger absorbers.

A second, more subtle effect also appears; an interference of the spectral absorption structures with the highly structured solar spectrum $I_0(\lambda)$. Dividing the measured spectrum by the Fraunhofer spectrum fails in totally removing the Fraunhofer structures, because the convolution and taking a ratio cannot be exchanged. Since this effect arises from the spectral structure of the solar spectrum $I_0(\lambda)$ it is referred to as ‘ I_0 effect’ [65].

It can be corrected for by using modified absorption cross-sections. To calculate these, a highly resolved solar spectrum $I_0(\lambda)$ is convolved with the instrument function. A modelled absorption spectrum (calculated from the highly resolved solar spectrum and a highly resolved absorption cross section) is then convolved with the instrument function. For the latter, an atmospheric column density S has to be assumed. The I_0 corrected cross section is then derived as:

$$\sigma_{corrected}(\lambda, S) = \frac{-\ln \frac{I*(\lambda, S)}{I_0 * \lambda}}{S} \quad (3.29)$$

These I_0 corrected cross sections can only match the absorptions in the measured atmospheric spectrum perfectly if the S used for the calculation matches the atmospheric S . Usually the maximum values of typically occurring atmospheric S are assumed for the determination of the corrected cross sections.

Chapter 4

Experimental Techniques

4.1 TotalBro Instrument

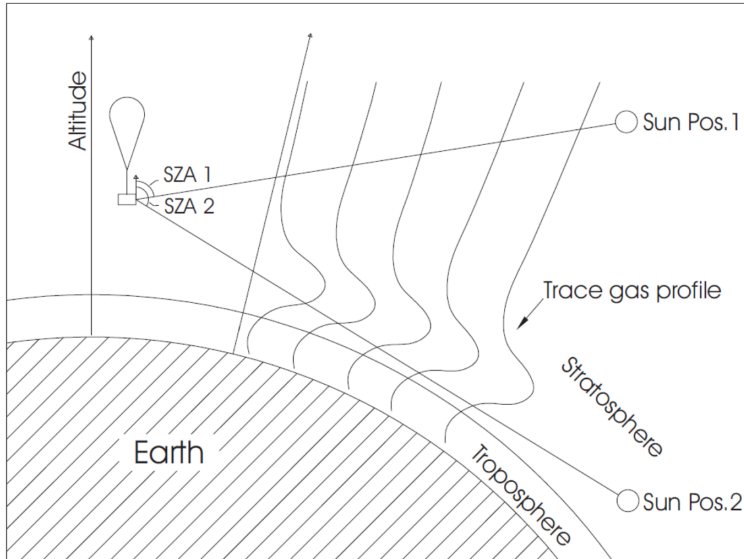


Figure 4.1: Solar Occultation viewing Geometry utilised to reveal information about trace gas distributions. From [5]

gondola is kept constant by rotating the gondola during the flight, thereby keeping the sun's azimuth angle fixed as seen by the solar tracker. The altitude, on the other hand, is not controlled by the gondola but only by the tracker. This results in the pointing angle of the gondola increasing as the Sun moves from East to West.

To obtain the vertical information required for DOAS, the sunlight gathered by the instrument must pass through different layers of the atmosphere. This is achieved by gathering direct sunlight during sunset. Mounting the spectrometer on a balloon makes it possible to track the Sun below the horizon at SZAs greater than 90° , resulting in tangent heights (altitude for which the local SZA is 90° and the Sun's rays are therefore parallel to the Earth's surface) well below float altitude. This method is called solar occultation and is illustrated in Fig. 4.1.

The solar spectra analysed in this project were collected by the Total-BrO instrument, which is composed of an active solar tracker (detailed in [5]) and a spectrometer unit (developed by [66]) with two optical temperature stabilized grating spectrometers for the UV and visible spectral ranges. The instrument is designed for solar occultation viewing geometry, so the recorded data can be used to infer a vertical profile for Iodine Oxide.

The solar tracker contains two moveable mirrors mounted in an Altazimuth orientation: the primary is variable in altitude, the secondary in Azimuth. Angles seen by the tracker are relative to the pointing of the tracker as the instrument moves throughout the campaign, making cardinal frame measurements unfeasible. The azimuth of the Sun to the

The tracker is equipped with two independent telescopes, the optics of which are adapted such that one feeds sunlight from the UV (300 - 400nm) spectral range, the other from the visible (400 - 500nm) range, into the separate glass fibres and corresponding spectrometers that are attached to them. These two Ocean Insight QE-Pro reflection grating spectrometers are housed within an evacuated box and temperature stabilized to 0°C by a surrounding ice-water bath, as illustrated in Fig. 4.2.

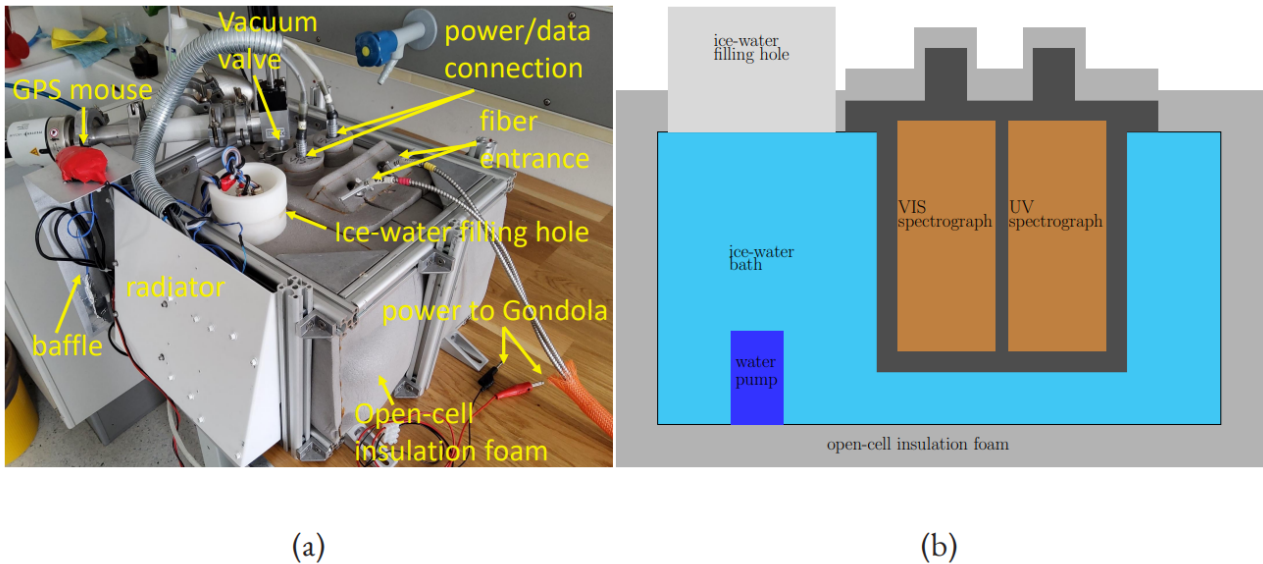


Figure 4.2: (a) shows the spectrometer unit from the outside, and (b) a diagrammatic cross-section. From [4]

The optical system of the spectrometers is shown in Fig. 4.3. The detector used in both is a back-thinned FFT-CCD (Hamamatsu S7031-1006S), i.e., a Full Frame Transfer Charged Coupled Device. The key elements of the detector are illustrated by the numbers 1 - 8, where these labels correspond to:

- 1) SMA Connector. Secures the input fiber to the spectrometer. Light from the input fibre enters the optical bench through this connector.
- 2) Interchangeable Slit. A dark piece of material containing a rectangular aperture, which is mounted directly behind the SMA Connector. The size of the aperture regulates the amount of light that enters the optical bench and controls spectral resolution.
- 3) Filter. Restricts optical radiation to pre-determined wavelength regions. Light passes through the Filter before entering the optical bench.
- 4) Collimating Mirror. Focuses light entering the optical bench towards the Grating of the spectrometer. Light enters the spectrometer, passes through the SMA Connector, Slit, and Filter, and then reflects off the Collimating Mirror onto the Grating.
- 5) Grating. Diffracts light from the Collimating Mirror and directs the diffracted light onto the Focusing Mirror. Gratings are available in different groove densities, to give a specified wavelength coverage and resolution in the spectrometer.

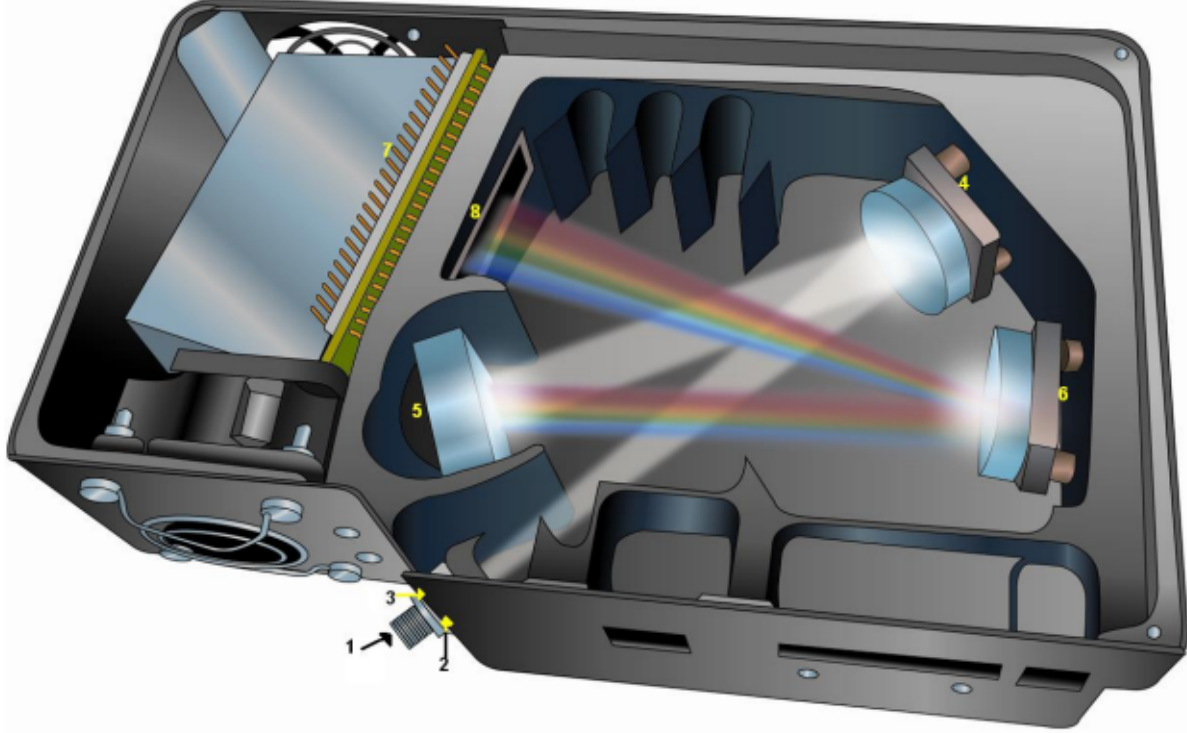


Figure 4.3: The QE Pro Spectrometer with components numbered. From [67]

- 6) Focusing Mirror. Receives light reflected from the Grating and focuses the light onto the CCD Detector or L2 Detector Collection Lens (depending on the spectrometer configuration)
- 7) Back-thinned Area Detector with TE Cooling. Provides 90% quantum efficiency and bins pixels in a vertical column to acquire light from the entire height of the spectrometer's slit image. This improves light collection and signal-to-noise significantly. The 2D area detector is back-thinned (back-illuminated).
- 8) Detector with OFLV Filter. Eliminates second-order effects and is used with an HC-1 Grating in a 200-950 nm wavelength system in a QE Pro.

Photons hit the detector and excite electrons into the potential wells of the detector pixels via the photoelectric effect. The number of electrons N_e excited per photon is determined by the quantum efficiency Q_e according to

$$Q_e = \frac{N_e}{N_p} \quad (4.1)$$

where N_p represents the number of photons. During the readout process, the number of electrons is determined by measuring the voltage. The analog-to-digital converter (ADC) converts the electron counts/voltages to anaolg-digital units (ADUs), which are saved in the spectra.

Data were collected during a stratospheric balloon flight in August 2022 launched in Timmins, ON, Canada.

4.2 Instrument Calibration

A constant voltage offset is applied during the readout process to avoid the inclusion of negative signals, which cannot be processed. This offset can be measured for a darkened slit entrance using very short integration times. The mean offset spectra obtained after the campaign is shown in Fig. 4.4.

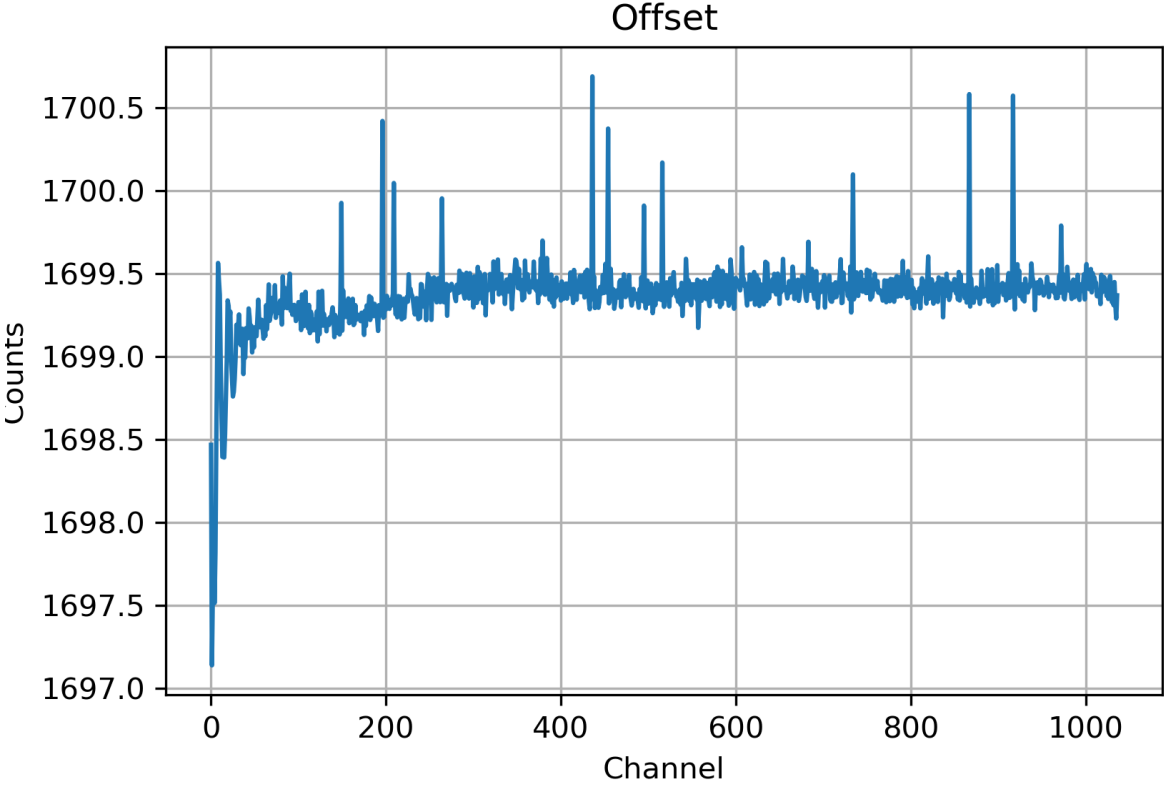


Figure 4.4: Mean offset spectra (integration time 10ms) from 4998 coadded scans.

Even when there is no photon flux incident on the detector, some current will still flow - this is defined as 'dark current' [68]. This effect occurs due to spontaneous thermal fluctuations within the detector, which have enough energy to generate electrons in the same way that photons do. These electrons are not part of the signal, but there is no way to distinguish them from the signal in the detector, so they become a source of noise. The dark current is the rate at which these thermal electrons are generated.

The dark current is always present, even without light, which is why it is referred to as "dark." Each pixel has a different amount of dark current, but it is usually stable over time, so it can be accounted for by acquiring a mean dark current spectrum from several coadded spectra taken over long integration times and subtracting this from further measured spectra [69]. A dark current spectrum for the instrument is acquired using an integration time of 60 seconds while the spectrometer is covered. The mean dark current obtained from coadding 13 such spectra is shown in Fig. 4.5. This dark current spectrum is already corrected for offset.

Using the aforementioned dark current and offset spectra D and O, each measured spectrum I is corrected using its corresponding number of scans and integration time I_{intt} according to

$$I^{corr}(\lambda) = I^{raw}(\lambda) - O(\lambda) \cdot \frac{I_{Scans}}{O_{Scans}} - (D(\lambda) - O(\lambda)) \cdot \frac{D_{Scans}}{O_{Scans}} \cdot \frac{I_{Scans}}{D_{Scans}} \cdot \frac{I_{intt}}{D_{intt}} \quad (4.2)$$

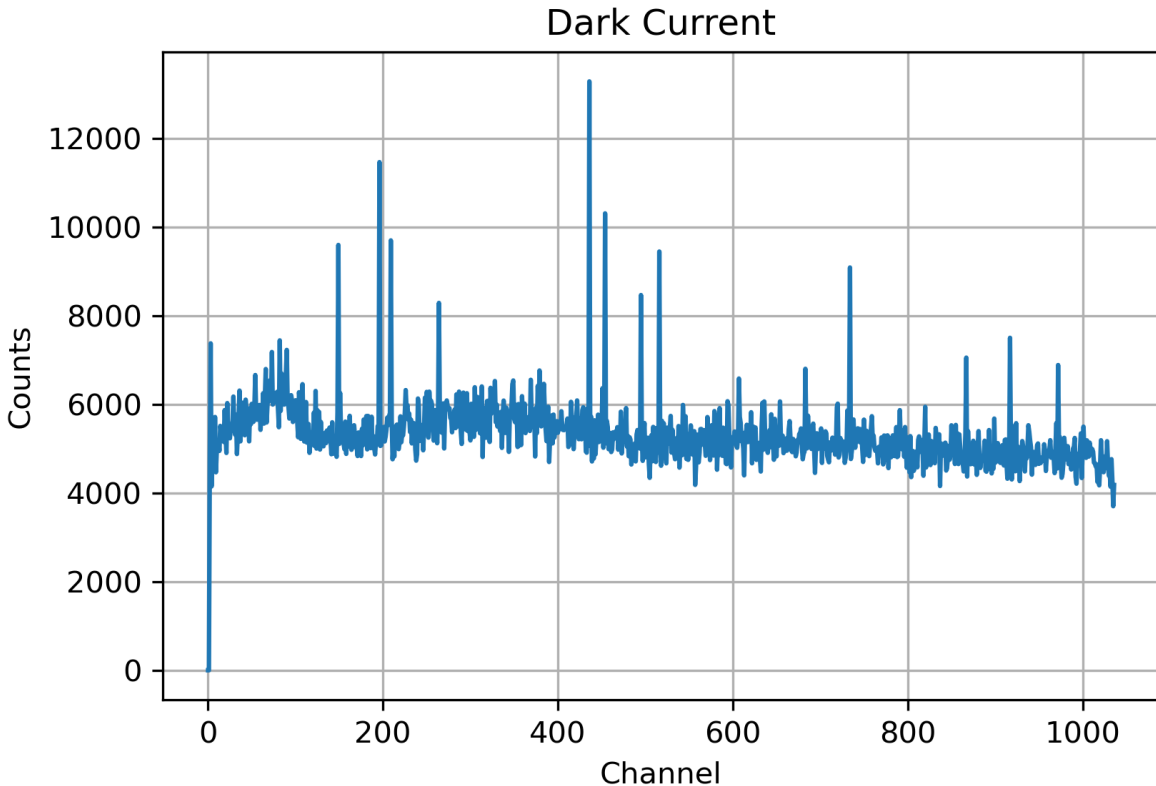


Figure 4.5: Mean dark current spectra (integration time 60s) from 13 coadded scans, corrected for offset.

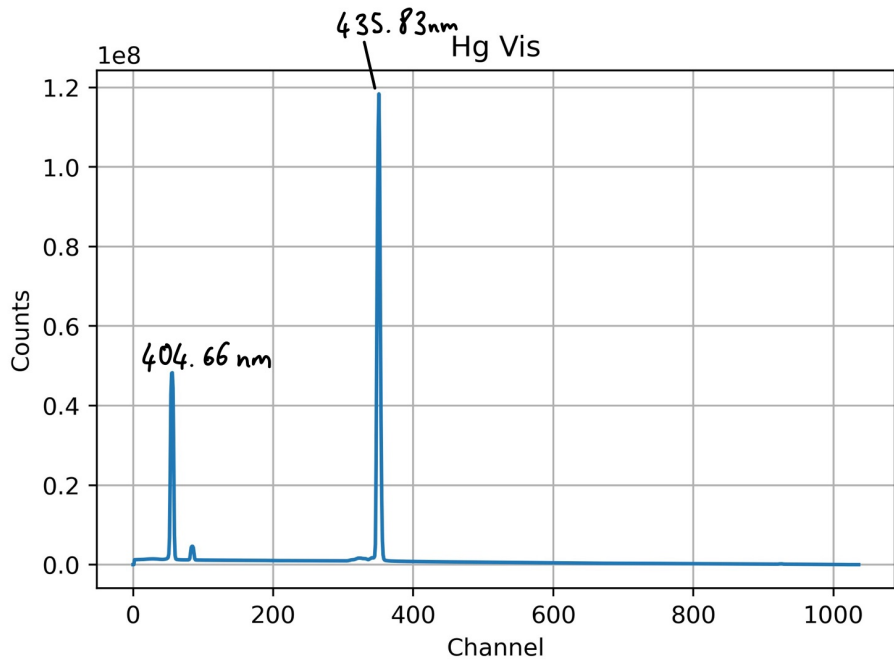
The spectrometer resolution and calibration is determined in several lab measurements prior to and following data collection using a mercury (UV and VIS) and Krypton (VIS) Pen-ray emission lamp. These lamps produce very finely tuned spectra via atomic transitions [70], with linewidths far narrower than the VIS spectrometer's resolution. The spectra recorded from these lamps by the instrument after its return from the campaign are shown in 4.6, having been corrected for dark current and offset according to equation 4.2.

These spectra are used for preliminary wavelength calibration by fitting Gaussians to their peaks, and then linking the peak value returned by the Gaussian fit to the literature wavelength of the respective emission peak. The wavelength corresponding to each peak is determined by close comparison to the structures shown in reference spectra.

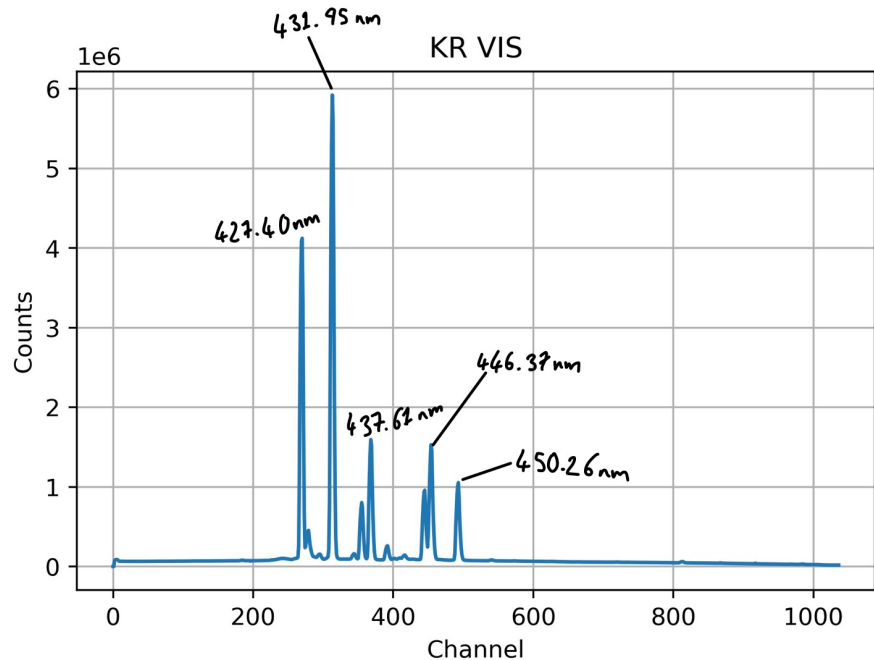
The wavelength corresponding to each peak used for calibration is shown in Fig. 4.6. Some peaks were not used in the fitting procedure as they result from two emission lines very close together, to the point where our instrument is incapable of resolving them separately. As it is not possible to attribute a precise wavelength value to these peaks, they cannot be used in the calibration fit.

The spectrometer is then calibrated by a linear fit of the wavelengths of the known Hg and Kr peaks against their channel numbers, as shown in 4.7. The fit was performed using the `scipy.optimize.curve_fit` function, which uses non-linear least squares to fit a function f , in this case given as $y = mx + b$ to data. The fit errors returned for m and b were 0.6% and 0.05% respectively, indicating a very good fit quality.

Evaluation of the Full Width Half Maximum (FWHM) of the spectral structures caused by single-emission peaks also enables determination of the resolution of the spectrometer and the



(a) Hg Spectrum and Peak Wavelengths



(b) Kr Spectrum and Peak Wavelengths

Figure 4.6: Hg and Kr Spectra taken by the instrument following its return from the campaign. These spectra are corrected for Offset and Dark Current. Peaks are annotated with the wavelength value they correspond to.

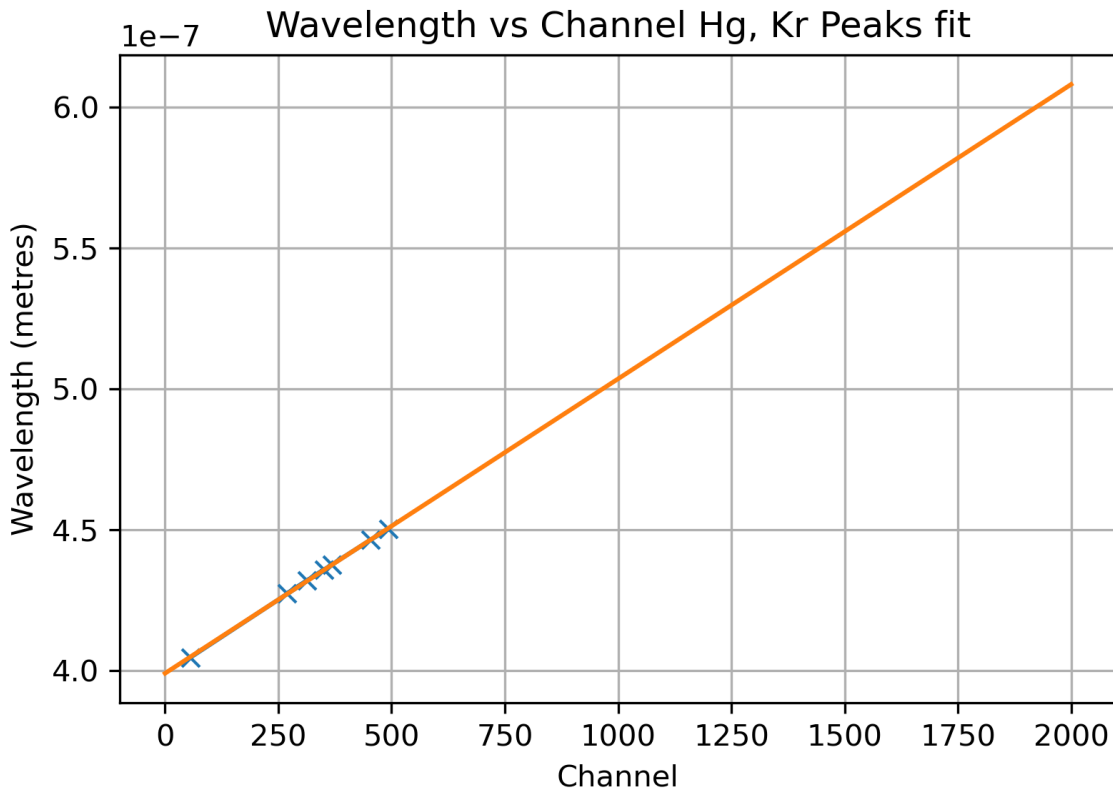


Figure 4.7: Fit of spectral feature wavelength value against channel number for calibration. The fitted function is $y = mx + b$, with the parameters $m = (1.05 + / - 0.006)e - 10$ and $b = (3.99 + / - 0.002)e - 07$ as determined by scipy's curve_fit function.

development of a convolution function to apply to literature spectra of the target gas absorption cross-sections, as the literature spectra are generally recorded at much higher resolutions than that of the present spectrometer.

An example of a Gaussian fit to the 435.58 nm Hg emission line to determine a FWHM and the channel number corresponding to this wavelength is shown in 4.8. The function used in the curve fitting program for each Gaussian fit was

$$y = \frac{Ce^{-x-x_{mean}^2}}{2\sigma^2} \quad (4.3)$$

The parameters retrieved by the fit shown in Fig. 4.8 were:

- $C = (1.20 + / - 0.01) \times 10^8$
- $X_{mean} = 350.69 + / - 0.01$
- $\sigma = 2.16 + / - 0.02$

This fit was particularly successful, producing very low uncertainty values; uncertainties on the fits to some other peaks were higher. However, all fits were successful in producing a Gaussian shape and returning values for the peak's channel value and FWHM.

As in the calibration process, only single-emission peaks were considered in calculating instrument resolution; the emission peaks which consist of two lines very close to each other

must be filtered out of FWHH calculations as they would give disproportionately large values, and could not be successfully resolved into a Gaussian fit.

Taking a mean of all functional Gaussian fits and applying Gaussian error propagation to sum all fit errors gave a sigma value of 2.5 ± 0.1 channels. The FWHM is given by 2σ , which corresponds to 5 ± 0.2 channels. Using the wavelength calibration discussed previously, this corresponds to an instrument resolution of (0.52 ± 0.02) nm.

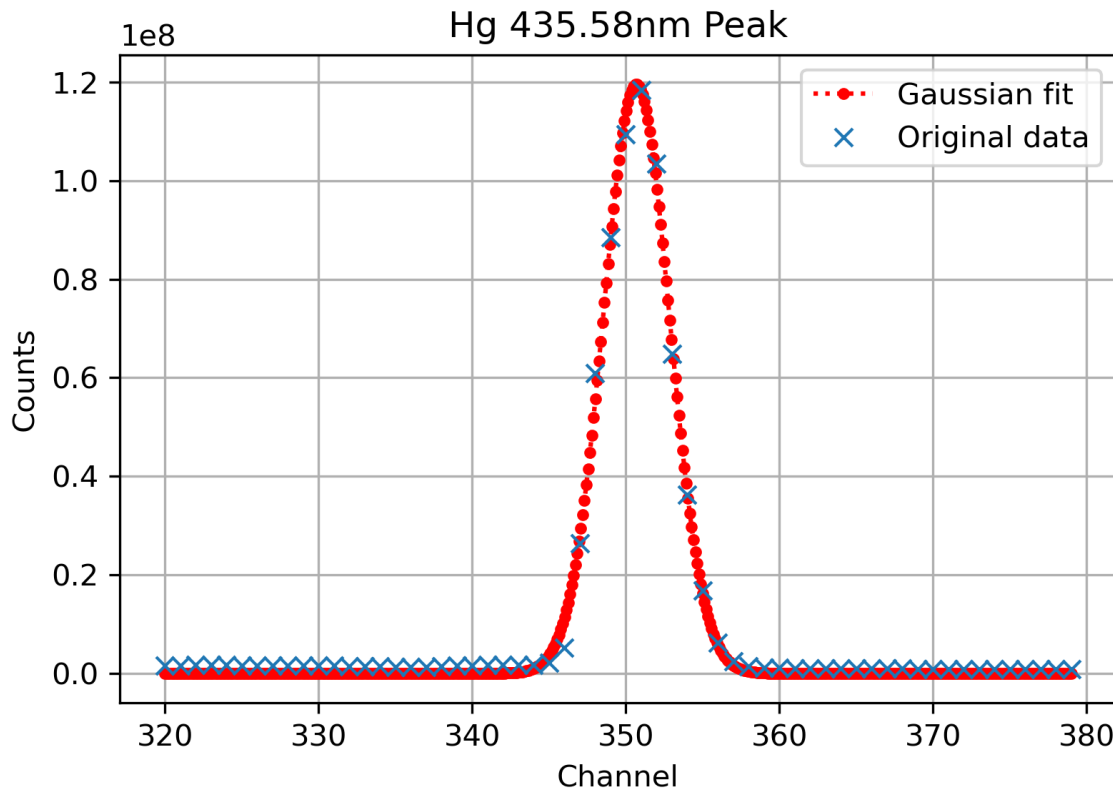


Figure 4.8: Example of a Gaussian fit to the 435.58 nm Hg peak to determine instrument resolution.

Chapter 5

QDOAS: Analysing Spectra

To increase the signal-to-noise ratio, several single spectra are coadded. Coadding up to 100 scans where possible gives a good compromise between noise and time resolution. Only spectra of the same integration time are coadded to ensure an exact DC and offset correction; as a result, not every data point is composed of 100 scans. For subsequent analysis, spectra with fewer than 30 scans are filtered out. This reduces the number of spectra analysed from 3856 to 3365. The number of scans coadded to produce each data point is shown in Appendix A.

The QDOAS software package developed by the Royal Belgian Institute for Space and Aeronomy is used to perform the DOAS retrieval of trace gases from these spectral measurements [7].

5.1 Fit Scenario

To achieve a reasonable DOAS retrieval, a suitable fit scenario must be constructed. The most significant parameters for the QDOAS program retrieval are:

- Wavelength range: Region for which spectral retrieval is carried out. The range covered should cover the significant absorption bands of the species being examined, and be within the range covered by the instrument used for data acquisition.
- Reference Spectrum: As described in Chapter 3, the I_0 spectrum which all other spectra are evaluated with respect to.
- Shift and Stretch: These parameters enable the correction of possible misalignment between the various wavelength-dependent quantities involved in the data evaluation (such as measured and reference spectra and absorption cross-sections). They may be fitted or applied to any wavelength-dependent quantity according to the equation

$$\Delta\lambda = a + b(\lambda - \lambda_0) + c(\lambda - \lambda_0)^2 \quad (5.1)$$

where λ is the wavelength according to the original calibration and λ_0 is the center wavelength of the current spectral range. Parameters a , b and c describe the offset, first-order stretch and second-order stretch applied to λ respectively [71].

- Polynomial Order: Order of polynomial to fit. In the DOAS technique, the absorption cross-sections of the considered molecules are highly structured, while scattering by

molecules and particles (Rayleigh and Mie Scattering) and surface reflection have broad-band dependencies that can be approximated by a low order polynomial. QDOAS allows the fitting of polynomials up to degree 8.

- Offset: Applied to correct for effects such as stray light in the spectrometer and other unaccounted for natural sources of offset. QDOAS models the offset using a polynomial

$$offset(\lambda) = (a + b(\lambda - \lambda_0) + c(\lambda - \lambda_0)^2)\bar{I} \quad (5.2)$$

where λ_0 is the center wavelength of the spectral analysis window, \bar{I} is the average intensity and a, b, c are fitted parameters.

- Ozone cross-section: Literature cross-section used for Ozone detection.
- NO_2 cross-section: Literature cross-section used for NO_2 detection.

The scenario implemented here is based on the IO retrieval scenario used by Bösch [72], which provides a starting point to determine the optimal parameter in each category. Each parameter is then varied around this point, or varied more extensively, to determine which value provides the best retrieval. The quality of the obtained retrievals is analyzed approximately by calculating the average Root Mean Square (RMS) residual after the fit. A closer evaluation is then carried out by examining the time series of the RMS; no distinct structures or wave-like behaviour should be present. The retrieved dSCD profile is also examined for significant structures or wave-like behaviour. Finally, the fits determined for each absorber cross section by the QDOAS program are examined to determine whether the absorbers are being found, i.e. the fit closely follows the structure of the cross section.

The best retrieval scenario is one which produces retrieved dSCDs with minimal wavelike structures, a low mean RMS with no significant structures, and fits to each pseudoabsorber cross-section which closely follow its structure. For each retrieval conducted, only one parameter was changed, so that the impacts of each change could be separated and evaluated. Certain parameter variations had a significant impact on the outcome of the retrieval and are examined in more detail, while others caused only minor change and are therefore not significant to determining the robustness of the retrieval.

5.1.1 Wavelength Range

The parameter determined to have the most significant impact on the retrieved IO dSCD values was the wavelength range. Bösch [46] used a fit window of 425 - 465 nm, so ranges similar to this were examined, with results displayed in Fig. 5.1. The figure shows the retrieved dSCD values for IO , O_3 and NO_2 , as well as the dSCDs calculated for the CLD pseudoabsorber cross-section, and the RMS for the total fit to the spectrum as a measure of quality. Low SZAs are shown in the plots on the left-hand side of the figure, and high SZAs on the right. The two sections are separated as the scale of the low SZA values is much smaller - plotting all values together makes it so that the wave-like behaviour at low SZAs cannot be seen. The low SZA dSCD retrieved values are mostly noise, but the level of wave-like behaviour and the presence of structures in the residual provides an indication of fit quality (the lower the waviness and the fewer prominent structures, the better)

Ultimately, the wavelength range 425 - 465 nm produced the best results, as evidenced by the far lower RMS values displayed for SZA 85° - 95° when this fit window is used, as well as the less intense wavelike behaviour shown for the low SZAs with this fit window.

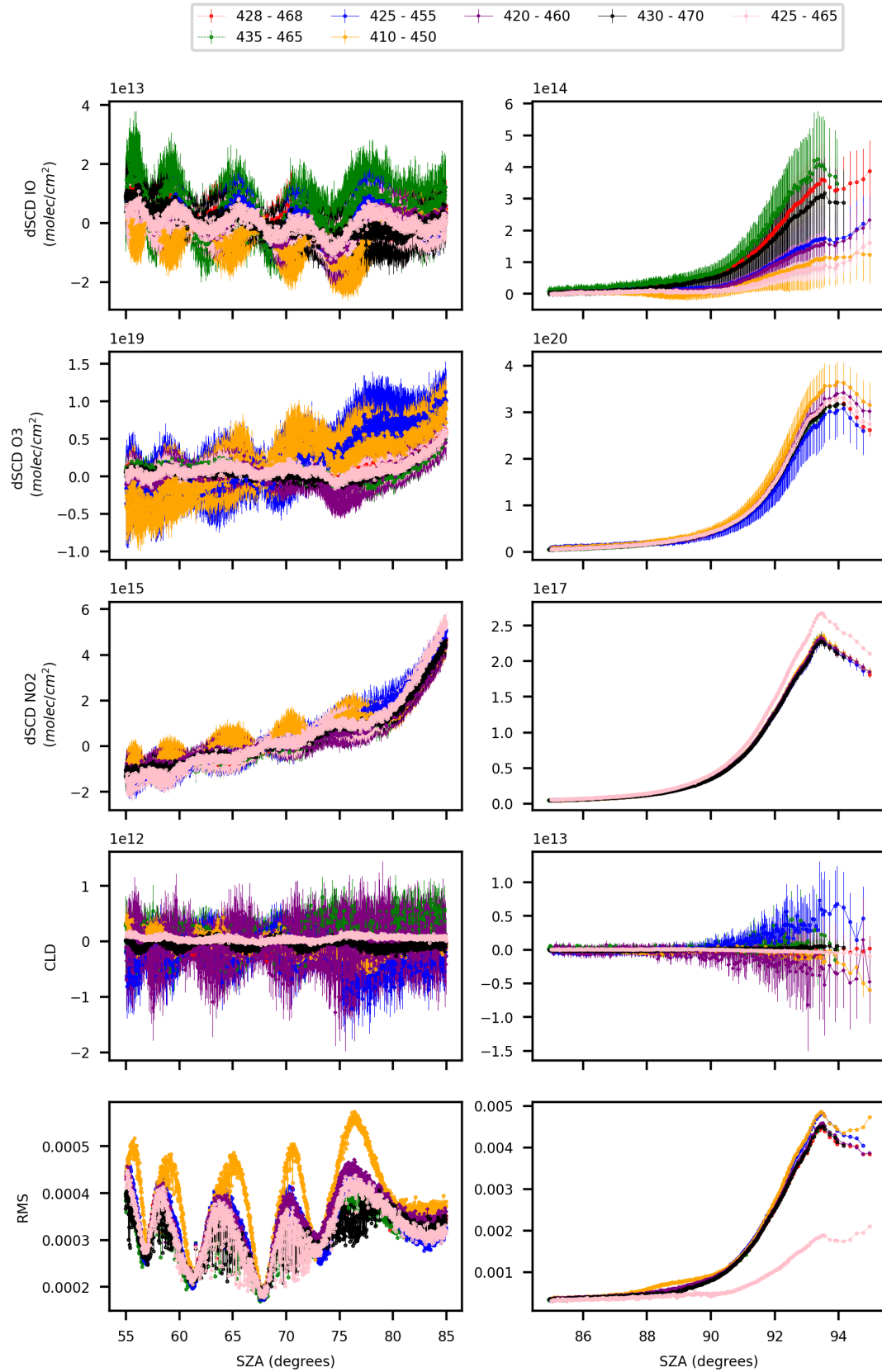


Figure 5.1: Retrieved dSCDs for IO, O_3 , and NO_2 , along with CLD and RMS for various wavelength fit windows. The wavelength fit range corresponding to each figure is displayed in nanometres in the legend. The wavelength range 425 - 465 nm produced the best results, as evidenced by the far lower RMS values displayed for SZA 85° - 95° (the figures on the right hand side) when this fit window is used.

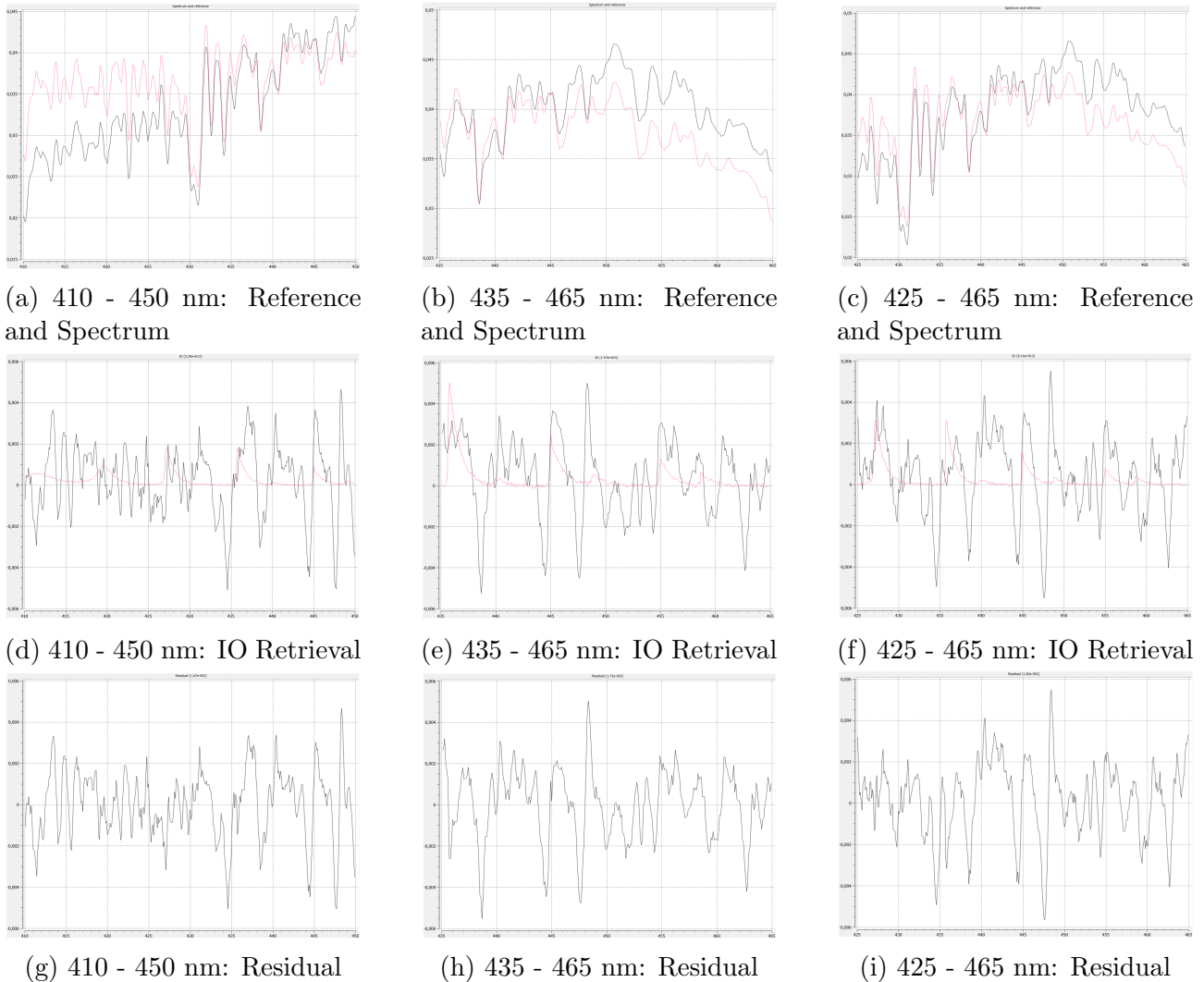


Figure 5.2: Spectrum (red) and Reference (black), IO cross-section retrieval, and Residual as output by the QDOAS program for the wavelength ranges 410 nm - 450 nm (on the left), 435 nm - 465 nm (in the middle) and 425 nm - 465 nm (on the right). For the IO absorber cross section retrieval (middle row), the red line represents the respective fit coefficient times the cross section, and the black line represents the red curve plus the residual

The retrieved CLD in Figure 5.1 displays large residual structures and averages to close to zero; examination of the CLD spectrum and fit displayed by the QDOAS determined that no CLD was detected in the retrieval. Therefore, CLD is not displayed in subsequent parameter evaluation plots.

For the sake of conciseness, subsequent parameter evaluation plots also do not display dSCD retrievals for O_3 or NO_2 , as the purpose of this project is to evaluate the presence of IO. Parameter variations are aimed at improving sensitivity to IO, so only these dSCDs will be evaluated in detail for other parameter variations.

All retrievals suggest that IO dSCDs peak at an SZA of about 93.5°, so the QDOAS output for SZA 93.46° was examined for closer evaluation of retrieval quality. The resulting plots of the reference and spectrum, IO cross-section and total residual are shown in Fig. 5.2 for the wavelength ranges 410 - 450 nm, 435 - 465 nm, and 425 - 465 nm.

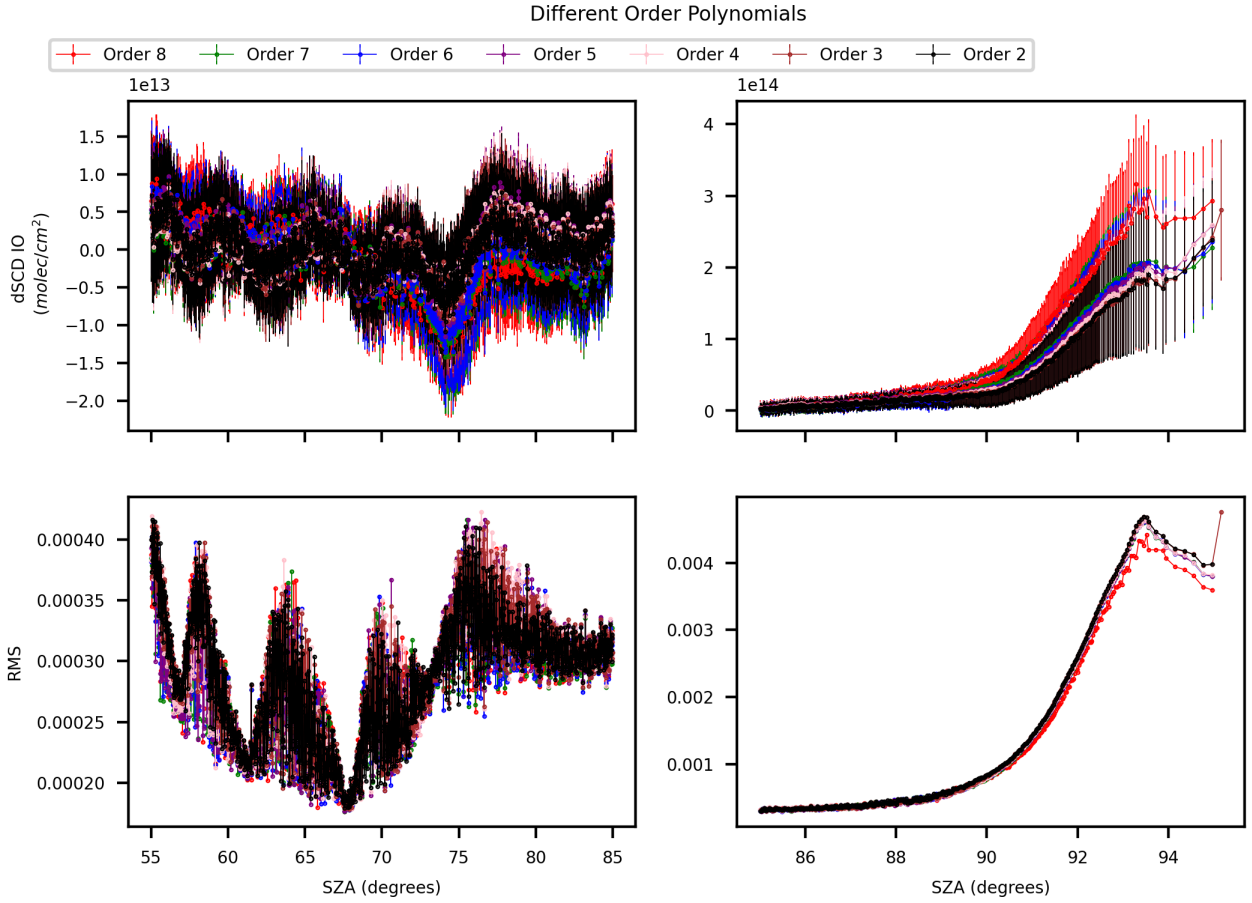


Figure 5.3: Retrieved dSCDs, CLD and RMS for various polynomial orders

5.1.2 Polynomial Order

Polynomials of orders 2-8 are compared in Fig. 5.3. A polynomial of order 3 was chosen, as this strikes a good balance between providing a low mean RMS and avoiding overfitting. Polynomial Order 6 produced the lowest mean RMS, but seems irrationally high and tends towards overfitting to absorber cross sections.

5.1.3 Reference Cross Sections

Reference cross sections of trace gases were chosen based on work by Holzbeck [5]. The absorption features of the trace gases are not independent of temperature, so various cross-sections were tested for the strong absorbers O_3 and NO_2 . These results are presented in Fig. 5.4. Ultimately, cross sections at 243K were chosen for both absorbers.

Ideally, we would fit a cross section at the effective absorption temperature of each absorber along the lightpath of each spectrum. Each spectrum can be characterized by an effective temperature T_{eff} defined as

$$T_{eff} = \frac{\sum_{k=1}^L K_k T_k n_k}{\sum_{k=1}^L K_k n_k} \quad (5.3)$$

under the assumptions of a layered atmosphere with L layers k, each with constant temperature T_k and constant species concentration n_k . In equation 5.3 K_k represents the air mass

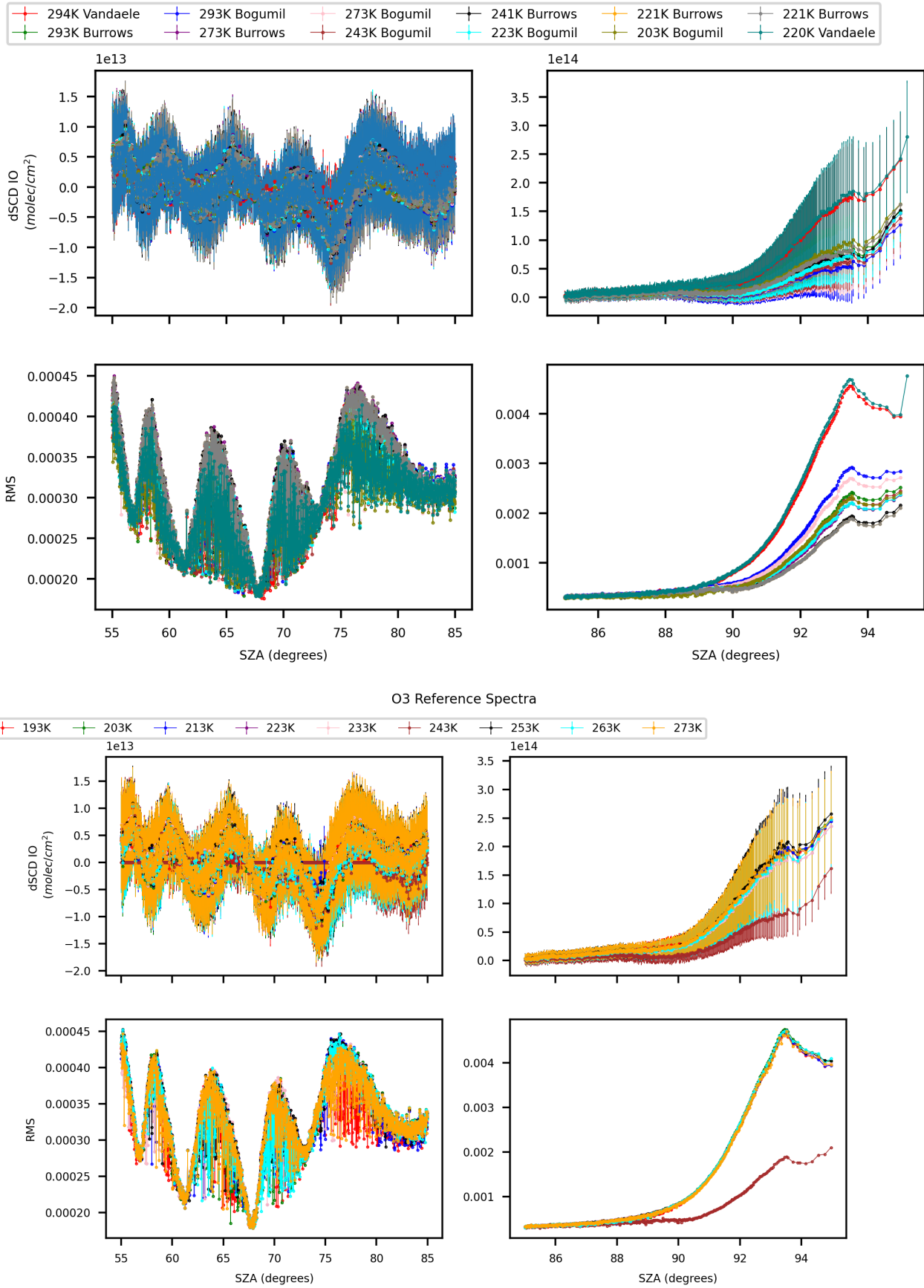


Figure 5.4: Retrieved dSCDs, CLD and RMS for various NO₂ and O₃ reference cross sections

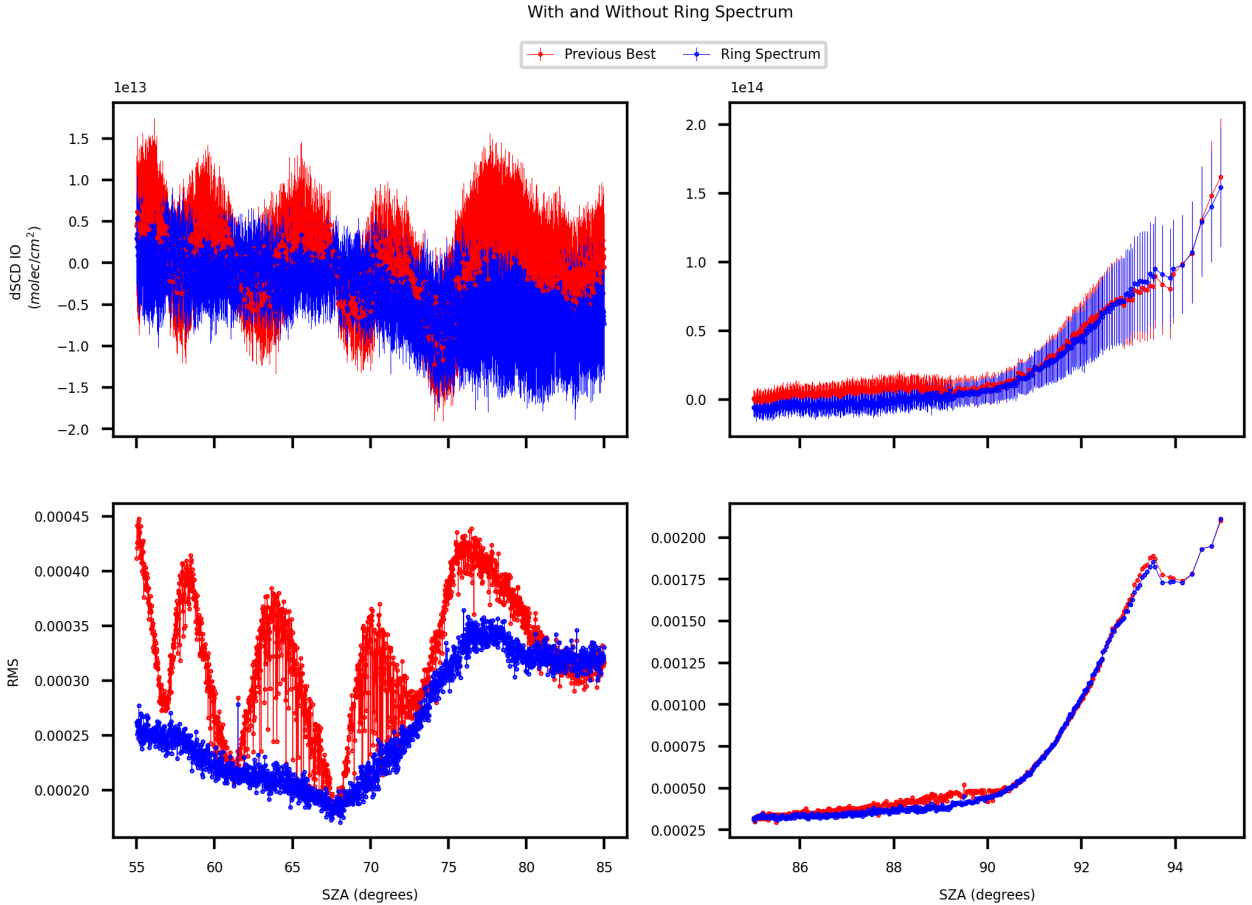


Figure 5.5: Retrieval results with and without a Ring Effect correction.

factor in layer k corresponding to the line of sight of the considered spectrum (the ratio of the slant path through layer k to the thickness of layer k). In summary, the effective absorption temperature T_{eff} is the mean absorber concentration weighted temperature along the line of sight [73].

Since we are primarily interested in the underlying structures, we can neglect fitting separate cross sections under the assumption that only the magnitude of the fitted cross section changes with temperature. If the structures themselves or the relative height of the peaks change, this could lead to systematic residual structures, making a robust detection of the target trace gas IO very difficult.

For the two strongest absorbers (NO_2 and O_3) the solar I_0 effect is also taken into account. The NO_2 correction uses an S value of 10^{20} , and the O_3 correction takes S as 10^{17} . A Ring Spectrum pseudoabsorber cross-section is also included in the fit scenario. Figure 5.5 compares retrievals run with and without the Ring Effect correction.

To minimize Fraunhofer offset, the retrieval should use a reference spectrum taken at low SZA. In this case, the spectrum taken at 22:00:05, corresponding to an SZA of 67.75° was chosen. Figure 5.6 shows the results of the retrieval scenarios using various reference spectra.

Additionally, wave-like structures in dSCD results are corrected by inclusion of pseudoabsorber cross-sections in the QDOAS evaluation. These are constructed using the wave-like structure observed in the intensity measured on each detector pixel over time. A principal component analysis (PCA) is performed to condense information within the set of residuals. The first 6 Principal Components (PCs) are taken and incorporated as absorber cross-sections

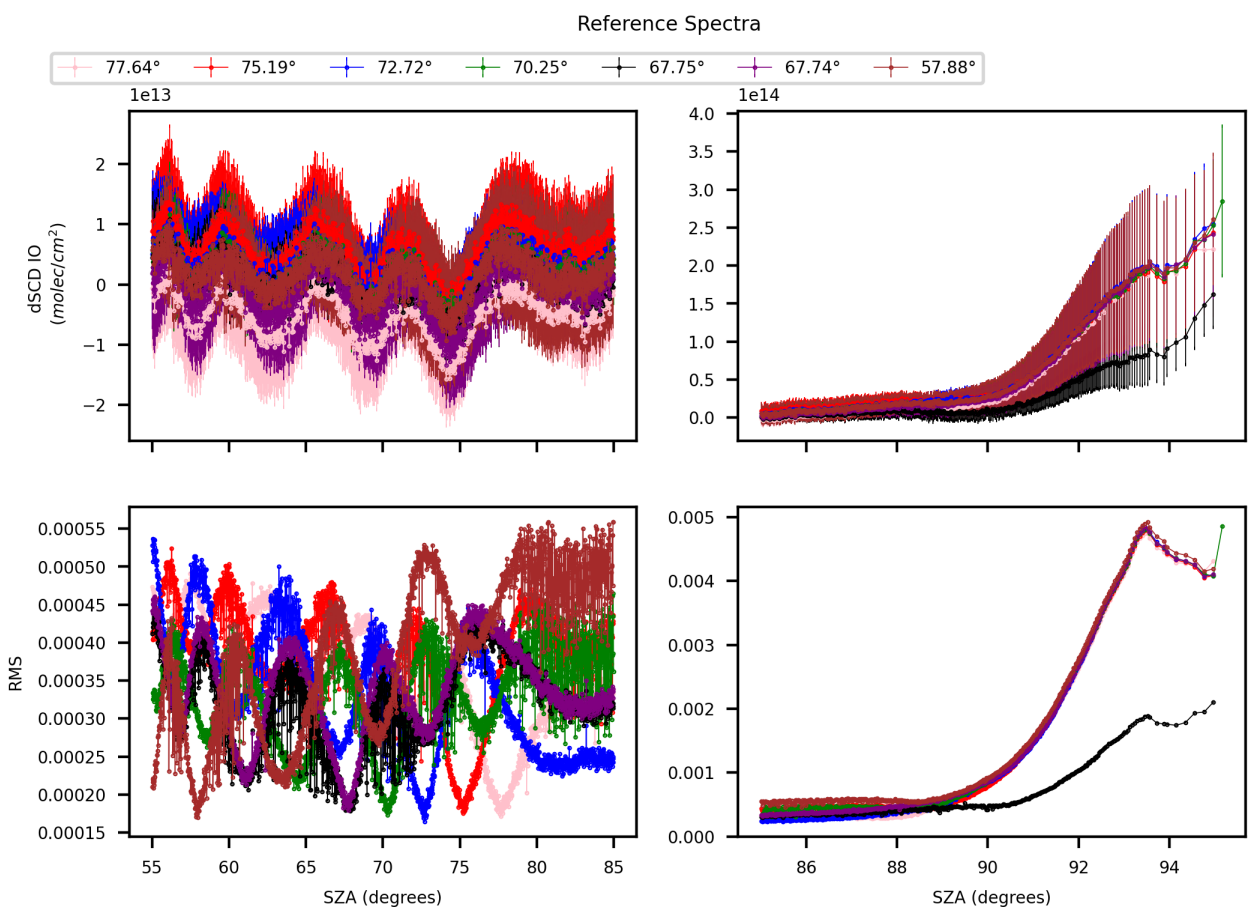


Figure 5.6: Outcomes of retrievals using various Fraunhofer reference spectra.

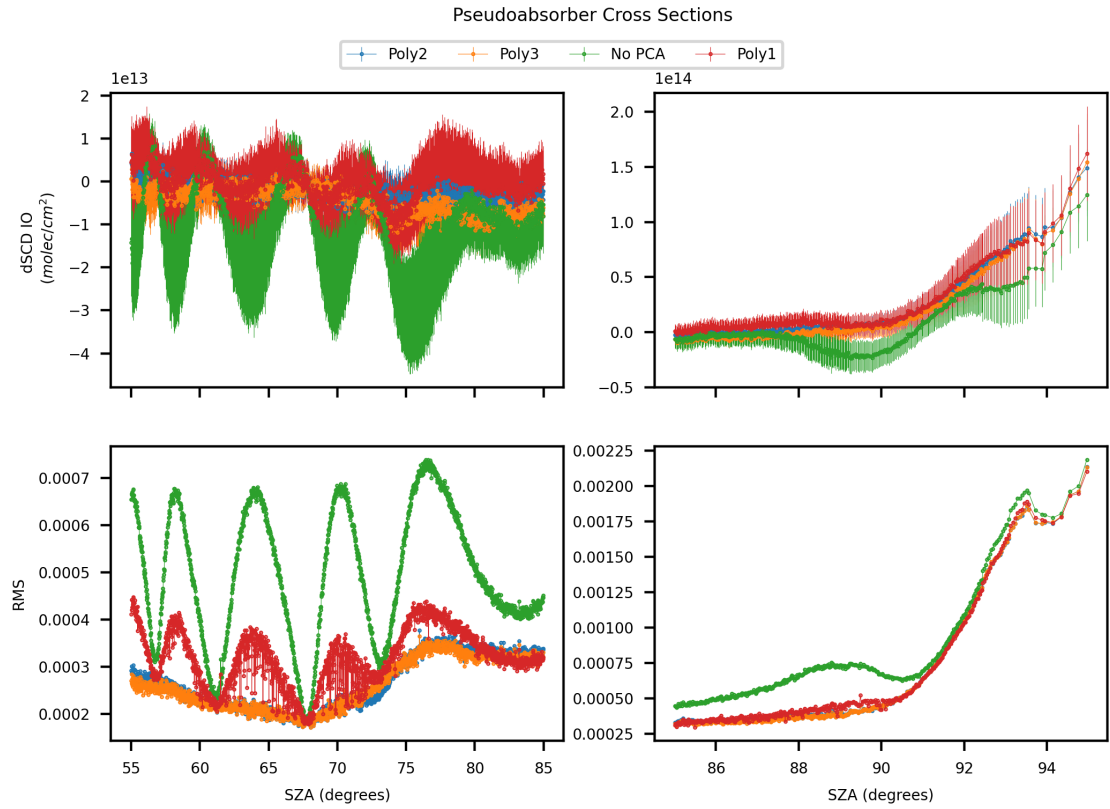


Figure 5.7: Analysis of three sets of Pseudoabsorber Cross Sections.

in the retrieval scenario [4] [5].

Fig. 5.7 illustrates three sets of PCs that were tested, as well as a fit run without any PCs for comparison. The structures of the pseudoabsorbers for Poly2 and Poly3 are shown in Fig. 5.8.

The properties of the three sets of pseudoabsorber cross sections differ as follows:

- Poly1: 100 coadded spectra, SZA $55^\circ - 75^\circ$, Reference at SZA = 72° , Polynomial Order 2
- Poly2: 200 coadded spectra, SZA $55^\circ - 76^\circ$, Reference at SZA = 76° , Polynomial Order 2
- Poly3: 200 coadded spectra, SZA $55^\circ - 76^\circ$, Reference at SZA = 76° , Polynomial Order 3

Wavelike structures are visible in the RMS and retrieved ΔSCD values for the case without PCs. These are suspected to be caused by an issue within the solar tracker optics or by an effect caused by solar radiation, as similar structures are visible in both the UV and VIS spectral ranges [5]. The spectral structures within the PCs are narrower than the instrument line shape and thus cannot be caused by an absorber in the light path.

The spectrum is allowed to shift non-linearly, with a second-order stretch fit. The six intensity wave principal components are linked and allowed to shift nonlinearly with no stretch fit. The absorber cross sections are fixed.

Stretch is set as 1st order. No offset is applied. The results for various configurations of these three parameters are shown in Fig. 5.9.

For each input parameter, the optimal value was found by evaluation of plotted inversions compared to measured spectra, as well as the size and structure of RMS residuals. Plotted

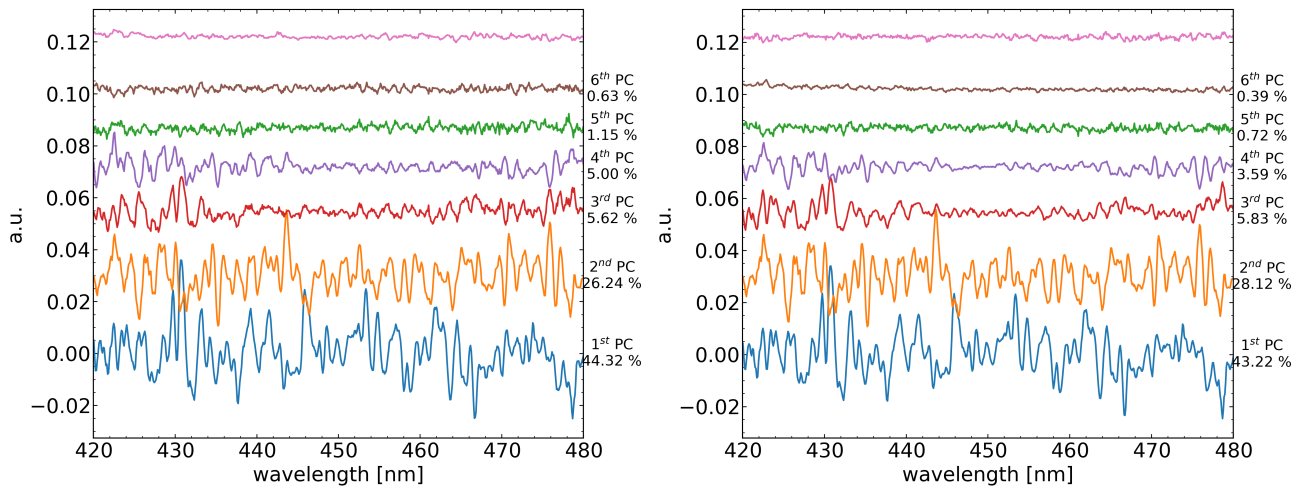


Figure 5.8: The structures of the pseudoabsorbers for Poly2 and Poly3

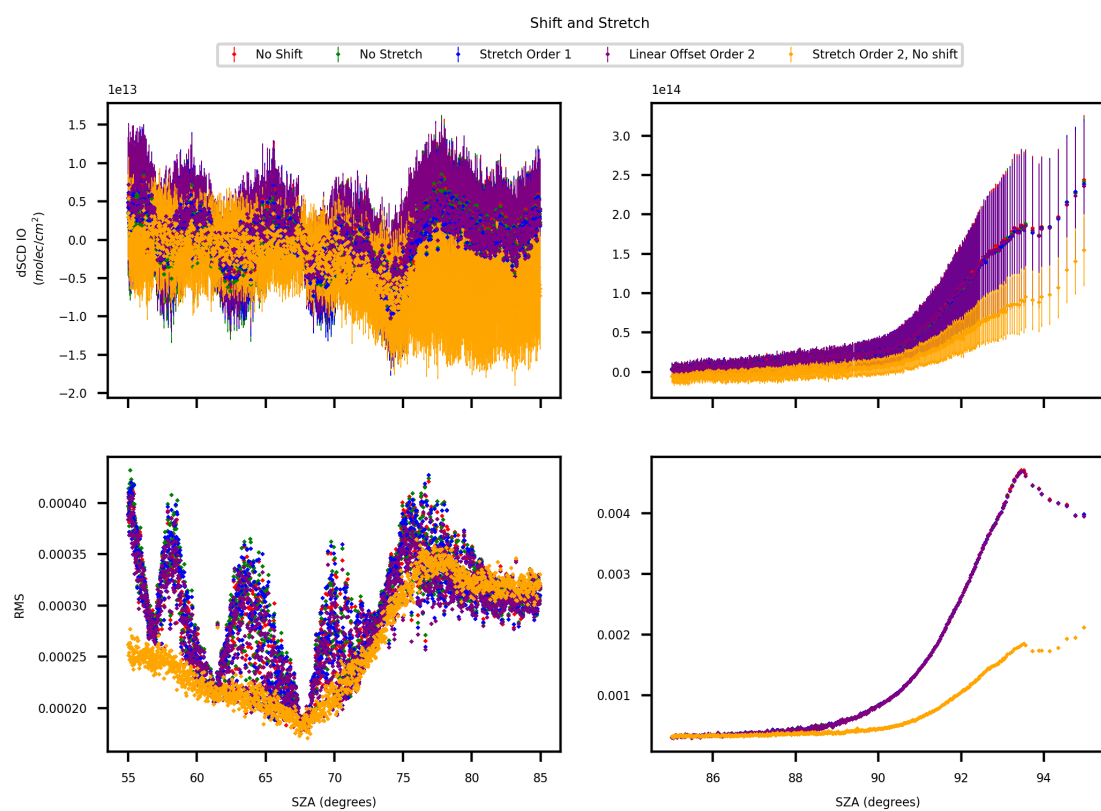


Figure 5.9: Different Configurations for shift, stretch and offset parameters.

inversions compared to measured spectra were analysed for SZAs corresponding to the stable section of the retrieval where IO dSCDs are at their maximum, i.e. SZA values just below 93.5° . Some residuals and inversions for different fit scenarios were shown in Fig. ??.

The fit scenario ultimately used for the DOAS retrieval is as follows:

- Wavelength range: 425 - 465 nm
- Reference Spectrum: SZA 67.75
- Shift: Non-linear (Spectrum), Non-linear (PCs)
- Stretch: 2nd Order (Spectrum), None (PCs)
- Polynomial Order: 3
- Offset: None
- Ozone cross-section: O₃ 243K Serdyuchenko(2014)(2013 version) [74]
- NO₂ cross-section: NO₂ 243K Bogumil(2003) [75]

The plotted inversions compared to measured spectra for $SZA = 93.46^\circ$ in this retrieval scenario are shown for IO , O_3 , NO_2 and O_4 in Fig. 5.10. Fig. 5.11 shows the plot produced by QDOAS for the Spectrum and Reference, the Residual, and the fit found to the CLD pseudoabsorber at $SZA 93.46^\circ$. The absorption structures of O_3 and NO_2 are clearly visible. No CLD effect is found. It is uncertain whether the absorption structures of IO are found, as the remaining residual structures are larger than those of the fitted IO.

The full QDOAS test results for $SZA 93.46^\circ$ are shown in Appendix B, including the fits found for the pseudoabsorber cross-sections included for the removal of residual structures, and the fit to the Ring Spectrum.

5.2 Results

The coadded spectra are analysed with the retrieval scenario described above, and the results are plotted in Fig. 5.12. Errors are given by the corresponding 2σ fit error for all results except CLD, where they are represented by a 1σ fit error.

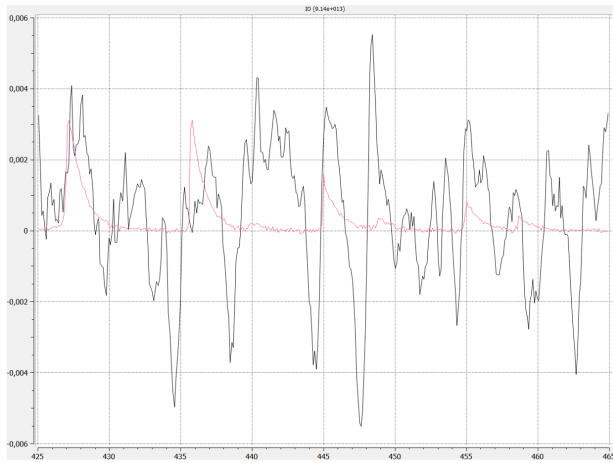
The first panel shows the retrieved ΔSCD for IO.

The second panel illustrates the retrieved ΔSCD for the CLD pseudoabsorber cross-section included in the fit.

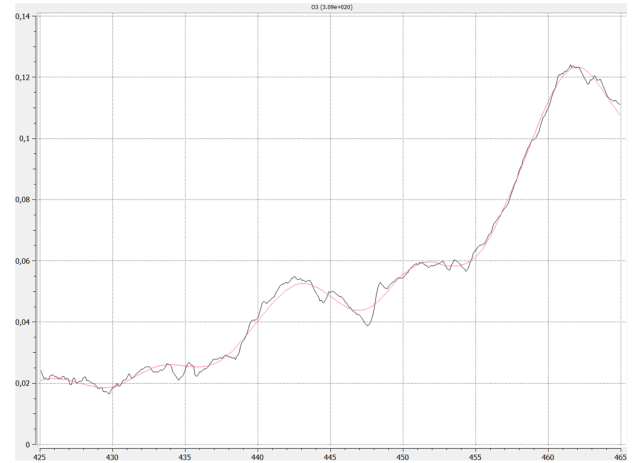
The third panel gives the root-mean-square (RMS) of the fit residuals. This does not display any significant structures beyond the expected up tick towards high SZA values.

The fourth and fifth panels show the retrieved values for O_3 and NO_2 respectively. These are the two strongest absorbers included in this scenario. As expected, their ΔSCD values increase significantly with increasing light path (i.e. higher SZA values). This trend reverses around SZA 94° for both absorbers, since for these measurements the observed tangent heights are below the maximum of the vertical profile of the species.

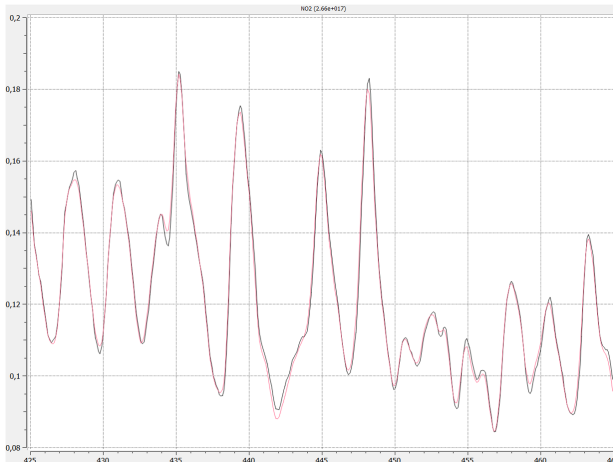
The sixth panel shows output for O_4 , which is only present in very low concentrations.



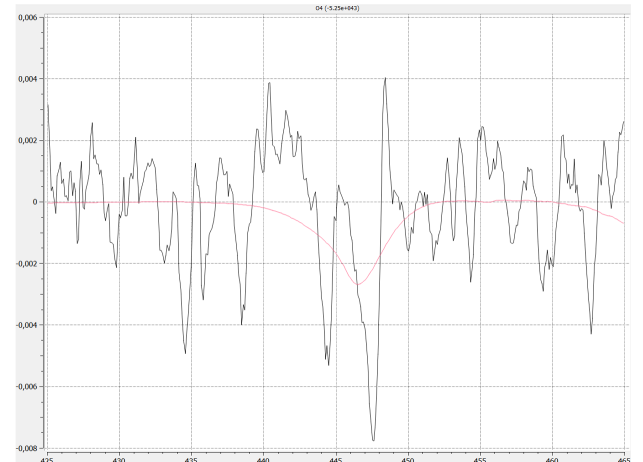
(a) IO



(b) O_3



(c) NO_2



(d) O_4

Figure 5.10: QDOAS retrieval (red) compared to absorber cross-section (black) for SZA = 93.46° from the best retrieval scenario for species IO , O_3 , NO_2 and O_4

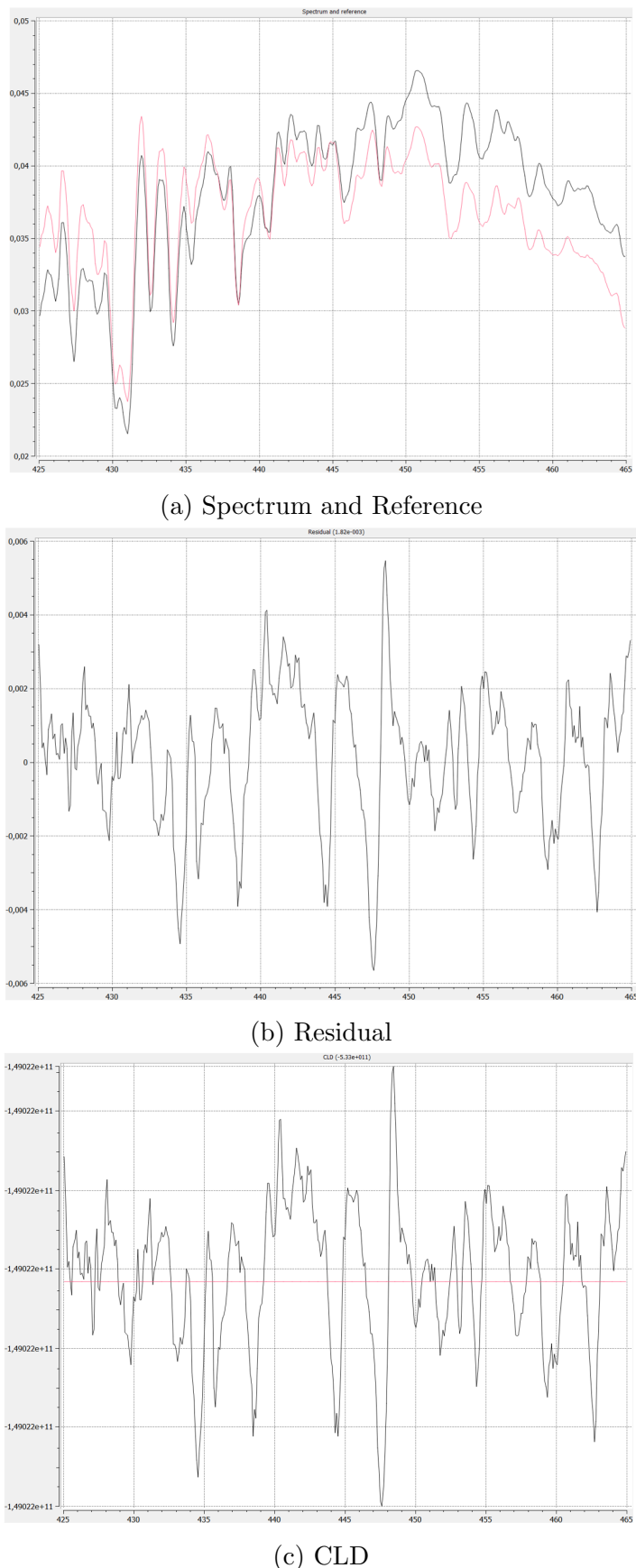


Figure 5.11: The plot produced by QDOAS for the Spectrum (red) and Reference (black), the Residual, and the fit (red) found to the CLD pseudoabsorber cross-section (black) at SZA 93.46°

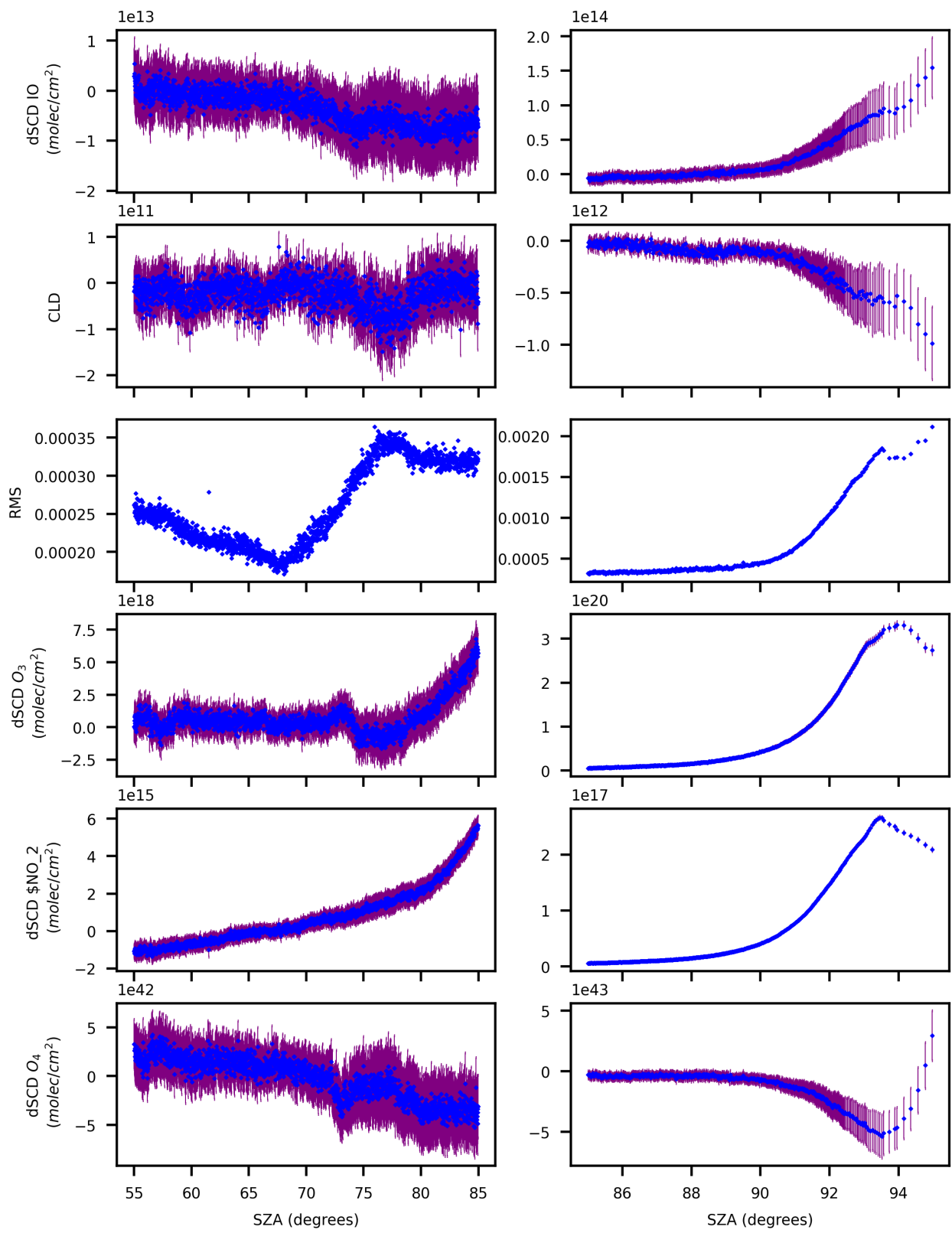


Figure 5.12: DOAS fit results for low (left) and high (right) SZA values.

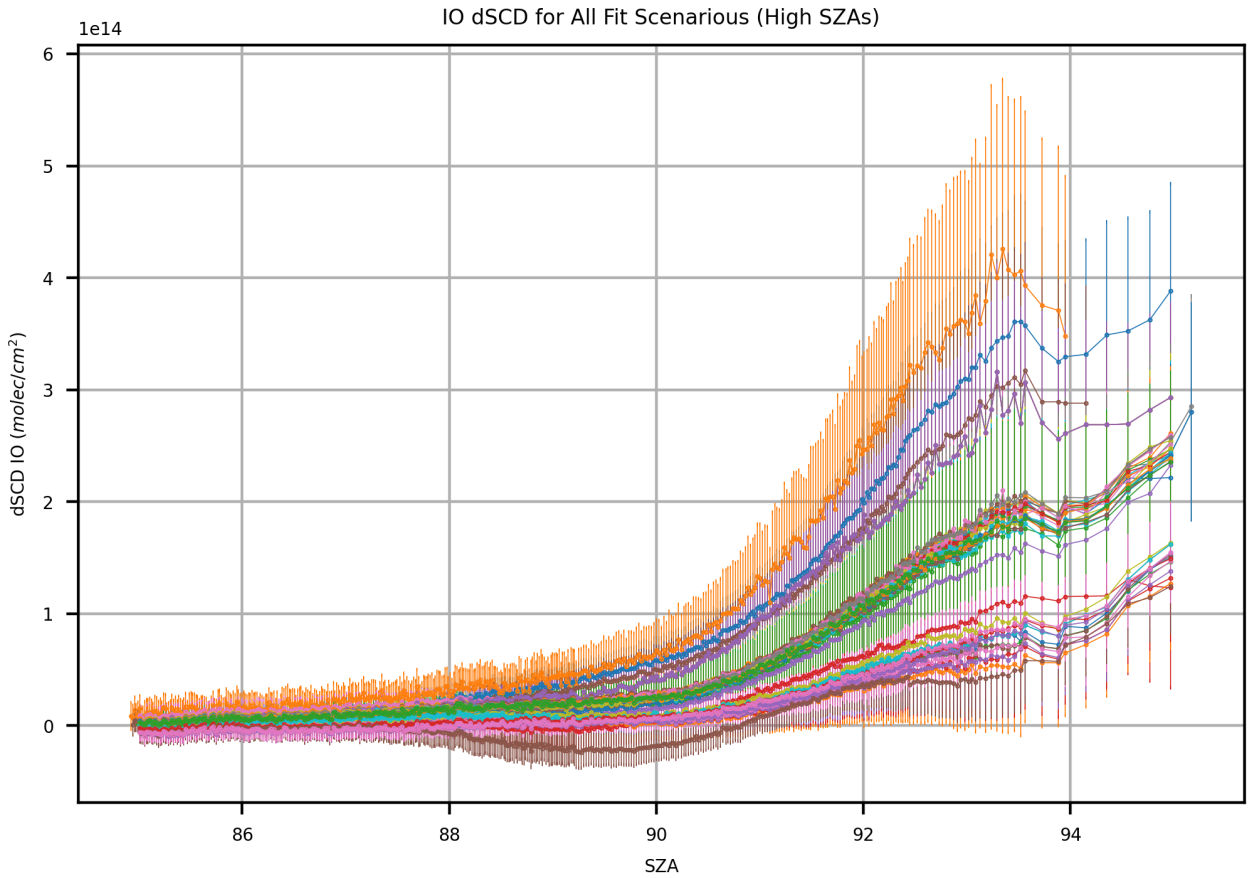


Figure 5.13: Retrieved IO SCDs for all fit scenarios. Almost all retrievals deviate from zero by more than the 2σ error shown by the error bars, which represents the detection limit under the assumption that the only error is statistical noise .

5.3 Sensitivity Study

A sensitivity study was conducted to analyse the impact of adjusting retrieval scenario parameters on retrieved SCDs. The retrieved dSCDs at high SZA for all scenarios are shown in 5.13.

For every given retrieval scenario, the detected IO values deviate from zero by more than 2σ for large SZAs, as indicated by the error bars. However, these error bars are generated by the retrieval, so their indicative value is linked to the quality of the retrieval itself. Under the assumption that the only error is statistical noise, the error bars represent the detection limit, indicating that IO surpasses this threshold. However, the presence of significant residual structures or other sources of error can render this assumption incorrect [73].

The retrieved dSCD values also group into distinct sections. Some parameters cause minimal differences to retrieved SCDs with variation, leading their retrieval scenario values to form a closely bunched set. As discussed previously, changing elements such as the literature reference cross section used for O_3 and NO_2 has a very minimal impact on the retrieval, while the most significant deviations in the retrieved dSCD profile occur when the wavelength range for the retrieval scenario is changed.

Variation of pseudoabsorber cross-sections used in the retrieval is responsible for the unphysical below-zero results produced for SZAs below 90°; this is on account of the retrieval

being skewed by the wave-like structures that occur in the absence of pseudoabsorbers.

Chapter 6

Results

6.1 Langley Plots

The mean VMR and Fraunhofer offset for O_3 , NO_2 and IO are determined using Langley's method, as described in Chapter 3.

O_3 and NO_2 are analysed together with IO despite not being the target species in this project for validation purposes. A great deal more is known about stratospheric Ozone and NO_2 profiles than about IO , so the results obtained from these species can initially be used as a sanity check on the reliability of the SCD retrieval and profile construction.

Additionally, Ozone vertical profile data are available from an Ozone sonde launched separately from the balloon a few hours after the launch of the balloon, and from the MLS (microwave limb sounding) satellite which gathered data for the Timmins region on the same date as the campaign. These external data sources are used to validate the retrieved Ozone profile, and thereby examine the reliability of the retrieval, in Chapter 7.

The Langley plots for O_3 , NO_2 and IO are shown in Fig. 6.1, with the linear regression (discussed below) included. The plot shows the relationship between the ΔSCD values and the total air mass. Air mass was calculated using the Air Mass Factor (AMF) matrix output by the DAMF program [76] and the layer densities for several layers of the atmosphere, according to the equation

$$SCD_{air} = \text{AMF} \times \text{Vertical column densities of each layer} \quad (6.1)$$

where the vertical column densities of each layer are given by layer density times layer height for each atmospheric layer considered in the program.

A linear regression fit to the plotted data is performed using the LinearRegression program from `sklearn.linear_model` [77]. This method fits a linear model with coefficients $w = (w_1, \dots, w_p)$ to minimize the residual sum of squares between the observed targets in the dataset, and the targets predicted by the linear approximation. Mathematically, it solves a problem of the form:

$$\min_w \|Xw - y\|_2^2 \quad (6.2)$$

The coefficient estimates for Ordinary Least Squares methods such as this Linear Regression module rely on the independence of the features. When features are correlated and the columns of the design matrix X have an approximately linear dependence, the design matrix becomes close to singular and as a result, the least-squares estimate becomes highly sensitive to random errors in the observed target, producing a large variance.

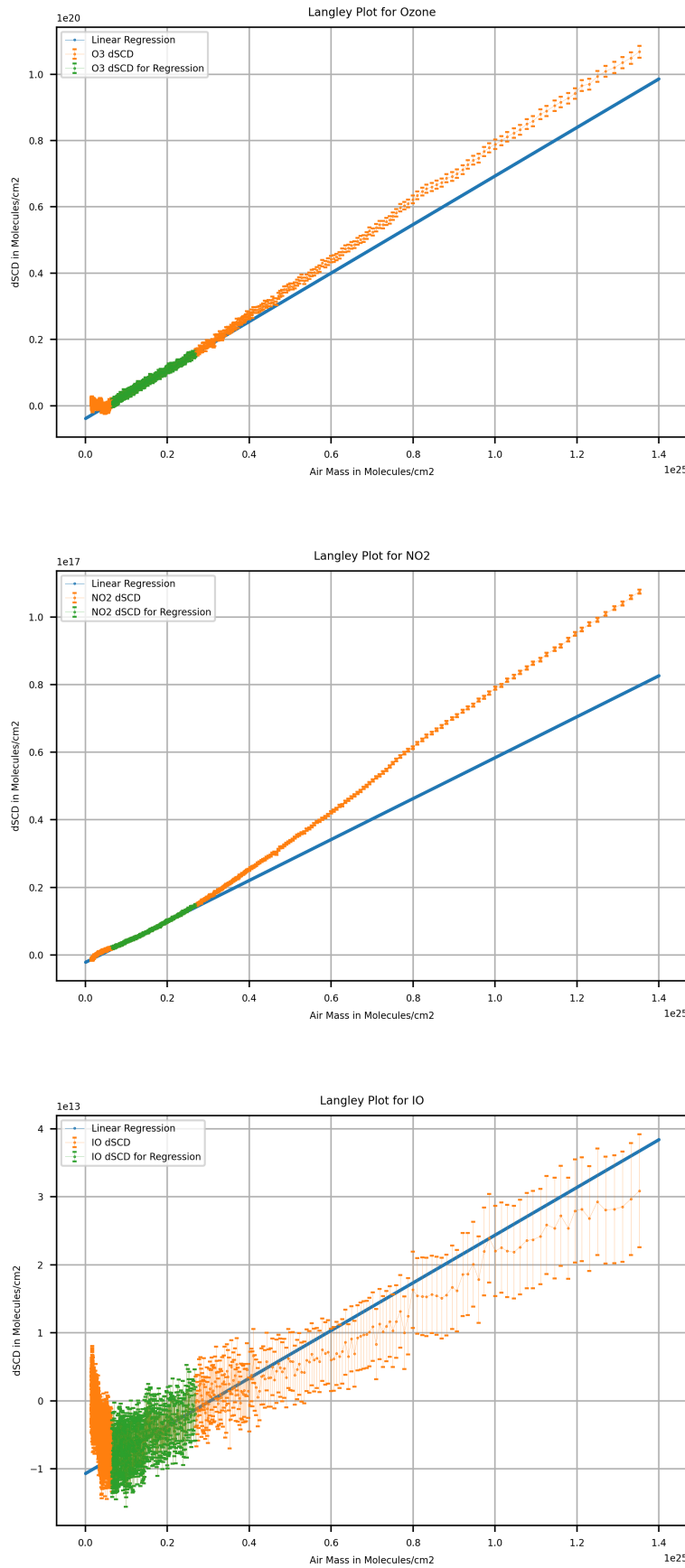


Figure 6.1: Langley Plots for O_3 , NO_2 and IO , with Linear Regression fits.

SZAs between 80 and 88 were included in the regression. This is as retrieved values for the gas dSCDS below 80° are usually below the detection limit and can therefore not be used. For SZAs above 88 the assumption of constant VMR and AMF for each layer, which is a cornerstone of Langley's Method, is no longer appropriate.

Langley's method assumes that the considered absorber's and the air's concentration in each layer do not change for all considered spectra. In other words, a large horizontal and temporal homogeneity of the gas concentration over all traversed height layers and over the time interval considered within the Langley fit is assumed. Photochemical processes significantly depend on the actinic flux, which changes with the SZA. Thus, the assumption of temporal homogeneity may result in errors. The assumption of horizontal homogeneity is justified for typical light path lengths through the atmosphere to the instrument during the float phase because the stratosphere is considered well mixed and not dominated by local phenomena above 30 km. Additionally, a constant VMR is assumed above balloon float altitude, which is generally not the case for trace gases such as IO. However, due to the quickly decreasing air density with height, only the lowest height layers above balloon float altitude contribute significantly to the VMR. Ideally, the Langley plot should not be performed up to the limit of $SZA = 90^\circ$ because the mixing ratio could already be affected by the changing irradiance conditions [4].

Furthermore, the approximation

$$AMF_j \approx \cos^{-1}(SZA) \quad (6.3)$$

which is central to the linear approximation used in a Langley plot, is only valid for low altitude segments and by extension small SZAs. At an SZA of 78° the deviation from this formula for a float spectrum in the altitude segment around 32 km is about 3% - in the altitude segment around 50 km over 10%. At an SZA of 85° these deviations increase to 4% and more than 20% for 32 km and 50 km altitude segments respectively. For an SZA of 90° , the deviation from the approximation increases towards infinity, since the air mass factor remains finite due to the curved atmosphere, but $\cos^{-1}(SZA)$ diverges [78].

However, since deviations for all considered trace gases develop similarly and remain minimal for SZAs up to 88° , values up to this point are considered in the fits performed in this project. As would be expected from this, the ΔSCD values deviate from the linear regression for the high Air Masses corresponding to the higher SZA values, as can be seen in each Langley Plot.

The parameters returned by the linear regression $Y = A + B \cdot x$ represent the following quantities:

A : The negative of the SCD of the trace gas within the reference spectrum.

B : The overhead mixing ratio of the examined species.

R^2 : The coefficient of determination of the prediction, for which the ideal value is 1 [77].

The values extracted by the regression fit for O_3 , NO_2 and IO are summarised in table 6.1.

| | O_3 | NO_2 | IO |
|------------------------|---------------|---------------|---------------|
| A ($molecules/cm^2$) | $-3.83e + 18$ | $-2.11e + 15$ | $-1.07e + 13$ |
| B (VMR) | $7.32e - 06$ | $6.06e - 09$ | $3.51e - 12$ |
| R^2 | 0.992 | 0.996 | 0.614 |

Table 6.1: values extracted by the regression fit for O_3 , NO_2 and IO.

The absolute value of A is taken for each species to obtain the Fraunhofer Offset SCD_{ref} .

To check the values provided by the Linear Regression fit and obtain a rough estimate of the error in this fit, a Least squares polynomial fit is also performed for each Langley Plot, using the `numpy.polyfit` function.

This method fits a polynomial

$$p(x) = p[0] * x * *deg + \dots + p[deg] \quad (6.4)$$

of degree deg, which was taken in this case taken as 1 to create a linear fit to the points (x, y). The function returns a vector of coefficients p that minimises the squared error. The function can also return a covariance matrix of the estimate, which was used to obtain the error for each value.

The values and errors obtained with this fitting routine are summarised in Table 6.2 .

| | O_3 | NO_2 | IO |
|-------------|---------------------------|---------------------------|---------------------------|
| SCD_{ref} | $(3.83 + / - 0.04)e + 18$ | $(2.10 + / - 0.02)e + 15$ | $(1.07 + / - 0.02)e + 13$ |
| VMR | $(7.32 + / - 0.03)e - 06$ | $(6.04 + / - 0.02)e - 09$ | $(3.51 + / - 0.1)e - 12$ |

Table 6.2: The values and errors obtained with `numpy.polyfit`.

Similarly to the significantly lower R^2 obtained from the linear regression fit for IO, the `polyfit` covariance matrix also returns an uncertainty on the VMR for IO which is an order of magnitude larger than the errors on the VMRs obtained for O_3 and NO_2 (the error is only one order of magnitude smaller than the value - for the other two species, the error is two orders of magnitude smaller).

However, the uncertainty given for the Fraunhofer offsets are similar between species - all errors are two orders of magnitude smaller than their respective values. This indicates that the gradient causes greater uncertainty in the fit than the offset.

In both cases, the uncertainty given by the QDOAS fit is used to weight the fitting program. For the linear regression module, this is input directly as the `sample_weight` parameter. For the `polyfit` routine, the error is incorporated by weighting the data points against $1/y_err$ (where y_err is the uncertainty in the QDOAS SCD retrieval, as indicated by the error bars on the Langley Plots).

The obtained Volume Mixing Ratio for IO is unphysically and unexpectedly high for both fitting methods.

6.2 Profile Retrieval

For the purposes of profile retrieval, the determined ΔSCD values must be corrected to $SCDs$ by the addition of the Fraunhofer Offset obtained from the Langley Plot. The error of the offset is propagated to the total error of the SCDs using Gaussian error propagation, [79], so the total error is given by

$$SCD_{error} = \sqrt{(\Delta SCD_{fit-error})^2 + (SCD_{ref-error})^2} \quad (6.5)$$

A vertical column density profile is retrieved from the measures slant column density values by the application of inverse methods. Inverse Methods refer to a class of algorithms applied to solve the so-called 'inverse problems,' which consist of using the results of actual observations to infer the values of the parameters characterizing the system under investigation.

Typically, predicting the result of a measurement requires a model of the system under investigation, and a physical theory linking the parameters of the model to the parameters being measured. This prediction of observations, given the values of the parameters defining the model, constitutes the "normal problem," or, in the jargon of inverse problem theory, the forward problem. The "inverse problem" works backward, extrapolating the observational results to a model of the system under investigation [80].

In this case, the inverse problem is solved with a zeroth order Tikhonov regularization to extract the species vertical profile from the SCDs and airmass factors (AMF). A routine is defined based on Singular Value Decomposition (SVD) and the Tikhonov filter factors that solves the inverse problem.

The routine takes the following input variables:

- K: forward model matrix ($m \times n$)
- y: measurement vector (m)
- yerr: measurement uncertainties (m)
- alpha: regularization parameter

For our purposes, the forward model matrix is given by the Air Mass Factor (AMF) matrix. for the retrievals described below, the AMF matrix was created with a resolution of 1km by the DAMF program.

The measurement vector and measurement uncertainties are given by the SCD values and their corresponding uncertainty. The function itself is shown in Appendix C. The function performs singular value decomposition of the forward model (AMF matrix) using the np.linalg.svd routine. Through this function, the AMF matrix is factorized as $u @ np.diag(s) @ vh = (u * s) @ vh$, where u and the Hermitian transpose of vh are 2D arrays with orthonormal columns and s is a 1D array of the AMF's singular values.

The array of singular values s, saved under the variable name 'Svec', is used to develop an array of filter factors based on the given regularization parameter alpha. These filter factors are used to perform a Moore-Penrose pseudo-inverse with 0th-order Tikhonov regularization, thereby calculating a gain matrix.

Initially, the program is run with a suitable guess for the regularization parameter, based on previous work. A best regularization parameter is determined via the L-curve method.

The routine returns:

- x: state estimate (n)
- S: a posteriori error covariance matrix ($n \times n$)
- A: averaging kernel matrix ($n \times n$)

Retrieved satellite quantities always represent a weighted average over all parts of the atmosphere that contribute to the signal observed by the satellite instrument. The averaging kernel matrix A returned by the regularization defines the relation between the retrieved quantities and the true atmospheric state [81].

The a posteriori error covariance matrix S gives an indication of the uncertainty in the retrieved profile. The square roots of the diagonals of this matrix give the error in each retrieved data point, and are included as error bars in the plotted profiles.

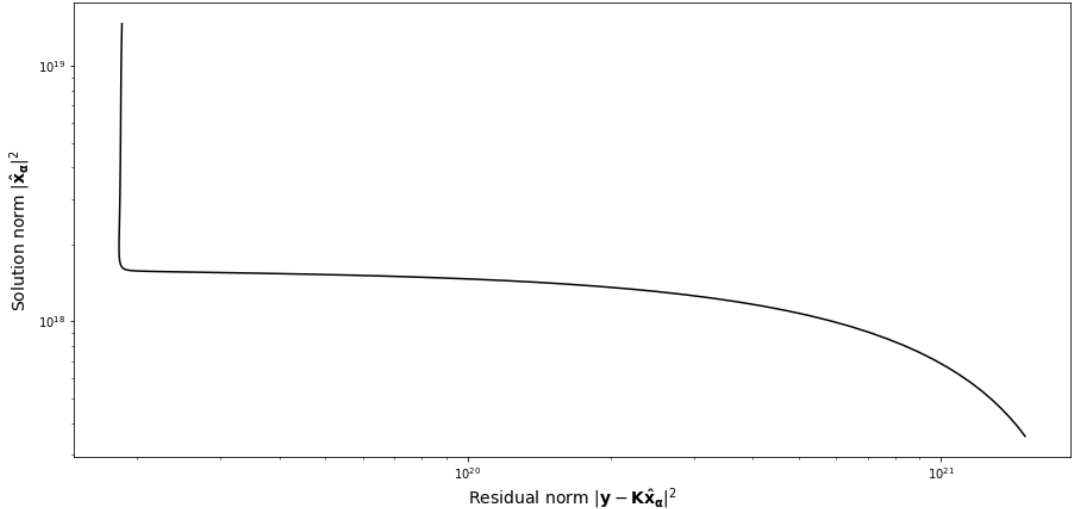


Figure 6.2: L-Curve for determination of regularization parameter alpha in O_3 profile retrieval.

The L-curve criterion is one of the best known heuristic methods for choosing the regularization parameter in various regularization methods for ill-posed problems [82]. The L-curve is a logarithmic plot of the norm of a regularized solution versus the norm of the corresponding residual. It is a convenient graphical tool to display the trade-off between the size of a regularized solution and its fit to the given data as the regularization parameter varies [83].

An example of the L-curve used to determine alpha in the case of the Ozone profile retrieval is shown in Fig. 6.2. Alpha is chosen to give the trade-off shown by the corner of the L; at this point, the size of the regularized solution is well-balanced against the fit to the given data.

6.2.1 Ozone

The retrieved O_3 profile and accompanying averaging kernels are shown in Fig. 6.3. The retrieval is only sensitive between approximately 10 km and 35 km as indicated by the plot of the averaging kernels, which are effectively zero beyond this range. Correspondingly, the plot of the profile is cropped to only display this sensitive range.

The profiles are displayed in terms of Volume Mixing Ratio for ease of comparison with other datasets and evaluation. We know that the VMR of ozone peaks at approximately 10 ppm in the stratosphere, which is consistent with this recovered profile. Plotting the profile in terms of VMR also prevents its shape from being affected by the changing properties of the atmosphere.

This retrieved ozone profile is compared with validation data sources in Chapter 7.

6.2.2 NO_2

The retrieved NO_2 profile and accompanying averaging kernels are shown in Fig. 6.4.

Similarly to the Ozone Averaging Kernels, the NO_2 averaging kernels are virtually zero outside of the 10 km to 35 km range and are peaked close to 1 within this range. However, the averaging kernels do suggest that sensitivity for the NO_2 retrieval extends slightly higher than for O_3 .

The VMR values obtained for NO_2 peak at 10 ppb at approximately 34 km altitude, with concentrations gradually increasing up to this point. Although the profile seems to indicate

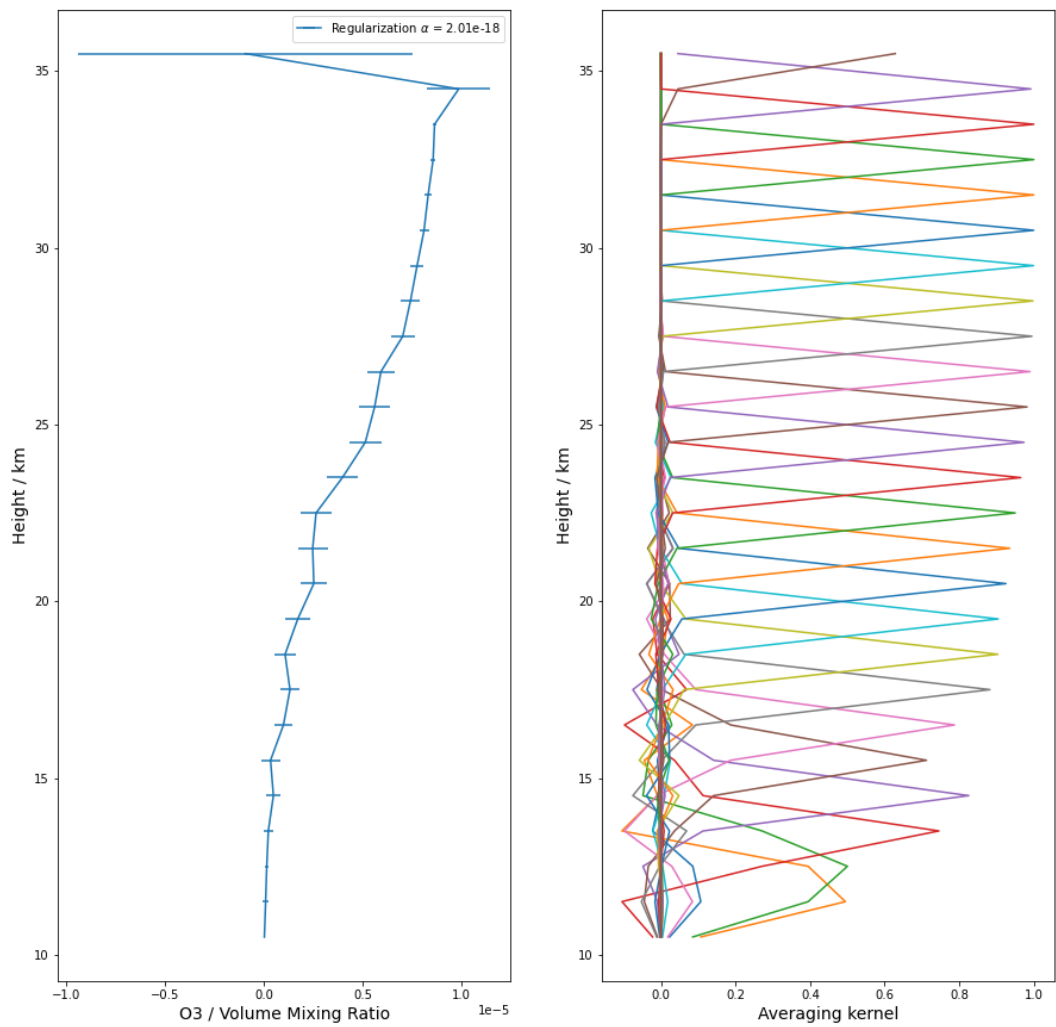


Figure 6.3: Profile and Averaging Kernels for O_3

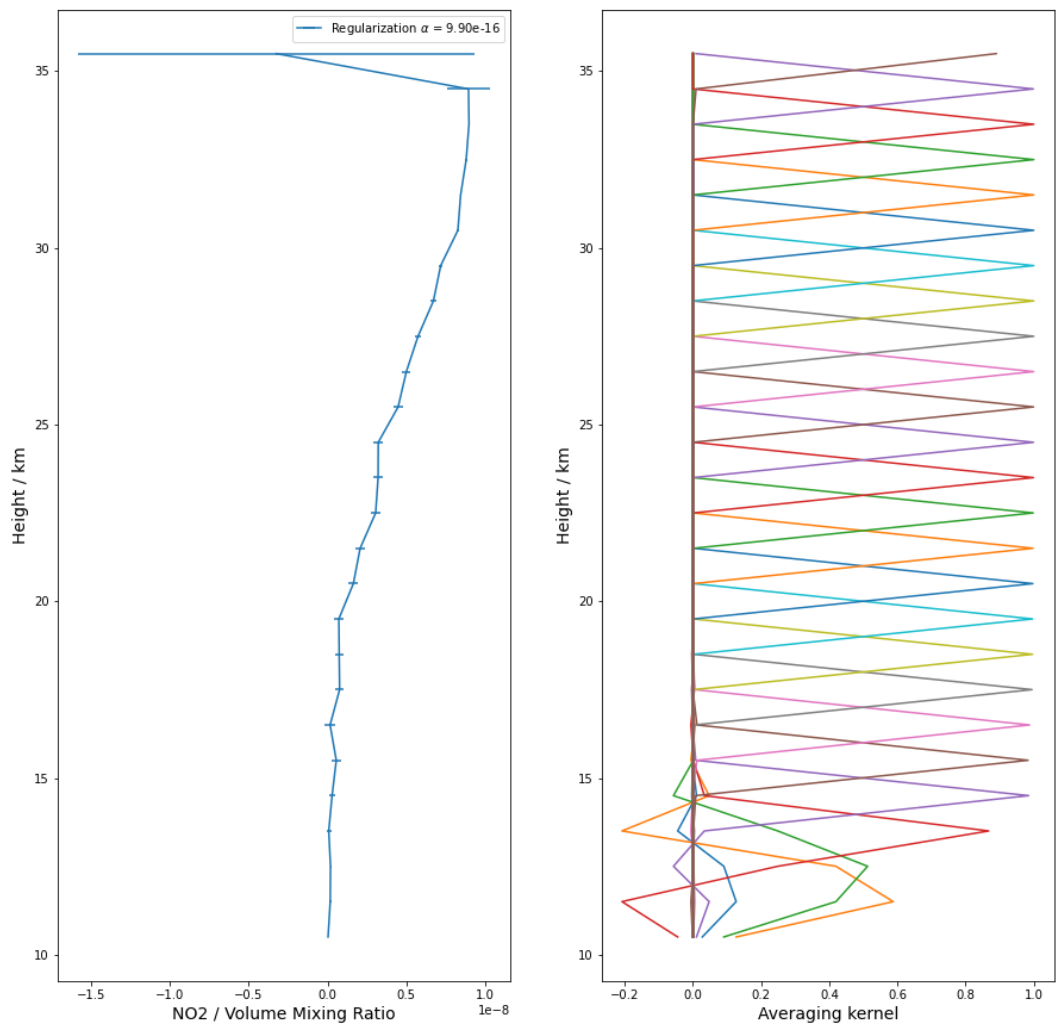


Figure 6.4: Profile and Averaging Kernels for NO_2

that concentrations start to decrease again beyond 34km, the error on the data point included beyond this height is so large that definitive statements cannot be made.

Other work has predicted that NO_2 concentrations peak between 5 and 15 ppbv in the stratosphere [84], so the concentrations retrieved here seem to be of the correct order of magnitude.

Exact validation data sources are not available for the NO_2 concentration profiles above Timmins on the date of the campaign.

6.2.3 IO

The retrieved IO profile and accompanying averaging kernels are shown in Fig. 6.5.

The vertical profile indicates that the VMR values peak at approximately 0.4 ppt. Recall that the Langley plot suggested a VMR above the atmospheric layers probed by the TotalBro instrument of 3.5ppt. This indicates a high concentration of IO above the stratosphere, and a sharp and sudden transition from low to high concentrations of IO somewhere above 35km. This contradicts all previous knowledge of stratospheric IO chemistry, and is an unphysical result. Furthermore, the errors in the retrieved vertical profile extend to zero for most data points.

From this, we can extrapolate that the DOAS method is failing to reliably detect IO, especially for lower SZAs. The Langley plot for IO also demonstrates some large residual structures and significant errors for low SZA values.

Additionally, the QDOAS fit to the IO absorber cross-section does not look particularly sensitive. Although the results are positive and therefore pass initial physicality considerations, upon closer examination, the QDOAS absorber fit closely resembles an inverted version of the fit to the O_4 absorber cross-section. In the case of O_4 , it was immediately assumed that no O_4 was detected because all returned dSCD values are negative (which is unphysical) and an unreliable QDOAS fit. Additionally, the residual structures for the QDOAS fits are larger than the fits themselves, indicating that the method is failing to detect IO.

At VMRs of parts per trillion, IO lies at the boundary of the detection sensitivity of the DOAS method. As this work indicates, it may not be possible to reliably detect stratospheric IO through DOAS.

Computational modelling of the ozone depleting effects of IO suggested that these would be most pronounced in the lower stratosphere in the tropics. An alternative method of quantifying stratospheric IO in this most significant region could be to measure Ozone profiles and their depletion, and then to analyse sections of depletion that are unaccounted for by other known and measured stratospheric chemistry. This unaccounted for depletion may give an indication of the levels of IO present in the area and their impact on the stratospheric ozone layer.

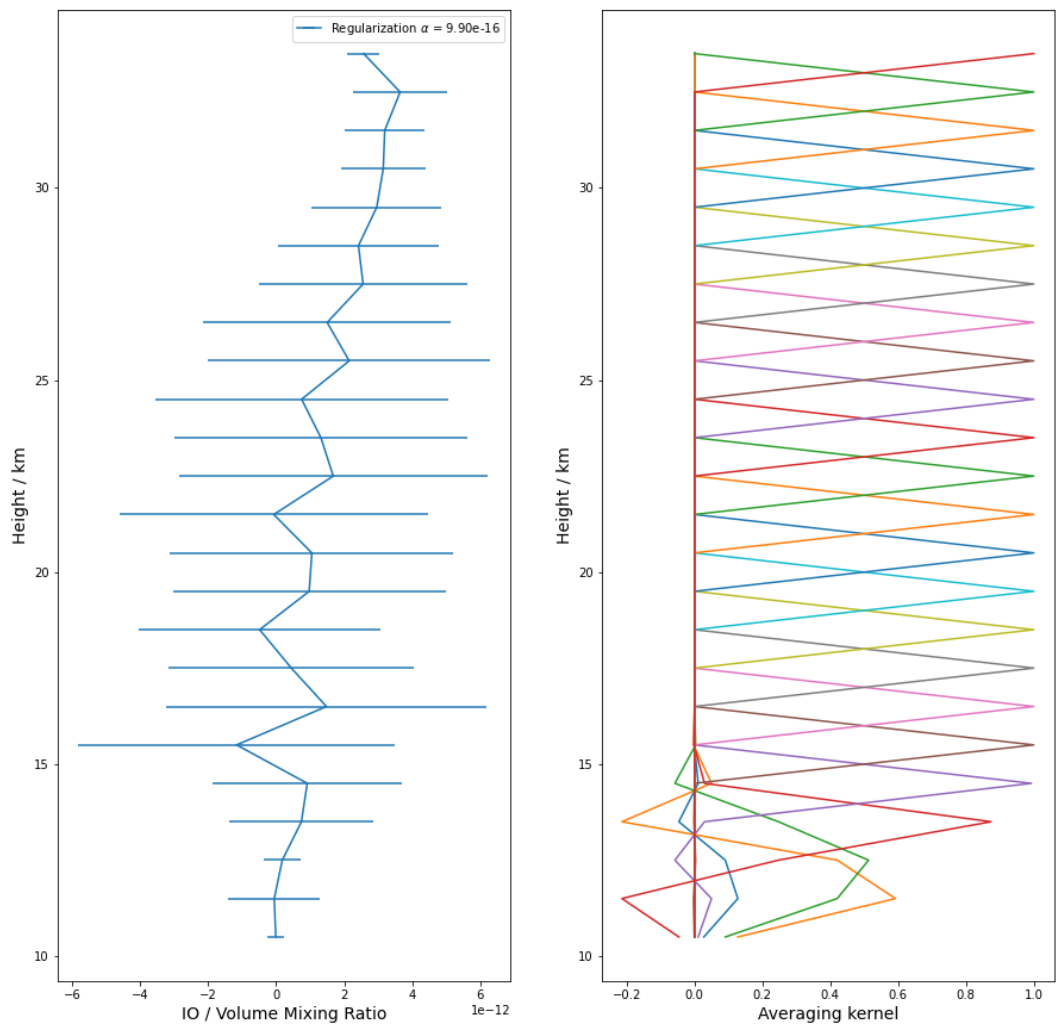


Figure 6.5: Profile and Averaging Kernels for *IO*

Chapter 7

Validation

7.1 Sonde Ozone Data

The HEMERA 3 balloon launch during which these data were collected also included the launch of an electrochemical Ozone sonde with long-range real-time communication (LoRa), named BallonBus [6], shortly after the main gondola had been deployed.

An electrochemical ozone sensor uses a porous membrane that allows ozone gas to diffuse into a cell containing an electrolyte and electrodes. When ozone comes into contact with the electrolyte, a change in electrochemical potential occurs between the electrodes causing electrons to flow. As the presence of ozone increases, the electrical signal increases proportionally [85].

Typically, an ozone sonde consists of a Teflon air pump and electrochemical ozone sensor interfaced to a meteorological radiosonde. The pump bubbles ambient air into the sensor cell, which contains 3 millilitres of 1% potassium iodide solution. The reaction of ozone and iodide generates an electrical signal proportional to the amount of ozone. The radiosonde measures air temperature, pressure, relative humidity, and transmits all the ozone and weather data back to a ground receiving station. The balloon carrying both instruments will ascend to altitudes of about 35 km before it bursts.

Total column ozone (given in Dobson Units) is calculated by integrating the partial pressure profile of ozone up to the balloon burst altitude and adding a residual amount, based on climatological ozone tables, to account for the ozone above the balloon burst altitude [86].

The volume mixing ratio profile generated with the data collected by the ozone sonde launched following the HEMERA 3 balloon is shown alongside the vertical profile retrieved from the spectra gathered by TotalBro in Fig. 7.1. The Sonde only gathered data up to 20km, but there is good agreement between the two profiles in this considered range.

7.2 MLS Data

The Earth Observing System (EOS) Microwave Limb Sounder (MLS) instrument on board NASA's Aura satellite measures naturally occurring microwave thermal emission from the limb (edge) of the Earth's atmosphere to remotely detect vertical profiles of atmospheric gases, temperature, pressure, and cloud ice [87].

It is one of four instruments aboard the satellite, which was launched on July 15th 2004. The Aura satellite is in a near-polar orbit at an altitude of 705 km. It stays fixed relative to the Sun as the Earth rotates underneath it. This configuration enables it to complete approximately 15 orbits per day, providing daily global coverage. Aura is part of NASA's A-train group of Earth

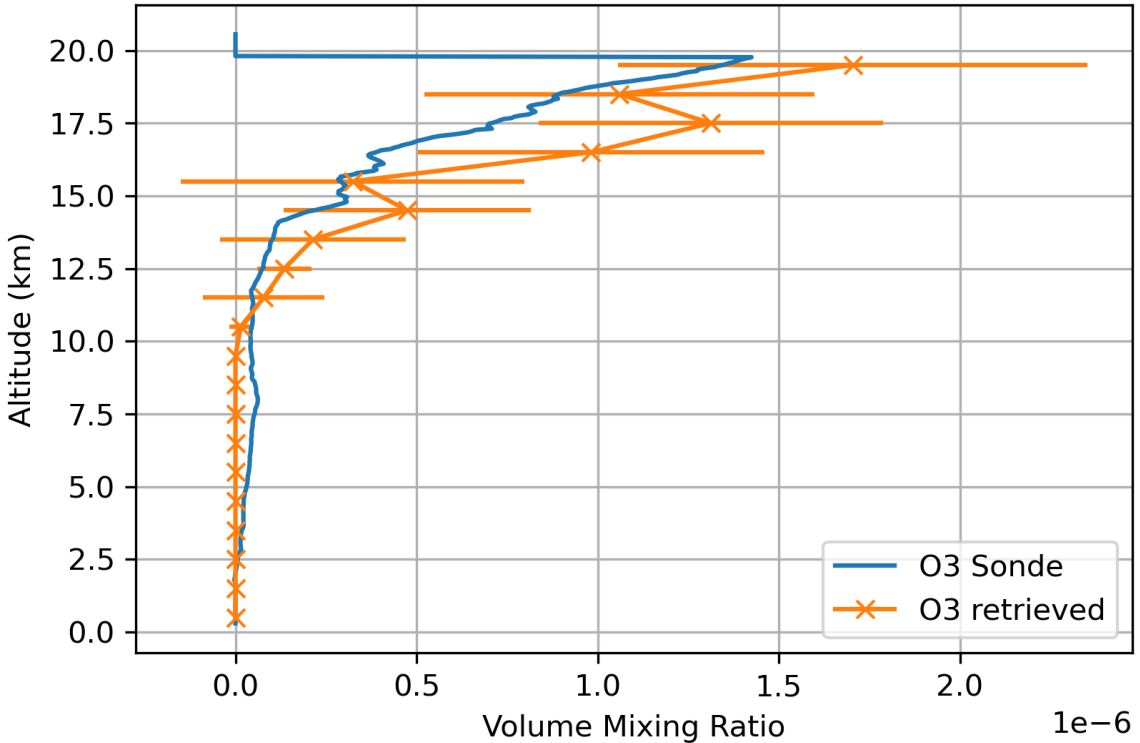


Figure 7.1: Sonde Data for O_3

observing satellites. These satellites fly in formation and make temporally close measurements [88].

MLS observes thermal microwave emission from Earth's 'limb' (the edge of the atmosphere) viewing forward along the Aura spacecraft flight direction, scanning its view from the ground to approximately 90 km roughly every 25 seconds. The instrument measures vertical profiles for the following gases:

- CO
- H_2O
- HNO_3
- N_2O
- O_3
- SO_2

Data sets for these six measured species and for the measured temperature profiles are available at [89]. The AURA satellite flew over Timmins on the same day the campaign was carried out, so the ozone profile retrieved by the TotalBro instrument can be compared with that obtained by MLS for this date and location.

The ozone profile measured by MLS is shown alongside the ozone profile retrieved in this project in Fig. 7.2. There is strong agreement between the two profiles.

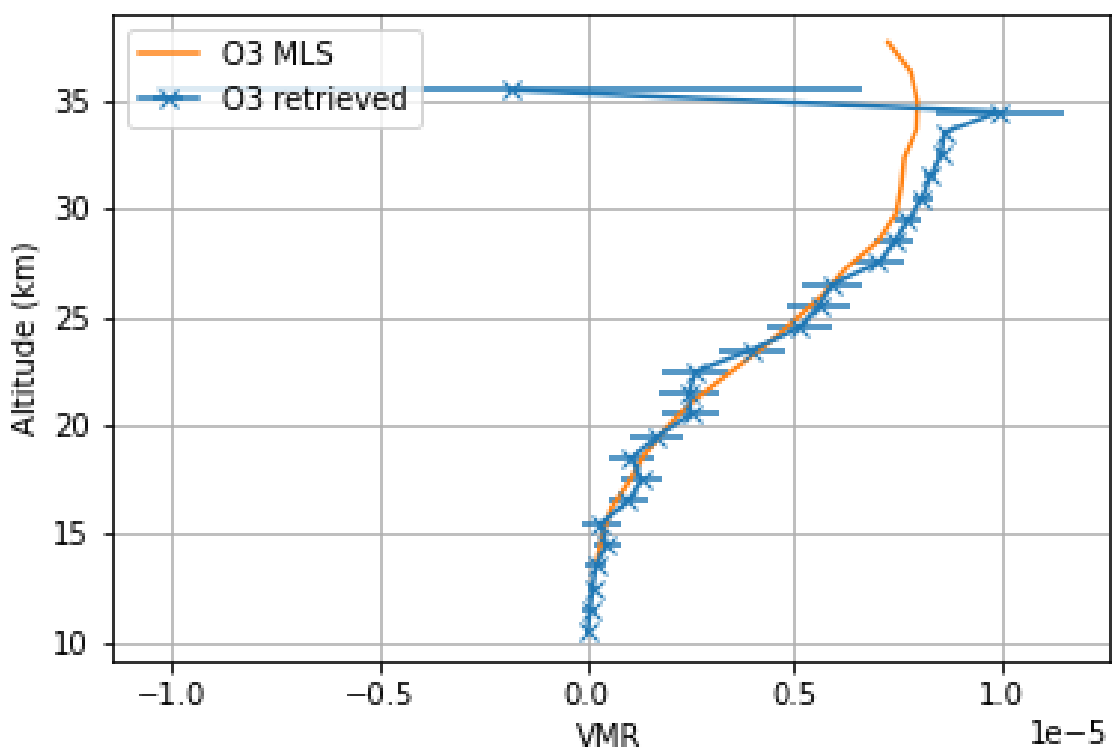


Figure 7.2: MLS Data for O_3

Chapter 8

Conclusion

Within this project, balloon-borne Differential Optical Absorption Spectroscopy (DOAS) remote sensing methods were used to examine total stratospheric IO content, and to retrieve a vertical concentration profile for IO in the lower and middle stratosphere via solar occultation and ascent measurements. The analysed spectra were obtained by the TotalBrO solar occultation DOAS instrument during the HEMERA 3 balloon launch from Timmins, Canada in August 2022 [6]. The instrument measured ultraviolet (UV) and visible (VIS) light using two grating spectrometers, and this study analysed the VIS measurements using the QDOAS program [7], for which a suitable retrieval scenario was obtained by conducting of a sensitivity study. This sensitivity study also examined whether *IO* was reliably detected.

Retrieved differential Slant Column Density (dSCD) values were analysed using Langley's Method to obtain an overhead VMR for O_3 , NO_2 and IO , and the Tikhonov inversion technique was applied to retrieve mid-stratosphere vertical concentration profiles for these species. The retrieved O_3 results compare well with data gathered by an Ozone sonde released closely after the HEMERA 3 launch, as well as data taken by a Microwave Limb Sounder (MLS) satellite which surveyed the area close to the same time.

IO is found to be on the limit of the detection sensitivity of the DOAS method, with concentrations peaking at 0.4 ppt in the retrieved vertical profile. An overhead VMR of 3.5 ppt was found; this is an unphysical result, and the two results (peak concentration and overhead VMR) are incompatible. Residual structures obtained in DOAS fits were larger than IO absorption peaks, and errors in the retrieved vertical profile extended to zero for most data points.

Research suggests that the highest concentrations of IO are present in the lower stratosphere of the tropics. Future evaluations of IO concentration and profile using DOAS could focus on this region, to increase the likelihood of robust detection of IO. Atmospheric concentrations of IO are predicted to lie in the very low ppt range, which is at the limit of the sensitivity of the DOAS method. Accordingly, applying the method to regions with higher concentrations present would enable more robust detection as the likelihood of IO being present above the detection threshold increases.

8.1 Acknowledgements

I would like to thank my supervisors, Karolin Voss and Prof. Dr. Andre Butz, for overseeing this project. I would also like to thank the Atmosphere Group at the Environmental Physics Institute of Heidelberg University for their input and feedback.

Bibliography

- [1] D. W. Fahey, "Twenty Questions and Answers About the Ozone Layer: 2006 Update," Chemical Sciences Laboratory, Tech. Rep., 2006.
- [2] T. K. Koenig, S. Baidar, P. Campuzano-Jost, C. A. Cuevas, B. Dix, R. P. Fernandez, H. Guo, S. R. Hall, D. Kinnison, B. A. Nault, K. Ullmann, J. L. Jimenez, A. Saiz-Lopez, and R. Volkamer, "Quantitative detection of iodine in the stratosphere," *Proceedings of the National Academy of Sciences*, vol. 117, no. 4, pp. 1860–1866, 1 2020.
- [3] N. Benavent, A. S. Mahajan, Q. Li, C. A. Cuevas, J. Schmale, H. Angot, T. Jokinen, L. L. J. Quéléver, A.-M. Blechschmidt, B. Zilker, A. Richter, J. A. Serna, D. Garcia-Nieto, R. P. Fernandez, H. Skov, A. Dumitrascu, P. Simões Pereira, K. Abrahamsson, S. Bucci, M. Duetsch, A. Stohl, I. Beck, T. Laurila, B. Blomquist, D. Howard, S. D. Archer, L. Bariteau, D. Helmig, J. Hueber, H.-W. Jacobi, K. Posman, L. Dada, K. R. Daellenbach, and A. Saiz-Lopez, "Substantial contribution of iodine to Arctic ozone destruction," *Nature Geoscience*, vol. 15, no. 10, pp. 770–773, 2022. [Online]. Available: <https://doi.org/10.1038/s41561-022-01018-w>
- [4] Karolin Voss, "Determination of the total stratospheric BrO mixing ratio via balloon-borne direct sun measurements with the novel spectroscopic TotalBrO instrument," Ph.D. dissertation, University of Heidelberg, Heidelberg, 2022.
- [5] Philip Holzbeck, "Results from the novel DOAS solar occultation instrument TotalBrO during its first deployment aboard a stratospheric balloon," Ph.D. dissertation, University of Heidelberg, Heidelberg, 2022.
- [6] L. Pacheco, "HEMERA 3," 6 2023. [Online]. Available: <https://stratocat.com.ar/fichas-e/2022/TMS-20220823.htm>
- [7] Royal Belgian Institute for Space Aeronomy, "QDOAS," 12 2022. [Online]. Available: <https://uv-vis.aeronomie.be/software/QDOAS/>
- [8] I. Cnossen, J. Sanz-Forcada, F. Favata, O. Witasse, T. Zegers, and N. F. Arnold, "Habitat of early life: Solar X-ray and UV radiation at Earth's surface 4–3.5 billion years ago," *Journal of Geophysical Research: Planets*, vol. 112, no. E2, 2 2007. [Online]. Available: <https://doi.org/10.1029/2006JE002784>
- [9] J. C. Van Der Leun, "The ozone layer," *Photodermatology, Photoimmunology & Photomedicine*, vol. 20, no. 4, pp. 159–162, 8 2004. [Online]. Available: <https://doi.org/10.1111/j.1600-0781.2004.00091.x>
- [10] R. L. McKenzie, P. J. Aucamp, A. F. Bais, L. O. Björn, M. Ilyas, and S. Madronich, "Ozone depletion and climate change: impacts on UV radiation," *Photochemical & Photobiological Sciences*, vol. 10, no. 2, pp. 182–198, 2 2011.

- [11] “ozone-depleting substance.” [Online]. Available: <https://www.eea.europa.eu/help/glossary/eea-glossary/ozone-depleting-substance>
- [12] H. Vargas-Uricoechea, A. Bonelo-Perdomo, and C. Sierra-Torres, “Iodine and the Thyroid,” 3 2016, pp. 27–48.
- [13] K. Christe and S. Schneider, “Iodine,” 2 2023.
- [14] A. Saiz-Lopez, J. M. C. Plane, A. R. Baker, L. J. Carpenter, R. von Glasow, J. C. Gómez Martín, G. McFiggans, and R. W. Saunders, “Atmospheric Chemistry of Iodine,” *Chemical Reviews*, vol. 112, no. 3, pp. 1773–1804, 3 2012. [Online]. Available: <https://doi.org/10.1021/cr200029u>
- [15] Chris McLinden, “Differential Optical Absorption Spectroscopy,” 7 1999. [Online]. Available: [https://www.ess.uci.edu/~cmclinden/link/xx/node67.html#:~:text=Differential%20Optical%20Absorption%20Spectroscopy%20\(DOAS,et%20al.%2C%201973\)](https://www.ess.uci.edu/~cmclinden/link/xx/node67.html#:~:text=Differential%20Optical%20Absorption%20Spectroscopy%20(DOAS,et%20al.%2C%201973)).
- [16] “Dynamics and Transport,” in *Aeronomy of the Middle Atmosphere: Chemistry and Physics of the Stratosphere and Mesosphere*, G. P. Brasseur and S. Solomon, Eds. Dordrecht: Springer Netherlands, 2005, pp. 51–149. [Online]. Available: https://doi.org/10.1007/1-4020-3824-0_3
- [17] J. Marshall and A. Plumb, *Circulation of the Atmosphere and Ocean: an introductory text*. Massachusetts: Massachusetts Institute of Technology, 1 2007.
- [18] S. K. Dhaka and V. Kumar, “Chapter 1 - Composition and thermal structure of the earth’s atmosphere,” in *Atmospheric Remote Sensing*, A. Kumar Singh and S. Tiwari, Eds. Elsevier, 2023, pp. 1–18. [Online]. Available: <https://www.sciencedirect.com/science/article/pii/B9780323992626000237>
- [19] I. V. Muralikrishna and V. Manickam, “Chapter Fourteen - Air Pollution Control Technologies,” in *Environmental Management*, I. V. Muralikrishna and V. Manickam, Eds. Butterworth-Heinemann, 2017, pp. 337–397. [Online]. Available: <https://www.sciencedirect.com/science/article/pii/B9780128119891000142>
- [20] D. E. Reichle, “Chapter 10 - The global carbon cycle and the biosphere,” in *The Global Carbon Cycle and Climate Change (Second Edition)*, D. E. Reichle, Ed. Elsevier, 2023, pp. 235–283. [Online]. Available: <https://www.sciencedirect.com/science/article/pii/B9780443187759000140>
- [21] R J Murgatroyd, “The physics and dynamics of the stratosphere and mesosphere,” *Reports on Progress in Physics*, vol. 33, no. 3, p. 817, 1970. [Online]. Available: <https://dx.doi.org/10.1088/0034-4885/33/3/301>
- [22] “The Stratosphere,” 2011. [Online]. Available: <https://scied.ucar.edu/learning-zone/atmosphere/stratosphere>
- [23] “Chapter 11 Stratospheric Dynamics,” in *International Geophysics*, J. R. Holton, Ed. Academic Press, 1979, vol. 23, pp. 295–322. [Online]. Available: <https://www.sciencedirect.com/science/article/pii/S0074614208605276>

- [24] J. Liang, “1 - Chemical composition of the atmosphere of the Earth,” in *Chemical Modeling for Air Resources*, J. Liang, Ed. Boston: Academic Press, 2013, pp. 3–20. [Online]. Available: <https://www.sciencedirect.com/science/article/pii/B978012408135200001X>
- [25] R. H. Varney and M. C. Kelley, “MESOSPHERE — Polar Summer Mesopause,” in *Encyclopedia of Atmospheric Sciences (Second Edition)*, G. R. North, J. Pyle, and F. Zhang, Eds. Oxford: Academic Press, 2015, pp. 436–443. [Online]. Available: <https://www.sciencedirect.com/science/article/pii/B9780123822253002218>
- [26] S. Bekki and J. Savarino, “Ozone and Stratospheric Chemistry,” in *Encyclopedia of Geochemistry: A Comprehensive Reference Source on the Chemistry of the Earth*, W. M. White, Ed. Cham: Springer International Publishing, 2016, pp. 1–12. [Online]. Available: https://doi.org/10.1007/978-3-319-39193-9_207-1
- [27] J. J. Zhang, Y. Wei, and Z. Fang, “Ozone Pollution: A Major Health Hazard Worldwide,” *Frontiers in Immunology*, vol. 10, 10 2019.
- [28] B. Bolaji, “CFC Refrigerants and Stratospheric Ozone: Past, Present and Future,” 10 2005, pp. 231–237.
- [29] E. Sher, “Chapter 2 - Environmental Aspects of Air Pollution,” in *Handbook of Air Pollution From Internal Combustion Engines*, E. Sher, Ed. San Diego: Academic Press, 1998, pp. 27–41. [Online]. Available: <https://www.sciencedirect.com/science/article/pii/B9780126398557500417>
- [30] C. Fabry and H. Buisson, “L’absorption de l’ultra-violet par l’ozone et la limite du spectre solaire,” *J. Phys. Theor. Appl.*, pp. 196–206, 1913.
- [31] S. Solomon, “Stratospheric ozone depletion: A review of concepts and history,” *Reviews of Geophysics*, vol. 37, no. 3, pp. 275–316, 8 1999. [Online]. Available: <https://doi.org/10.1029/1999RG900008>
- [32] S. Chapman, “XXXV. On ozone and atomic oxygen in the upper atmosphere,” *The London, Edinburgh, and Dublin Philosophical Magazine and Journal of Science*, vol. 10, no. 64, pp. 369–383, 9 1930. [Online]. Available: <https://doi.org/10.1080/14786443009461588>
- [33] T. Leisner, “Physics of the Atmosphere,” Heidelberg, 1 2023.
- [34] F. S. Rowland, “Stratospheric ozone depletion,” *Philosophical Transactions of the Royal Society B: Biological Sciences*, vol. 361, no. 1469, pp. 769–790, 5 2006.
- [35] U. Langematz, “Stratospheric ozone: down and up through the anthropocene,” *ChemTexts*, vol. 5, no. 2, p. 8, 2019. [Online]. Available: <https://doi.org/10.1007/s40828-019-0082-7>
- [36] R. R. Garcia, “Causes of ozone depletion,” *Physics World*, vol. 7, no. 4, pp. 49–55, 4 1994.
- [37] D. J. Lary, “Catalytic destruction of stratospheric ozone,” *Journal of Geophysical Research: Atmospheres*, vol. 102, no. D17, pp. 21 515–21 526, 9 1997.
- [38] “Scientific Assessment of Ozone Depletion,” World Meteorological Organization (WMO), Geneva, Tech. Rep., 2018.

- [39] F. d. Gruijl and J. Leun, “Environment and health: 3. Ozone depletion and ultraviolet radiation,” *Canadian Medical Association Journal*, vol. 163, no. 7, p. 851, 10 2000. [Online]. Available: <http://www.cmaj.ca/content/163/7/851.abstract>
- [40] “Montreal Protocol on Substances that Deplete the Ozone Layer,” Montreal, 9 1987.
- [41] “2. f Amendment to the Montreal Protocol on Substances that Deplete the Ozone Layer,” Kigali, 1 2019.
- [42] “U.S. Ratification of the Kigali Amendment,” 9 2022. [Online]. Available: <https://www.state.gov/u-s-ratification-of-the-kigali-amendment/#:~:text=The%20Kigali%20Amendment%20calls%20for,which%20are%20potent%20greenhouse%20gases>.
- [43] “Ozone depleting substances,” 10 2021. [Online]. Available: <https://www.dcceew.gov.au/environment/protection/ozone/ozone-science/ozone-depleting-substances>
- [44] “On the role of iodine in ozone depletion,” *Journal of Geophysical Research: Atmospheres*, vol. 99, no. D10, pp. 20 491–20 499, 10 1994. [Online]. Available: <https://doi.org/10.1029/94JD02028>
- [45] S. Solomon, J. B. Burkholder, A. R. Ravishankara, and R. R. Garcia, “Ozone depletion and global warming potentials of CF₃I,” *Journal of Geophysical Research*, vol. 99, no. D10, p. 20929, 1994.
- [46] H. Bösch, C. Camy-Peyret, M. P. Chipperfield, R. Fitzenberger, H. Harder, U. Platt, and K. Pfeilsticker, “Upper limits of stratospheric IO and OIO inferred from center-to-limb-darkening-corrected balloon-borne solar occultation visible spectra: Implications for total gaseous iodine and stratospheric ozone,” *Journal of Geophysical Research: Atmospheres*, vol. 108, no. D15, 8 2003. [Online]. Available: <https://doi.org/10.1029/2002JD003078>
- [47] P. O. Wennberg, J. W. Brault, T. F. Hanisco, R. J. Salawitch, and G. H. Mount, “The atmospheric column abundance of IO: Implications for stratospheric ozone,” *Journal of Geophysical Research: Atmospheres*, vol. 102, no. D7, pp. 8887–8898, 4 1997. [Online]. Available: <https://doi.org/10.1029/96JD03712>
- [48] A. Butz, H. Bösch, C. Camy-Peyret, M. P. Chipperfield, M. Dorf, S. Kreycy, L. Kritten, C. Prados-Román, J. Schwärzle, and K. Pfeilsticker, “Constraints on inorganic gaseous iodine in the tropical upper troposphere and stratosphere inferred from balloon-borne solar occultation observations,” *Atmos. Chem. Phys.*, vol. 9, no. 18, pp. 7229–7242, 9 2009. [Online]. Available: <https://acp.copernicus.org/articles/9/7229/2009/><https://acp.copernicus.org/articles/9/7229/2009/acp-9-7229-2009.pdf>
- [49] C. A. Cuevas, R. P. Fernandez, D. E. Kinnison, Q. Li, J.-F. Lamarque, T. Trabelsi, J. S. Francisco, S. Solomon, and A. Saiz-Lopez, “The influence of iodine on the Antarctic stratospheric ozone hole,” *Proceedings of the National Academy of Sciences*, vol. 119, no. 7, 2 2022.
- [50] A. Saiz-Lopez, S. Baidar, C. A. Cuevas, T. K. Koenig, R. P. Fernandez, B. Dix, D. E. Kinnison, J.-F. Lamarque, X. Rodriguez-Lloveras, T. L. Campos, and R. Volkamer, “Injection of iodine to the stratosphere,” *Geophysical Research Letters*, vol. 42, no. 16, pp. 6852–6859, 8 2015. [Online]. Available: <https://doi.org/10.1002/2015GL064796>

- [51] A. Karagodin-Doyennel, E. Rozanov, T. Sukhodolov, T. Egorova, A. Saiz-Lopez, C. A. Cuevas, R. P. Fernandez, T. Sherwen, R. Volkamer, T. K. Koenig, T. Giroud, and T. Peter, “Iodine chemistry in the chemistry–climate model SOCOL-AERv2-I,” *Geosci. Model Dev.*, vol. 14, no. 10, pp. 6623–6645, 10 2021. [Online]. Available: <https://gmd.copernicus.org/articles/14/6623/2021/><https://gmd.copernicus.org/articles/14/6623/2021/gmd-14-6623-2021.pdf>
- [52] G. Hönniger, C. von Friedeburg, and U. Platt, “Multi axis differential optical absorption spectroscopy (MAX-DOAS),” *Atmos. Chem. Phys.*, vol. 4, no. 1, pp. 231–254, 2 2004. [Online]. Available: <https://acp.copernicus.org/articles/4/231/2004/><https://acp.copernicus.org/articles/4/231/2004/acp-4-231-2004.pdf>
- [53] U. Platt, “Differential Optical Absorption Spectroscopy (DOAS),” in *Air Monitoring by Spectroscopic Techniques*, M. Sigrist, Ed. New York: Wiley, 1994, vol. 127, ch. 2, pp. 27–84.
- [54] J. Kaiser, “Atmospheric Parameter Retrieval from UV-vis-NIR Limb Scattering Measurements,” http://elib.suub.uni-bremen.de/diss/docs/E-Diss195_kaiser.pdf, 1 2001.
- [55] R. Penndorf, “Tables of the refractive index for standard air and the Rayleigh scattering coefficient for the spectral region between 0.2 and 20.0 μ and their application to atmospheric optics,” *Josa*, vol. 47, no. 2, pp. 176–182, 1957.
- [56] D. J. Lockwood, “Rayleigh and Mie Scattering,” in *Encyclopedia of Color Science and Technology*, M. R. Luo, Ed. New York, NY: Springer New York, 2016, pp. 1097–1107. [Online]. Available: https://doi.org/10.1007/978-1-4419-8071-7_218
- [57] C. Junge, *Air Chemistry and Radioactivity*. New York: Academic Press, 1963, vol. 4.
- [58] R. L. Kurucz, “High Resolution Irradiance Spectrum from 300 to 1000 nm,” 5 2006.
- [59] S. P. Langley, “On a Possible Variation of the Solar Radiation and its Probable Effect on Terrestrial Temperatures,” *The Astrophysical Journal*, vol. 19, p. 305, 6 1904.
- [60] U. Platt and J. Stutz, *Differential Optical Absorption Spectroscopy (DOAS)—Principles and Applications*, 1 2008, vol. 15.
- [61] J. F. GRAINGER and J. RING, “Anomalous Fraunhofer Line Profiles,” *Nature*, vol. 193, no. 4817, p. 762, 1962. [Online]. Available: <https://doi.org/10.1038/193762a0>
- [62] A. T. Young, “Rayleigh scattering,” *Applied Optics*, vol. 20, no. 4, pp. 533–535, 1981. [Online]. Available: <https://opg.optica.org/ao/abstract.cfm?URI=ao-20-4-533>
- [63] S. C. Solomon, A. L. Schmeltekopf, and R. W. Sanders, “On the interpretation of zenith sky absorption measurements,” *Journal of Geophysical Research*, vol. 92, pp. 8311–8319, 1987.
- [64] T. Wagner, K. Chance, U. Frieß, M. Gil, F. Goutail, G. Hönniger, P. Johnston, K. Karlsen-Tørnkvist, I. Kostadinov, H. Leser, A. Petritoli, A. Richter, M. Van Roozendael, and U. Platt, “Correction of the Ring effect and I0-effect for DOAS observations of scattered sunlight,” 1 2001.

- [65] S. R. Aliwell, M. Van Roozendael, P. V. Johnston, A. Richter, T. Wagner, D. W. Arlander, J. P. Burrows, D. J. Fish, R. L. Jones, K. K. Tørnkvist, J.-C. Lambert, K. Pfeilsticker, and I. Pundt, “Analysis for BrO in zenith-sky spectra: An intercomparison exercise for analysis improvement,” *Journal of Geophysical Research: Atmospheres*, vol. 107, no. D14, pp. 10–1, 7 2002. [Online]. Available: <https://doi.org/10.1029/2001JD000329>
- [66] S. Kazarski, “Neuere Ballonmessungen zur Photochemie und der Menge an stratosphärischem Brom,” Ph.D. dissertation, University of Heidelberg, Heidelberg, 1 2020.
- [67] “QE Pro Scientific-grade Spectrometer Installation and Operation Manual,” 2014. [Online]. Available: <https://www.oceaninsight.com/globalassets/catalog-blocks-and-images/manuals--instruction-ocean-optics/spectrometer/qepro.pdf>
- [68] A. D. Stiff-Roberts, “6.11 - Quantum-Dot Infrared Photodetectors,” in *Comprehensive Semiconductor Science and Technology*, P. Bhattacharya, R. Fornari, and H. Kamimura, Eds. Amsterdam: Elsevier, 2011, pp. 452–485. [Online]. Available: <https://www.sciencedirect.com/science/article/pii/B9780444531537000365>
- [69] “What is Spectrometer Dark Current?” 5 2017. [Online]. Available: <https://www.stellarnet.us/what-is-spectrometer-dark-current/>
- [70] W. Kaye, “Pen-Ray Rare Gas Lamp Spectra,” Tech. Rep., 1997.
- [71] T. Danckaert, C. Fayt, M. Van Roozendael, I. De Smedt, V. Letocart, A. Merlaud, and G. Pinardi, “QDOAS Software user manual,” 9 2017.
- [72] Hartmut Bösch, “Studies of the Stratospheric Nitrogen and Iodine Chemistry by Balloon-Borne DOAS Measurements and Model Calculations,” Ph.D. dissertation, University of Heidelberg, Heidelberg, 2 2002.
- [73] André Butz, “Case Studies of Stratospheric Nitrogen, Chlorine and Iodine Photochemistry Based on Balloon Borne UV/visible and IR Absorption Spectroscopy,” Ph.D. dissertation, University of Heidelberg, Heidelberg, 7 2006.
- [74] A. Serdyuchenko, V. Gorshelev, M. Weber, W. Chehade, and J. P. Burrows, “High spectral resolution ozone absorption cross-sections – Part 2: Temperature dependence,” *Atmos. Meas. Tech.*, vol. 7, no. 2, pp. 625–636, 2 2014. [Online]. Available: <https://amt.copernicus.org/articles/7/625/2014/>
- [75] K. Bogumil, J. Orphal, T. Homann, S. Voigt, P. Spietz, O. C. Fleischmann, A. Vogel, M. Hartmann, H. Kromminga, H. Bovensmann, J. Frerick, and J. P. Burrows, “Measurements of molecular absorption spectra with the SCIAMACHY pre-flight model: instrument characterization and reference data for atmospheric remote-sensing in the 230–2380 nm region,” *Journal of Photochemistry and Photobiology A: Chemistry*, vol. 157, no. 2, pp. 167–184, 2003. [Online]. Available: <https://www.sciencedirect.com/science/article/pii/S1010603003000625>
- [76] M. Schulte, “DAMF v2.0 - Direct Light Air Mass Factors,” Heidelberg, 1996.
- [77] F. Pedregosa, G. Varoquaux, and A. Gramfort, “Scikit-learn: Machine Learning in Python,” *Journal of Machine Learning Research*, vol. 12, pp. 2825–2830, 2011.

- [78] A. Lindner, “Ballongestützte Messungen der extraterrestrischen spektralen solaren Irradianz ,” Ph.D. dissertation, Ruprecht-Karls-Universität Heidelberg, Heidelberg, 2005.
- [79] V. Lindberg, “Uncertainties and Error Propagation Part I of a manual on Uncertainties, Graphing, and the Vernier Caliper,” 7 2000. [Online]. Available: <https://www.geol.lsu.edu/jlorenzo/geophysics/uncertainties/Uncertaintiespart2.html>
- [80] A. Tarantola, “Inverse Problem.” [Online]. Available: <https://mathworld.wolfram.com/InverseProblem.html>
- [81] H. J. Eskes and K. F. Boersma, “Averaging kernels for DOAS total-column satellite retrievals,” *Atmos. Chem. Phys.*, vol. 3, no. 5, pp. 1285–1291, 9 2003. [Online]. Available: <https://acp.copernicus.org/articles/3/1285/2003/><https://acp.copernicus.org/articles/3/1285/2003/acp-3-1285-2003.pdf>
- [82] S. Kindermann and K. Raik, “A simplified L-curve method as error estimator,” *ETNA - Electronic Transactions on Numerical Analysis*, vol. 53, pp. 217–238, 1 2020.
- [83] P. C. Hansen, “The L-Curve and Its Use in the Numerical Treatment of Inverse Problems,” in *Computational Inverse Problems in Electrocardiology*, 1 2001, vol. 4, pp. 119–142.
- [84] S. Liu, “Inversion Models for the Retrieval of Total and Tropospheric NO₂ Columns,” *Atmosphere*, vol. 10, p. 607, 10 2019.
- [85] “Ozone Sensor Technology Comparison,” 5 2022. [Online]. Available: <https://ozonesolutions.com/blog/hmos-vs-electrochemical-vs-uv/>
- [86] “ESRL/GML Ozonesondes.” [Online]. Available: <https://gml.noaa.gov/ozwv/ozsondes/>
- [87] “Aura MLS.” [Online]. Available: <https://mls.jpl.nasa.gov/eos-aura-mls>
- [88] “Aura.” [Online]. Available: <https://aura.gsfc.nasa.gov/index.html>
- [89] “Microwave Limb Sounder (MLS),” 3 2023. [Online]. Available: <https://www.earthdata.nasa.gov/learn/find-data/near-real-time/mls>

Appendix A

Coadded Spectra per Data Point

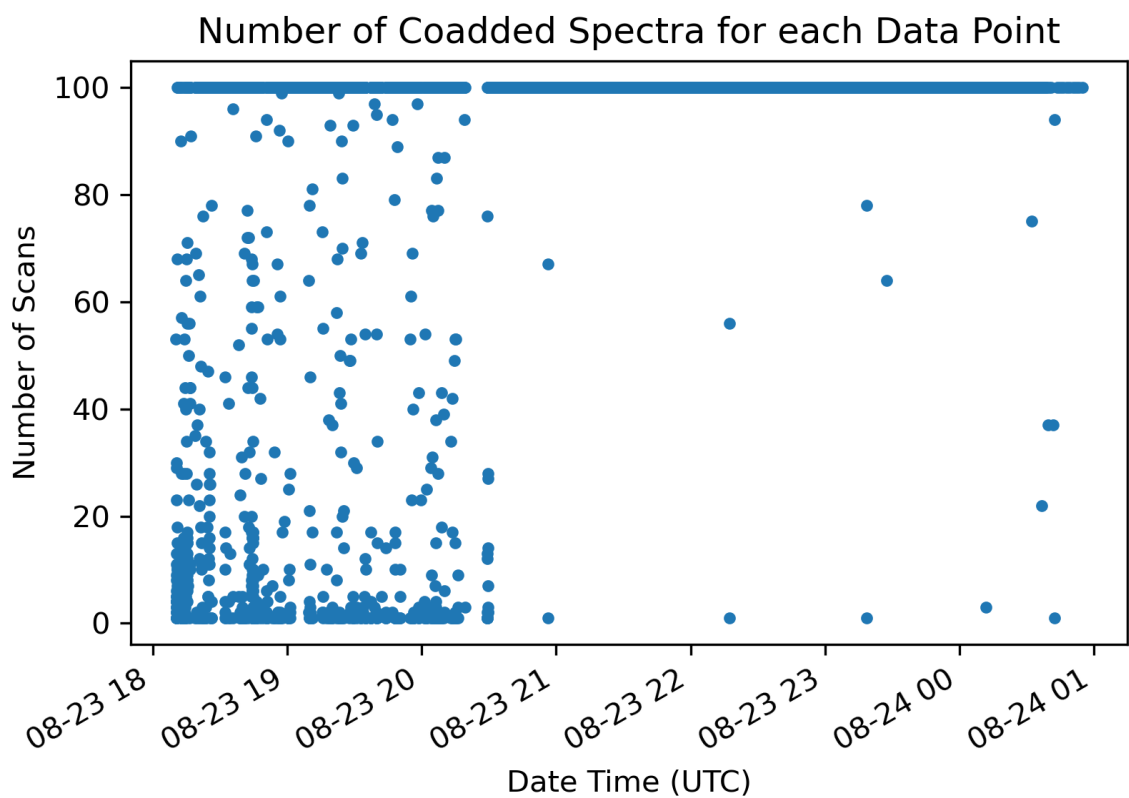


Figure A.1: Number of scans coadded to produce each data point. Data points consisting of fewer than 30 scans were disregarded in subsequent analysis on account of their higher signal-to-noise ratio. This mainly affected data gathered at the beginning of the balloon launch.

Appendix B

Full QDOAS Output SZA 93.46°

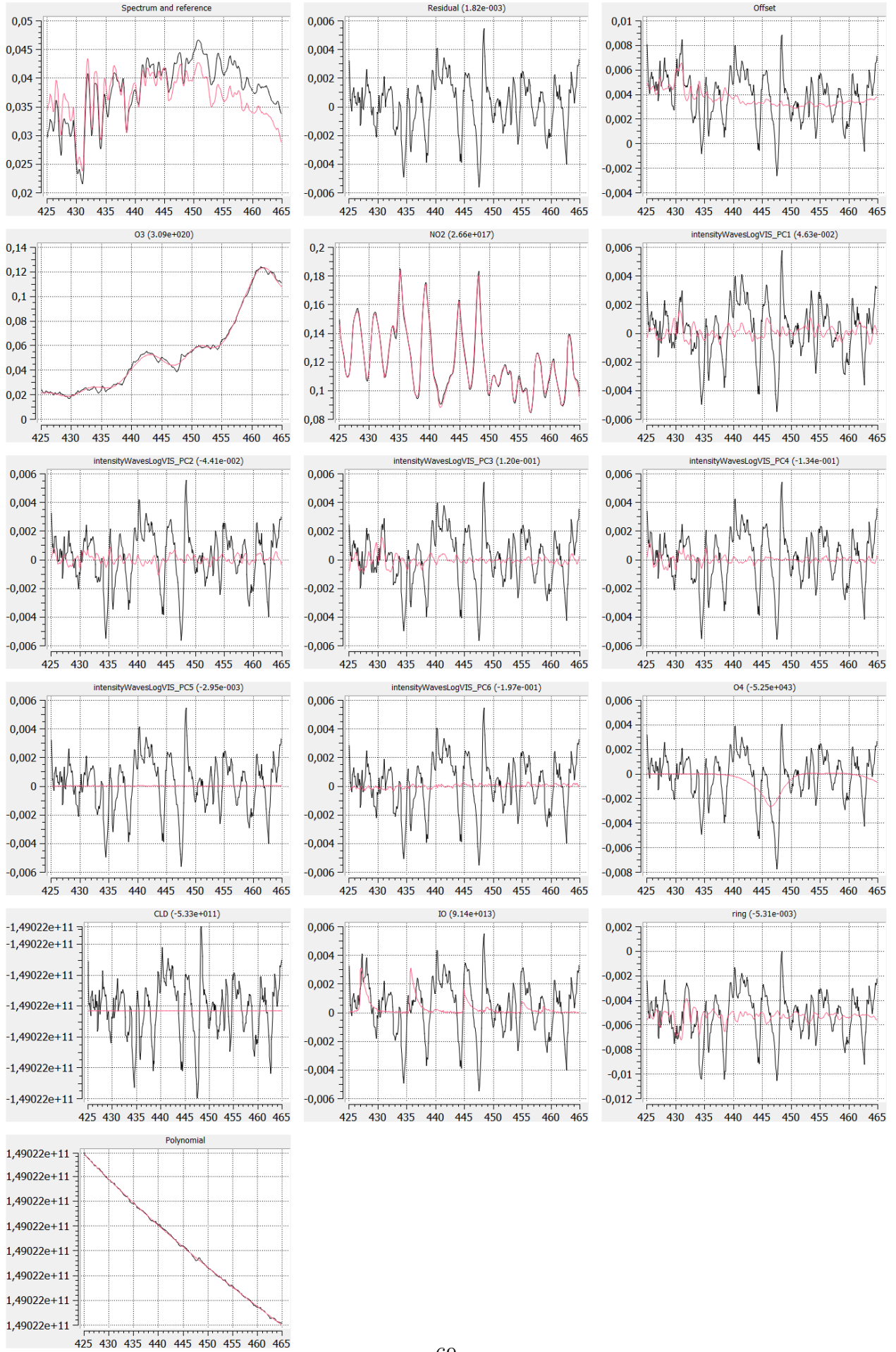


Figure B.1: The respective fit coefficient times the cross section (red) and red curve + residual (black) for all cross-sections included in the retrieval for SZA 93.46°

Appendix C

Zeroth Order Tikhonov Regularization Routine

```
m = len(y) # dim. measurements
n = len(K[0,:]) # dim. state vector

# Consider measurement uncertainties by merging them into K and y
Kw = np.zeros([m,n])
yw = np.zeros([m])
for i in range(m-1):
    Kw[i,:] = K[i,:]/yerr[i]
    yw[i] = y[i]/yerr[i]

# Singular value decomposition of forward model
U,Svec,VT = np.linalg.svd(Kw,full_matrices=False)
UT = U.T # U transpose
V = VT.T # V
F = np.array([s/(s**2+alpha**2) for s in Svec]) # Filter factors / s_i

# Moore Penrose pseudo-inverse with 0th order Tikhonov regularization
G = V.dot(np.diag(F).dot(UT)) # a.k.a. gain matrix
# Estimates
x = G.dot(yw) # state estimate
S = G.dot(G.T)# a posteriori error covariance
A = G.dot(Kw) # averaging kernel
```
